The Chemotherapeutic Potential of Bidentate Pyrrolide-Imine Gold(III) Chelates

Submitted in the fulfilment of the requirements for the degree of

Master of Science

By

Victoria A. Chiazzari

BSc(Honours)(University of KwaZulu-Natal)

November 2014

UNIVERSITY OF KWAZULU-NATAL

School of Chemistry and Physics

University of KwaZulu-Natal

Pietermaritzburg

College of Agriculture, Engineering and Science Declaration - Plagiarism

I, Victoria Chiazzari, declare that

1. The research reported in this thesis, except were otherwise indicated, is my original research.

2. This thesis has not been submitted for any degree or examination at any other university.

3. This thesis does not contain other persons' data, pictures, graphs or other information. unless specifically acknowledged as being sourced from other persons.

4. This thesis does not contain other persons' writing, unless specifically acknowledged as being sourced from other researchers. Where other written sources have been quoted, then:
    a. Their words have been re-written but the general information attributed to them has been referenced.
    b. Where their exact words have been used, their writing has been placed in italics and inside quotation marks, and referenced.

5. This thesis does not contain text, graphics or tables copied and pasted from the internet, unless specifically acknowledged, and the source being detailed in the thesis and in the Reference section.

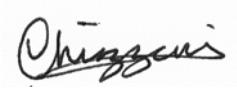

Signed..... Date: 30/10/2014

Victoria A. Chiazzari

I hereby certify that this is correct.

Signed..... Date: 30/10/2014

Dr. Matthew P. Akerman

(Supervisor)

Signed..... Date: 30/10/2014

Prof. Orde Q. Munro

(Co-Supervisor)

ACKNOWLEDGEMENTS

Firstly I would like to thank my supervisor Dr. Matthew Akerman for his dedication, detailed knowledge and advise with regard to my project. I am grateful for his constant encouragement and willingness to drive me to achieve higher standards and to overcome the obstacles faced in my project. The vast knowledge you have imparted will always be of value and I greatly appreciate your ambition and excitement towards furthering my project. To my co-supervisor Prof. Orde Munro your excitement and passion for inorganic chemistry is infectious and I appreciate your advice and guidance throughout my project.

I would also like to thank the South African National Research Foundation for the funding that has allowed me to pursue my dream of a MSc in inorganic chemistry.

To Mintek, I am grateful for their sponsorship and time to screen my gold(III) chelates against specific cancer cell lines.

Lastly I would like to thank my family for the support and belief that I can achieve anything I set my mind to. Your constant stability and words of encouragement will never be forgotten.

Publications

1. M.P. Akerman and V.A. Chiazzari, *J. Mol. Struct.* (2014), *1058*, 22-30.

Awards

1. The initial work in this thesis was presented at the South African Chemical Institute Postgraduate Colloquium (UKZN Westville, 2013). Second place was awarded for the presentation in the poster category.

List of Abbreviations

A2549	-	Non-small cell lung carcinoma
AM1	-	Austin Model 1
B3LYP	-	Becke Three Parameter Lee-Yang-Parr
Cisplatin	-	Diaminedichloroplatinum(II)
CSD	-	Cambridge Structural Database
DCM	-	Dichloromethane
DFT	-	Density Functional Theory
DMSO	-	Dimethyl Sulfoxide
DNA	-	Deoxyribonucleic Acid
DPPZ	-	Dipyrido[3,2-*a*:2',3'-*c*]phenazine
ECP	-	Effective Core Potentials
ES	-	Electro Spray
FTIR	-	Fourier Transform Infrared
GI_{50}	-	Growth Inhibition 50%
GIAO	-	Gauge-Including Atomic Orbital
HCl	-	Hydrochloric Acid
HOMO	-	Highest Occupied Molecular Orbital
HT-29	-	Human Colon Adenocarcinoma
IC_{50}	-	Half maximal inhibitory concentration
IR	-	Infrared
LANL2DZ	-	Los Alamos National Labs Double Zeta
LC_{50}	-	Lethal Concentration 50%
LMCT	-	Ligand-to-Metal Charge Transfer
LUMO	-	Lowest Unoccupied Molecular Orbital
MS	-	Mass Spectrometry
NBO	-	Natural Bond Orbital
NF-KB	-	Nuclear actor kappa-light-chain-enhancer of activated B cells
NMR	-	Nuclear Magnetic Resonance
RMSD	-	Root-Mean-Square Deviations
TK-10	-	Human renal adenocarcinoma
UV	-	Ultra violet
U251	-	Central nervous system

Abstract

Five (two novel) *bis*(pyrrolide-imine) Schiff base ligands were synthesized *via* a solid state method and characterised by ^{1}H and ^{13}C NMR, FTIR and UV/visible spectroscopy as well as high resolution mass spectrometry. The ligands comprised a pyrrole ring appended to various alkyl and aryl substituents via an imine bond. The structures of the ligands were varied through the nature of the appendages; complexes with propyl, phenyl, methylphenyl, ethylphenyl and methylnaphthyl appendages were synthesised. The coordination of the ligands to the gold(III) ion yielded five novel gold(III) chelates, synthesised through direct metallation of the free ligands using $[Bu_4N][AuCl_4]$. The solid-state structures were elucidated for four ligands using single crystal X-ray diffraction. All the free ligands exhibited complementary hydrogen-bonding between the pyrrole NH and imine nitrogen atom of an adjacent molecule leading to dimeric supramolecular structures. The gold(III) chelates were all fully characterised by the same spectroscopic techniques used for the ligands as well as X-ray crystallography. The gold(III) chelates all exhibited nominally square planar coordination geometry with two chloride ligands in a *cis*-configuration. The third and fourth coordination sites were occupied by the bidentate pyrrolide-imine ligands. The average $Au\text{-}N_{imine}$ bond length was 2.037(4) Å and $Au\text{-}N_{pyrrole}$ was 1.983(3) Å. The N1-Au-N2 bond angle was more acute than the ideal bond angle with an average angle of 82°. The solid-state structures showed Au···π and π···π interactions were common in all structures.

Density Functional Theory (DFT) simulations were performed on the gold(III) chelates and free ligands using the B3LYP/LanL2DZ and B3LYP/6-311G(d,p) level of theory for the gold(III) chelates and ligands, respectively. The simulations that were carried out include: NMR simulations, electronic transitions, geometry optimizations and vibrational frequency calculations. Overall, the simulations showed good accuracy with the basis set used for the free ligands producing more accurate results than that used for the gold(III) chelates. The DFT method was also used to further understand the supramolecular structures.

All five gold(III) chelates were screened against the following human cancer cell lines; A549, TK-10, U251 and HT29. The gold(III) chelates showed modest activity towards the four cancer cell lines with an average $-\log(IC_{50})$ value of 4.52. The chelate with a single methylene spacer between the imine bond and phenyl ring was the most cytotoxic across all cell lines.

List of Figures

List of Tables

List of Schemes

Contents

Chapter One: Introduction

1.1 Preface

Cancer is the second highest cause of death in developed countries,[1] with approximately 10 million people being diagnosed with cancer worldwide,[2] while 6.2 million will die from the disease annually.[3] It is a disease which can currently only be treated by the use of surgery, radiotherapy and drug therapy. Each of these procedures has their risks and side-effects. It has been documented that only half of the patients treated are cured while the other half may only experience prolonged survival. However, many do not benefit from any of the current treatments.[4] This is why there is an increased volume of drug research using metal complexes due to their stability and effectiveness in treating other conditions, such as rheumatoid arthritis.[5] By including a metal ion in the drug candidate it could potentially help overcome the problem of drug resistance as the metal ions are able to alter their modes of action. The use of gold started with the alchemists, but the first major use of gold in clinical medicine was started by Robert Koch[6] who discovered $Na[Au(CN)_2]$, could kill the bacteria responsible for tuberculosis.[4, 6-7] However, its use in the treatment of tuberculosis was limited due to its toxicity.

Gold(III) has been used in pharmaceutical compounds, but it is potentially unstable and is readily reduced to gold(I),[8-9] which can result in metal toxicity.[10] This will most likely cause kidney damage. The discovery that the gold(III) ion can be stabilised under physiological conditions by employing σ-donor ligands has allowed for its application in medicinal chemistry. Gold has shown characteristics of being a vital inhibitor of NF-kB (this is a transcription factor which produces tumour necrosis factor).[10] There has been recent interest in gold phosphine complexes, they have been shown to be suitable for biophysical and biomedical applications due to their anti-cancer activity and luminescent properties. The main challenges of drug discovery are finding a drug which is effective, but which does not harm the human body.[11]

There are many factors which come into play when developing a potential anti-cancer agent, such as the DNA binding mode and the effect it has on DNA and its replication. The topics that will be relevant to this research project are gold complexes, porphyrins and Schiff bases as well as platinum(II) complexes, which have a similar electronic structure to gold(III).

1.2 DNA Intercalators

1.2.1 DNA Binding Modes

The anticipated cellular target of the gold(III) chemotherapeutics synthesised in this work is DNA, thus a review of DNA binding modes has been included. There are three different modes of DNA binding, these are: 1) non-specific external association, 2) groove binding and 3) intercalation which occurs between DNA bases (Figure 1.2.1).[12-13,6] In this report only intercalation and cross-linking will be reviewed. DNA intercalators have defined characteristics which allow them to intercalate between DNA bases. They must be planar in shape and should contain three to four fused aromatic rings. The ligand must follow the insertion mechanism to become situated between two base pairs of DNA. In order for insertion to be successful the aromatic rings must be perpendicular to the axis of the helix.

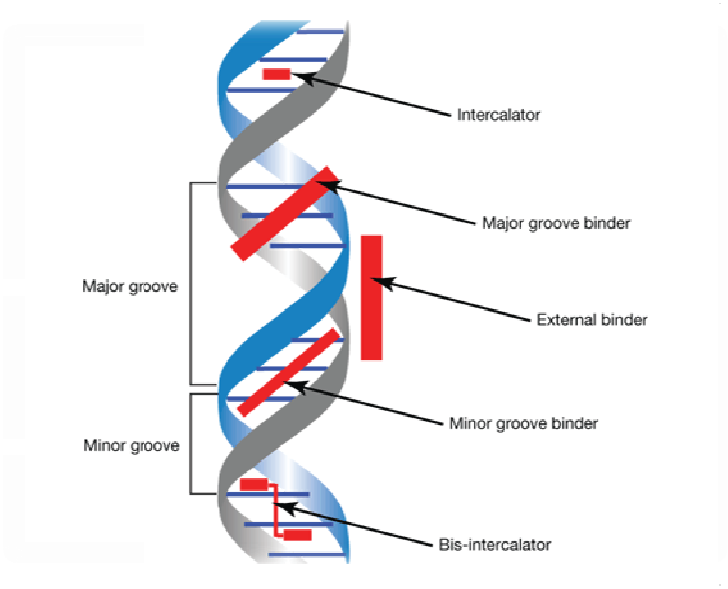

Figure 1.2.1: Different modes of DNA binding.[13]

The intercalated ligands are held in place by hydrogen bonding and van der Waals forces.[12] The inserted ligands should have an extended electron, rich, planar aromatic ring system. The function of the extended planar aromatic system is to allow for π-π interactions which stabilise the unwinding and extension of the deoxyribose-phosphate backbone in DNA. This unwinding and extension of the DNA is the result of the insertion of the compound.[14]

1.2.2 Organic DNA Intercalators

Some naturally occurring chemotherapeutics which exert their cytotoxicity via DNA intercalation are doxorubicin and daunarubicin (Figure 1.2.2).

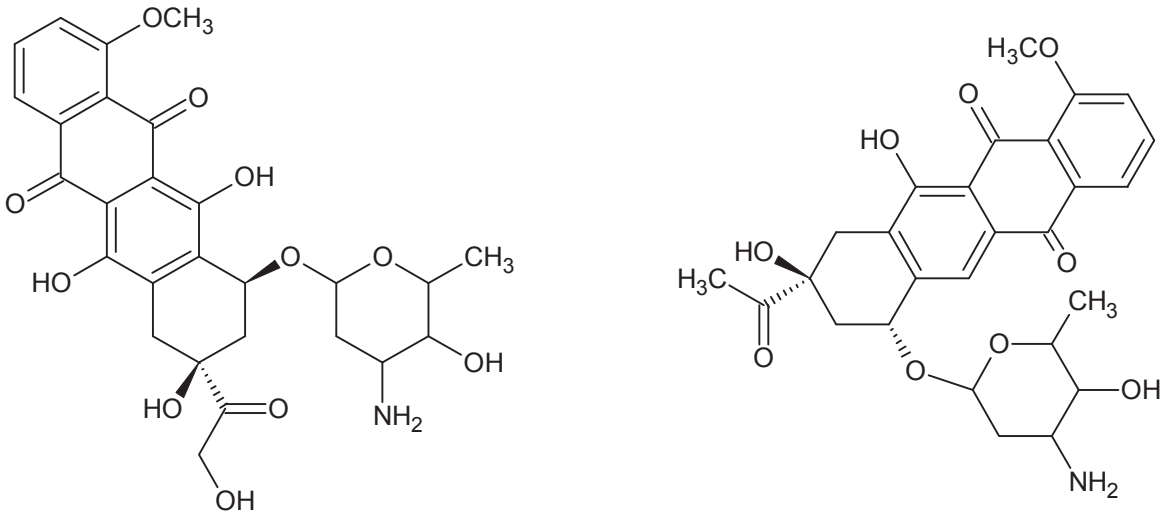

(a) (b)

Figure 1.2.2: (a) Doxorubin and (b) Daunarubicin both show extended aromaticity and multiple hydrogen bonding sites.

Doxorubin is an organic intercalator extracted from *streptomyces peucetius,*[2] experimentation has shown that it has a wide spectrum of activity. Daunorubicin came from the fermentation broth of *streptomyces peucetius.*[12] Epirubicin (Figure 1.2.3) is a synthetic analogue of doxorubicin, differing only in its stereochemistry.[12] Another known organic intercalator is dipyrido[3,2-*a*:2',3'-*c*]phenazine (dicatatonic dppz) this derivative of dppz is shown below in Figure 1.2.3. Dppz has been found to be almost completely insoluble in water, but is an efficient DNA intercalator as it is a planar molecule.[15] It is also very stable at a neutral pH.[15] To overcome the issue of insolubility in water, it has been converted to the dication. The dicationic form is shown in Figure 1.2.3.

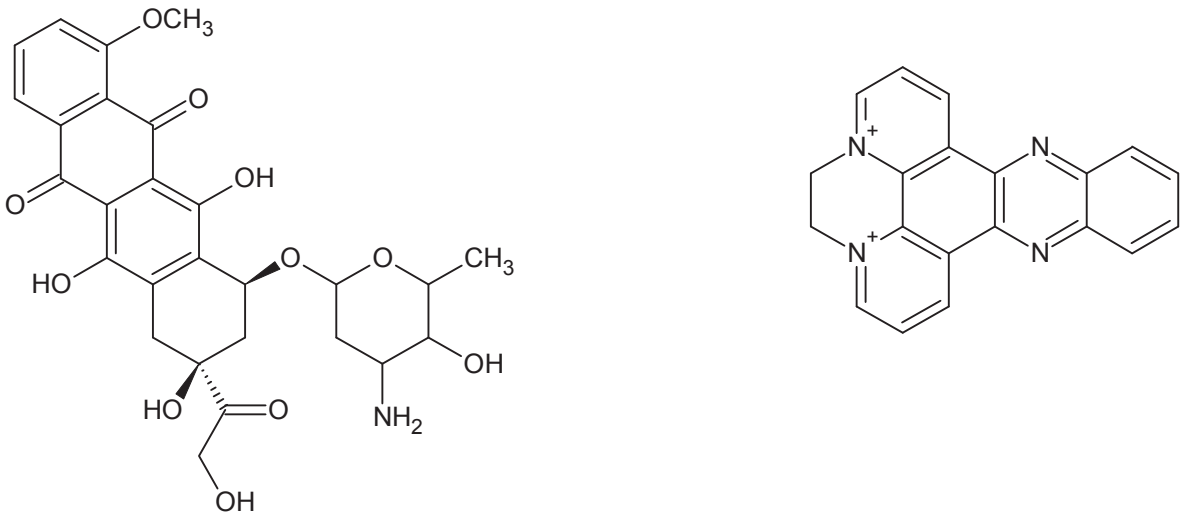

(a) (b)

Figure 1.2.3: 2D representation of (a) Epirubicin and (b) DPPZ: two examples of organic DNA intercalators.

1.2.3 Metal-Based DNA Intercalators

An example of a metal-based DNA intercalator is a gold(III) (meso-tetraaryl)porphyrin (Figure 1.2.4) and *cis*-dichloro[(isoquinolin-3-ylcarbonyl)[2-[(isoquinolin-3-ylcarbonyl) amino]phenyl] azanido]gold-(III), Figure 1.2.5.

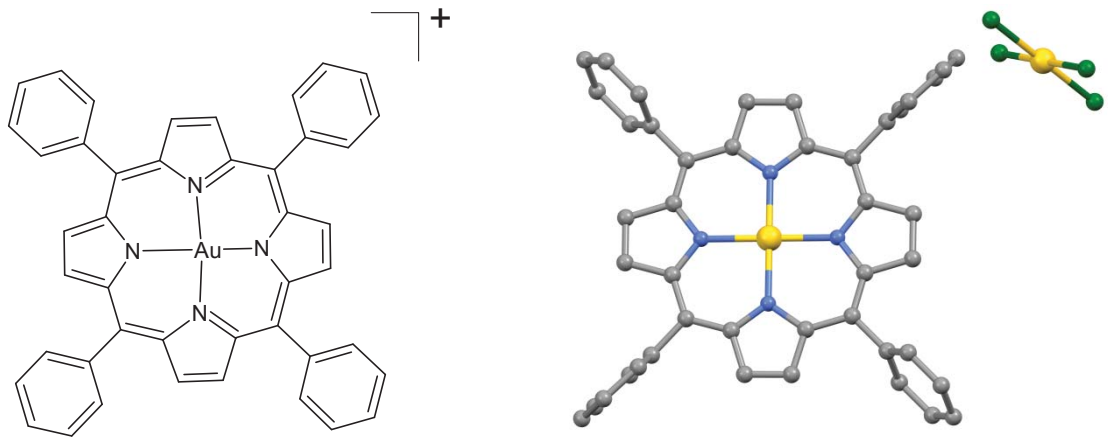

Figure 1.2.4: Gold(III) meso-tetraryl porphyrin: a known DNA intercalator.[16]

The above figure shows the structure of a gold(III) meso-tetraryl porphyrin, it was experimentally found to be stable against demetallation and was shown to have a higher

cytotoxicity against many human cancer cell lines than cisplatin.[16-17] This proved that gold(III) porphyrins are a potential anti-cancer drug; *in vitro* results showed that the cellular target of gold(III) porphyrins is DNA. The porphyrin is a tetradentate dianionic ligand, ligands of this structure are required to stabilise the gold(III) ion in its high oxidation state, particularly under physiological conditions.[7] It was determined that the robust square-planar geometry of the gold(III) complex reduces binding events and reductive demetallation when it comes into contact with serum proteins.[17] This is a major advantage over cisplatin which is known to bind serum proteins, reducing its effective concentration in blood.[17]

It has been shown that the porphyrin causes DNA fragmentation (*in vivo*), this is possibly due to the linkage between the porphyrin and DNA.[10] The porphyrin ligand will also carry the metal to the cellular target (in this case DNA).[10] It was found that gold(III) porphyrins cause apoptosis (as opposed to necrosis) of cancer cells, this was determined using confocal microscopy.[10]

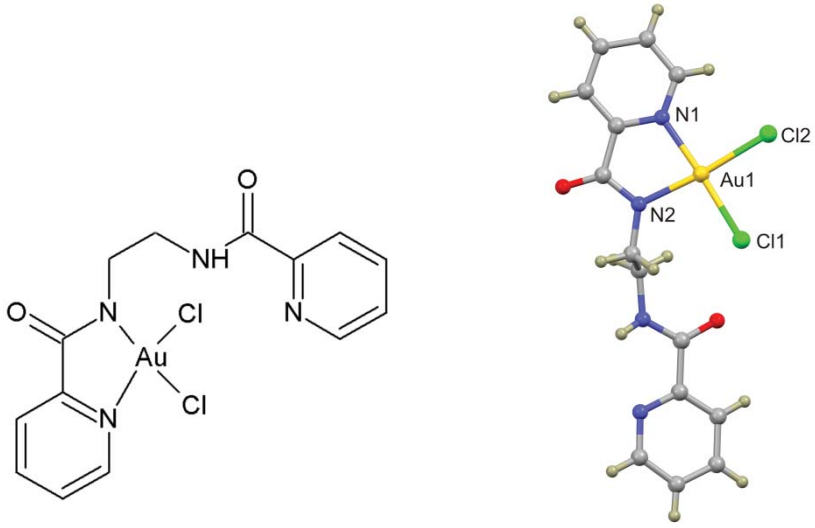

Figure 1.2.5: *Cis*-dichloro{(pyridin-2-ylcarbonyl)[2-[(pyridin-2ylcarbonyl)amino]ethyl] azanido}gold(III).

Figure 1.2.5 shows a gold(III) chelate which was synthesised as a potential chemotherapeutic, findings showed that the half-chelated amide complex acted as a topoisomerase II poison and underwent the same mechanical binding as topotecan, which is a topoisomerase I poison.[18] The compound was shown to be a weak DNA intercalator using a DNA winding assay. The chelate showed good cytotoxicity in a five dose NCI-60 screen. The mean IC_{50} value was 38 μM and it was more active against certain tumour cell lines than cisplatin.[18] The structure of the above gold(III) chelate is similar to that of cisplatin in that it has two chloride ligands chelated to the metal centre in a *cis* configuration. The amide ligand in conjunction with the chloride ligands stabilises the gold(III) cation sufficiently to eliminate the risk of reduction of gold(III) to gold(I).[18] The chelates proposed in this work are closely related to these compounds and may too act as topoisomerase II poisons.

1.2.4 Cross-Linking Agents

DNA cross-linking agents were first discovered during World War II when mustard gas was in use, this lead to intensive research into aliphatic nitrogen mustards as potential anti-cancer agents. There are two types of cross-linking methods one is intrastrand and the other is interstrand. Intrastrand is where the drug links to one DNA strand, while interstrand is the opposite in that the drugs bind to both DNA strands of the double helix.[12] Both types of binding inhibit DNA replication and transcription, this results in programmed cell death: apoptosis. It has been shown that cross-linking agents cause distortion of the DNA helix.[12] This distortion in the three-dimensional structure results in the activation of DNA repair enzymes, which recognise this distortion. This leads to resistance to these types of drugs as the enzyme is able to repair the distorted DNA.[19] An example of a cross-linking drug is cisplatin (Figure 1.2.6). These cross linking drugs attach to the DNA strand by undergoing elimination of the chloride ligands and subsequently binding to the guanine DNA bases.

1.2.5 Platinum Metallodrugs

Due to gold(III) being isoelectronic with platinum(II) and it having the same square planar geometry as *cis*-diammminedichloroplatinum (cisplatin) there is sudden interest in gold(III) chemotherapeutic agents.[20] Since gold(III) has the same geometry as cisplatin (Figure 1.2.6) it is expected that gold(III) will target DNA, as cisplatin does.[2]

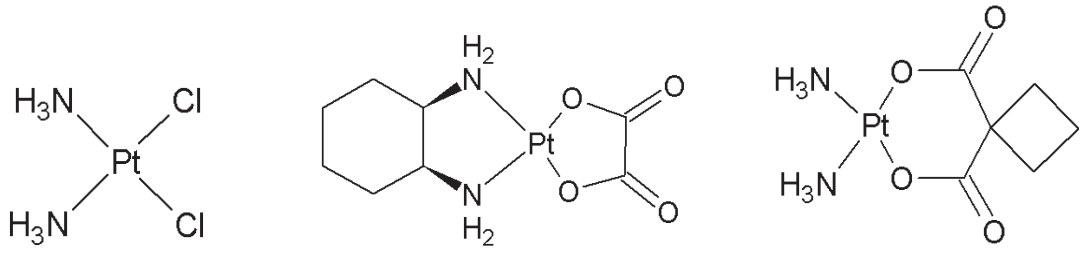

(a) (b) (c)

Figure 1.2.6: (a) Cisplatin (*cis*-diamminedichloroplatinum) and two of its derivatives: (b) oxaliplatin and (c) carboplatin.

Cisplatin was developed in the 19th century. It has been very effective, but has particular limitations which are: the resistance of particular tumours to the drug and its side-effects (neurotoxicity and nephrotoxcity).[2] Another limitation is that secondary tumours are often resistant to cisplatin after the primary treatment.[17]

It is thought that due to its high rate of irregular binding to extracellular and intracellular proteins that cisplatin would have an impaired cytotoxicity. This binding causes a negative effect on the efficiency of the drug as the binding decreases the effective concentration of the drug which reaches the tumour cells.[17]

Cisplatin binds to DNA in a cross-linked form,[21] this causes the DNA helical structure to distort, which in turn inhibits DNA replication and transcription.[17] This distortion occurs as cisplatin does not interact with the sugar phospohate backbone of DNA, but rather with the base pairs.[22] It favours bonding to guanine and cytosine rich regions of DNA. Cisplatin has two kinetically labile chloride ligands which can either react with a single site of two different bases or two different sites of one base.[22] Cisplatin's structure is directly related to the proposed gold(III) chelates in this work, it is relevant in that cisplatin was the breakthrough into metal-based anti-cancer drugs, which led to increased research into the topic.[17]

It is the *cis* geometry of cisplatin which leads to it's *in vivo* activity. The *trans* analogue is inactive *in vivo*.[17] This is because *trans* isomers of platinum(II) complexes are more reactive and unwanted side reactions occur, reducing the pharmacological activity. It has been assumed that gold(III) complexes are very similar to cisplatin this means that they may have a similar DNA targeting ability.[2] This has been proven with the gold(III) chelates targeting the mitochondria at a sub-cellular level.[2] It has been observed that platinum(II) complexes have an enhanced DNA binding affinity when compared to gold(III) complexes. This implies that these two classes of metal complexes will have different biological mechanisms and effects.[8, 17]

1.3 Topoisomerase Inhibitors

Cleavage, annealing and supercoiling of DNA is controlled by a group of enzymes called topoisomerases.[12] This is an important function as without it DNA could not unwind and transcription could not occur, thus cell death would be initiated due to the desired proteins not being synthesised.[12]

There are two types of topoisomerase they are I and II, each one carries out a different function. Topoisomerase I causes a single strand break in the DNA helix. The break allows the strand to spin, releasing the torque caused by the winding and unwinding during replication, this are shown in Figure 1.3.1. When the strand is relaxed the enzyme reforms the phosphodiester linkage.[12] It is thought that topoisomerase I inhibitors will be more effective on cancer cells as they grow and reproduce at an increased rate compared to normal cells. Topoisomerase II enzymes cleave both DNA strands and pass a new duplex strand through the cut simultaneously, then reseals the strands.[12, 23] It has been noted that topoisomerase II inhibitors have a higher activity towards testicular cancer, leukemia and lymphomas.[12]

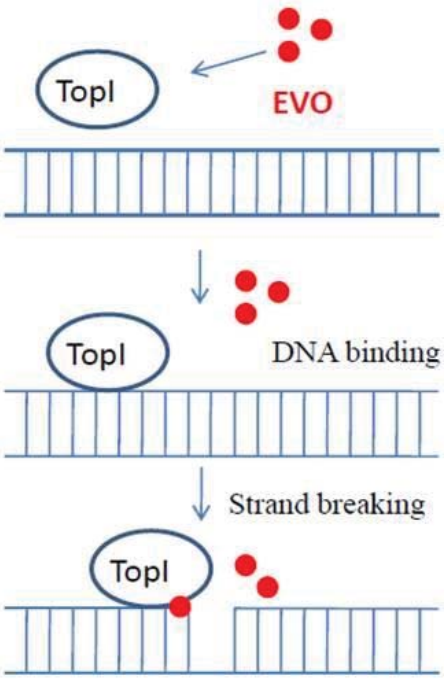

Figure 1.3.1: Illustration of topoisomerase I mediated DNA relaxation.[24]

Topotecan and podophyllotoxin are examples of topoisomerase I and II inhibitors, respectively. The structures of these commercially available drugs are shown in Figure 1.3.2 below.[12]

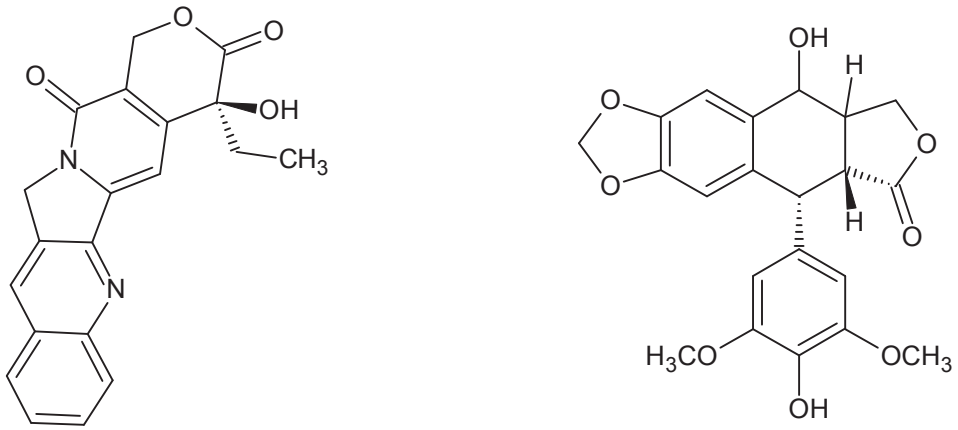

(a) (b)

Figure 1.3.2: Two-dimensional image of (a) topotecan and (b) podophyllotoxin. Topoisomerase I and II inhibitors, respectively.

Gold(III) complexes similar in structure to those proposed in this work have been shown to exert their cytotoxicity through topoisomerase inhibition/poisoning.

1.4 Schiff Base Ligands

Schiff bases are amongst the most studied compounds in recent years in areas such as biochemical, analytical and antimicrobial research.[25] Many Schiff bases have shown profound potential as anti-cancer drugs, but can be highly sensitive to the molecular environment.[25] There are numerous examples of Schiff base ligands including bidentate, tetradentate, *N*-donor and mixed *N*, *O* donor ligands. Shown below in Figure 1.4.1 is a variety of Schiff base ligands, many of which have been chelated to gold(III) in the search for new chemotherapeutic agents. These ligands inclue: *N,N′*-ethylenebis(salicylimine)(salen)[25-26] and fur-o-phdn,[27] The gold(III) salen chelate has a lower cytotoxicity towards most tumour cells compared to gold(III) porphyrins because of its reduced stability in aqueous media.[25] There are a few main reasons why Schiff bases have been a focus of research.[28] Firstly, they can be structured to favour either intercalation or external association with DNA.[29] Additionally, their cytotoxicity has also been shown to increase upon chelation to metal ions, making them ideal for inorganic drug candidates.[29]

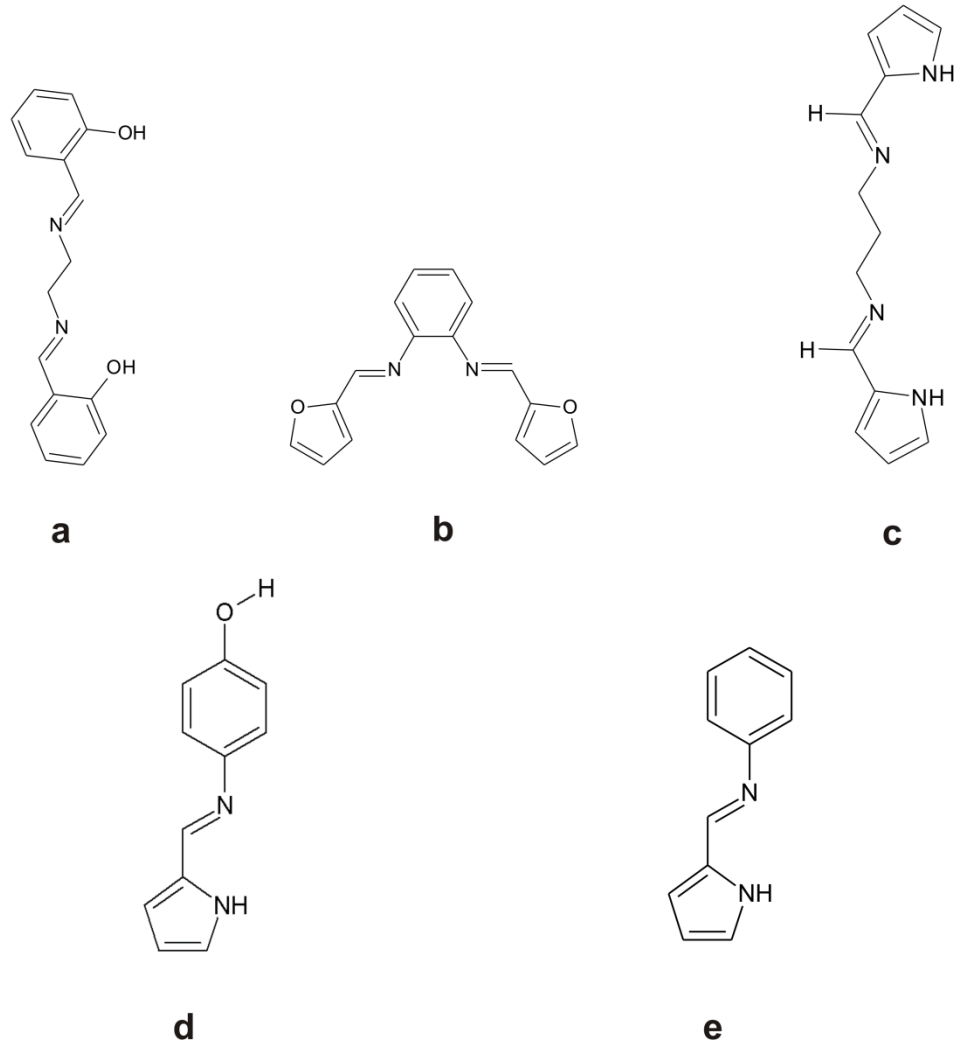

Figure 1.4.1: (a) *N*,*N*'-ethylenebis(salicylimine) (Salen),[25] (b) fur-o-phdn,[27] (c) *N*,*N*'- bis (pyrrol-2-ylmethylene)propane-1,2-diamine,[4] (d) 4-((1*H*-pyrrol-2-ylmethyl -ene)amino)phenol[30] and (e) (*E*) - *N* - phenyl -1- (1*H*- pyrrol - 2yl) methanim -ine[31] are examples of Schiff base ligands.

The Schiff base (*N*,*N*'-*bis*(pyrrol-2-ylmethylene)propane-1,2-diamine)[4] is a tetradenate Schiff base ligand and consists of two bridged pyrrole groups.[4] It was determined using X-ray crystallography that only the *E* isomer is favoured as the Z isomer would result in steric strain between the pyrrole and methylene groups.[4] Pyrrolide-imine Schiff bases are attractive ligands for coordination to various metal ions. Metal ion complexation with concomitant deprotonation of the pyrrole NH affords an *N*,*N*'-donor, bidentate monoanionic, ligand which can be used to stabilise metal ions in high oxidation states. This class of ligands has been coordinated to various metals including: Co, Cu, Ir, Mg, Mo, Ni, Pd, Pt, Ti and V. Upon coordination to various metal ions these compounds have been used as catalysts in polymerization reactions, luminescent materials, oxygen atom transfer (OAT) reagents and in the synthesis of coordination polymers.[32]

1.5 Medicinal Applications of Gold

The use of gold has been traced back as far as 3500 BC,[5] and has been found to have many medicinal applications. Although it has been broadly used, there is generally a lack of understanding of their mode of action as most of the drugs have not been designed for their specific application. The majority of gold drugs use gold(I) which has been used in the treatment of rheumatoid arthritis,[5, 33-34] it is a soft d^{10} metal ion which generally forms a linear coordination geometry. A well known gold(I) drug is Auranofin (Figure 1.5.1) which has been widely used for the treatment of rheumatoid arthritis.[2, 6, 33, 35] Many gold(I) drugs have been synthesised, but have not reached clinical trials due to their instability which leads to the formation of gold colloids *in vivo* which cause cardio toxicity. This is the reason for focusing on gold(III) as a potential scaffold around which anti-cancer agents can be constructed.

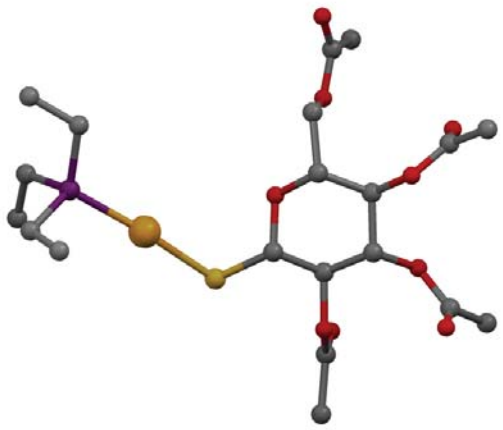

Figure 1.5.1: X-ray structure of Auranofin.

Gold(III) has been a recent area of interest for anti-cancer drugs due to its square planar geometry and d^8 electron structure,[36] features it shares with platinum(II).[17, 37-38] Gold(I) is generally not used in anti-cancer drugs as it is relatively unstable,[39] linear and only has two coordination sites.[4, 6] Even though gold(III) is preferred, there are difficulties in its biological application; such as gold(III) readily reduces to gold(I) or gold(0) in biological media.[17] Its instability in biological media can cause metal cytotoxicity and other application problems. In order to increase the stability of the gold(III) ion it needs to be co-ordinated to multidentate, σ-donor ligands as this stabilises the metal ion in its high oxidation state. Ligands such as cyclams, terpyridenes and phenanthrolines all have this stabilising effect on gold(III).[17, 20, 40]

Gold(III) complexes have become an exciting area of research due to their immunomodulatory effects and cytotoxicity towards tumour cells. It has been shown that gold(III) compounds do not bind to nucleic acids as strongly as platinum(II) drugs; this means that there is likely a different mechanism for the observed biological effects. Gold(III) complexes do not only target DNA, but rather have shown potential in inhibiting mitochondrial thioredoxin reductase.[2, 5, 16-17, 35, 41-42]

The following gold(III) compounds have been shown to induce apoptosis to a greater extent than cisplatin, while only changing the cell cycle slightly. The [Au(bipydmb-H)(OH)]PF_6 complex has an average IC_{50} value of 1.42 μM while [Au(bipydmb-H)(2,6-xylidine-H)]PF_6 (Figure 1.5.2) has an average IC_{50} value of 0.21 μM.[42] In comparison, cisplatin has a mean IC_{50} value of 27 μM.

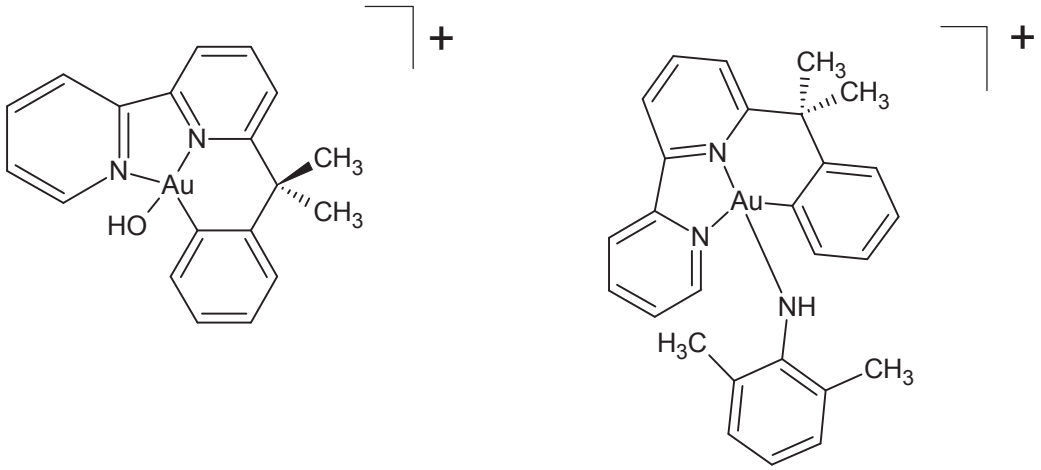

(a) (b)

Figure 1.5.2: (a) [Au(bipydmb-H)(OH)]PF_6 and (b) [Au(bipydmb-H)(2,6-xylidine-H)]PF_6: potential anti-cancer gold(III) complexes.[42]

The nature of the auxiliary ligands alters the DNA-binding affinity and influences the drug's mechanism of action. Overall, mitochondria are seemingly the primary target for most gold(III) compounds.[42]

1.6 Proposed Research

The goal of this research is to synthesise a range of bidentate pyrrolide-imine gold(III) chelates. These compounds are novel, but have similarities to previously reported structures.[18, 43] The ligands consist of a pyrrole ring appended to an aromatic moiety via an imine bond. The structure of each ligand will differ by the structure of the aromatic appendage. The structures of the ligands that will be chelated to the gold(III) cation are shown in Figure 1.6.1.

The coordination of this range of ligands to gold(III) occurs with deprotonation of the pyrrole NH. The ligand HL2 has been previously reported coordinated to Hf(II), Zr(II) and Mg(II).[44-45] When the pyrrolide-imine ligands are coordinated to the gold(III) cation, they will occupy two of the coordination sites, the two remaining sites will be occupied by chloride ligands. Thus the chelate will have an overall neutral charge.

The metal ion is expected to show a nominally square planar coordination geometry. This is attributed to the d^8 electronic configuration and the associated vacant $d(x^2\text{-}y^2)$ orbitals.

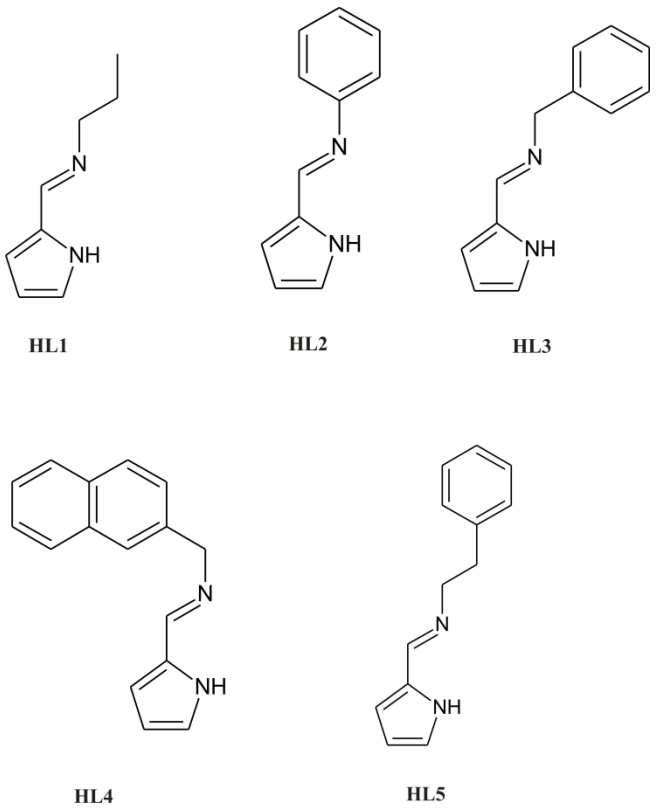

Figure 1.6.1: Structures and naming scheme of the pyrrolide-imine ligands that will be chelated to gold(III) in this work.

The bidentate pyrrolide-imine gold(III) chelates have been designed to be DNA intercalators or cross-linking agents and topoisomerase poisons/inhibitors. The design of these complexes is based on the structural features of cisplatin and previously reported gold(III) chelates (Figure 1.6.2).

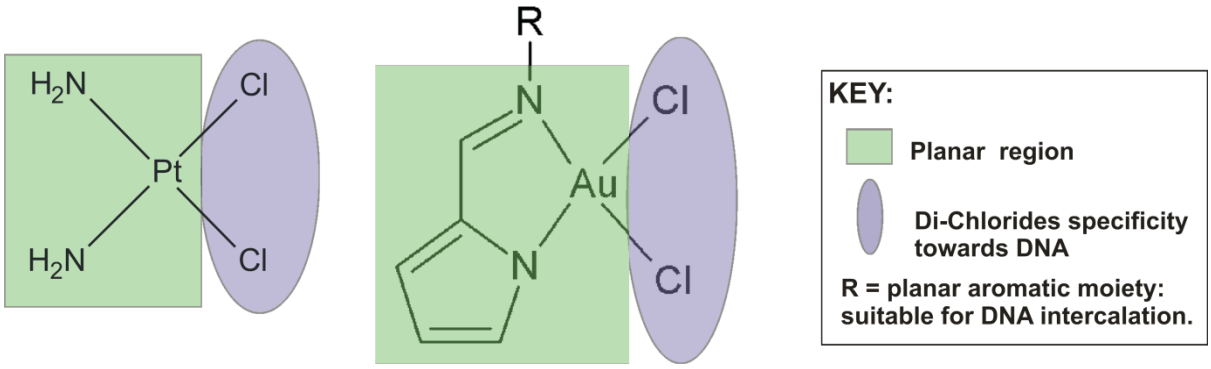

Figure 1.6.2: A comparison of key structural motifs of cisplatin and the bidentate pyrrolide - imine gold(III) chelates studied in this work.

The proposed gold(III) chelates have a planar aromatic region, this will allow for effective DNA intercalation. The extended aromatic nature of the planar region will increase the binding affinity, due to the positive π-π interactions which are likely to occur between the aromatic base pairs and the metal chelate.[6] The dichloride ions allow for increased specificity towards DNA due to base pairs favouring chlorinated species, they also allow for potential cross-linking with DNA base pairs.[42] An additional feature compared to cisplatin is the aromatic appendage, this will potentially allow for additional interactions with the DNA helix. The structure of the appendage will be varied to determine the influence that it has on the cytotoxicity.

1.7 Objectives

The following objectives for the project have been identified:

1. To synthesise and characterise the pyrrolide-imine ligands by ^{1}H, ^{13}C, cosy, DEPT, HMBC and HSQC NMR spectroscopy as well as UV/visible and FT-IR spectroscopy.
2. Study the free ligands by single crystal X-ray crystallography.
3. Characterise each novel gold(III) chelate by NMR, UV/visible and FT-IR spectroscopy. These characterisation data will be compared to that of the free ligands to confirm chelation to the gold(III) cation.
4. Study the gold(III) chelates by single crystal X-ray crystallography and determine accurate geometric information about each of their structures.
5. Computational studies will be performed using density functional theory (DFT). These computational studies will be used to expand the understanding of the experimental properties of the free ligands and metal chelates.
6. The gold(III) chelates will be screened against four human cancer cell lines to determine their cytotoxicity.

Chapter Two: Experimental

2.1 General Methods

For all reactions, solvents were dried and distilled before use. Analytical grade solvents were used in the purification processes. All reagents were purchased from Aldrich, Merck or Fluka and were used as received. Metallic gold (99.999%) was received from Harmony Gold in pellet form and used as received.

2.2 Instrumentation

NMR spectra were recorded with a Bruker Avance III 400 spectrometer equipped with a Bruker magnet (9.395 T) using a 5 mm TBIZ probe at the following frequencies: ^{1}H = 400 MHz and ^{13}C = 100 MHz. The spectra were recorded at 30 °C. All NMR experiments were conducted using Bruker Topspin 2.1, patch level 6.[46] All proton and carbon chemical shifts are referenced to TMS using DMSO-d_6 as the identifying signal: ^{1}H, 2.50 ppm and ^{13}C, 39.5 ppm. FTIR spectra were recorded using a Bruker Alpha FTIR spectrometer equipped with an ATR platinum Diamond 1 reflectance accessory. The machine acquired the information in 32 scans with a spectral resolution of 1.0 cm^{-1}. Electronic spectra were recorded using a Shimadzu UVPC-1800 double beam UV-visible scanning spectrometer (1.0 cm path length cuvette). Spectra were recorded from 800 to 200 nm. High resolution masses were determined with a Waters Acquity-LCT Premier coupled high performance liquid chromatography mass spectrometer (time-of-flight) using electrospray ionisation in positive mode. Fully assigned NMR, UV-visible, IR and mass spectra are available in **Appendix A**.

2.3 Ligand Synthesis

2.3.1 Synthesis of *N*-(1*H*-pyrrol-2-ylmethyl)propan-1-amine

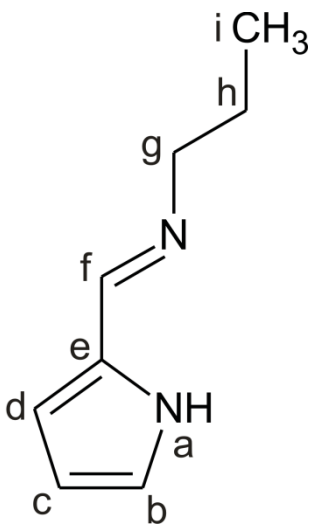

Figure 2.3.2: Structure and atom numbering scheme of *N*-(1*H*-pyrrol-2-ylmethyl)propan-1-amine (HL1).

Pyrrole-2-carboxaldehyde (1.000 g, 10.52 mmol) and propyl amine (0.719 g, 52.58 mmol) were ground together in a warm (85 °C) pestle and mortar until the propyl amine had reacted, approximately 10 minutes. The crude HL1 was dissolved in DCM (20 mL) and dried using anhydrous magnesium sulphate. The solution of HL1 was filtered and left to evaporate at atmospheric pressure. The resulting oil was dissolved in DCM and titurated with hexane. This yielded a yellow oil (1.109 g, 77.4% yield). UV/vis (acetonitrile) [λ_{max}, nm; ε, mol^{-1} dm^3 cm^{-1}]: 277; 2.144×10^4. *Anal*. Calc. for ES^+: 136.19 m/z. *Exp*. ES^+: 137.10 m/z ($M + H^+$). ^1H NMR (400 MHz, DMSO-*d6*, 298 K) [δ, ppm]: 0.88 (t, 3H, i), 1.62 (m, 2H, h), 3.44 (m, 2H, g), 6.09 (m, 1H, c), 6.44 (m, 1H, d), 6.85 (s, 1H, b), 8.04 (s, 1H, f), 11.34 (s, 1H, a). ^{13}C NMR (100 MHz, DMSO-*d6*, 298 K) [δ, ppm]: 12.20 (i), 24.2 (h), 62.67 (g), 109.24 (c), 113.59 (d), 122.30 (b), 130.53 (e), 151.99 (f). IR (cm^{-1}): 739.60 (s, pyrrole C-H bend), 1423.30 (s, C=C), 1581.70 (s, C=N), 2844.80 (w, imine C-H), 3163.4 (w, pyrrole N-H).

2.3.2 Synthesis of (*E*)-*N*-phenyl-1-(1*H*-pyrrol-2-yl)methanimine

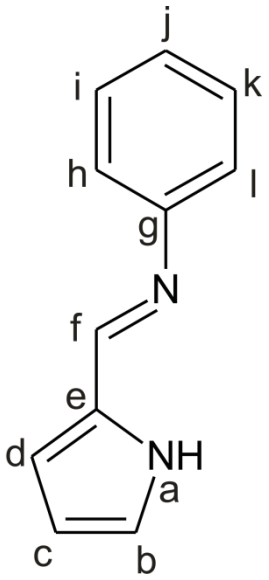

Figure 2.3.2: Structure and atom numbering scheme of (*E*)-*N*-phenyl-1-(1*H*-pyrrol-2-yl) methanimine (HL2).

Pyrrole-2-carboxaldehyde (1.000 g, 10.52 mmol) and aniline (4.897 g, 52.58 mmol) were dissolved in ethanol (10 mL). The solution was refluxed for 3 hours, during this time the solution changed from colourless to pale yellow. The ethanolic solution was dried using anhydrous magnesium sulphate and filtered by gravity filtration. Slow evaporation of the ethanolic solution yielded HL2 as a white crystalline solid (0.837 g, 46.8% yield). UV/vis (acetonitrile) [λ_{max}, nm; ε, mol^{-1} dm^3 cm^{-1}]: 322, 2.11 × 10^4 *Anal*. Calc. for ES^+: 170/08 m/z. *Exp*. ES^+: 171.09 m/z ($M + H^+$). ^1H NMR (400 MHz, DMSO-*d6*, 298 K) [δ, ppm]: 6.20 (m, 1H, c), 6.71 (m, 1H, d), 7.02 (s, 1H, b), 7.18 (m, 3H, h, j, l), 7.39 (m, 2H, i, k), 8.28 (s, 1H, f), 11.73 (s, 1H, a). NMR (100 MHz, DMSO-*d6*, 298 K) [δ, ppm]: 116.35 (c), 120.69 (d, h), 123.77 (b), 124.85 (l), 129.13 (I, k, j), 130.48 (e), 150.51 (f), 152.15 (g). IR (cm^{-1}):
739.89 (s, pyrrole C-H bend), 1416.17 (s, C=C), 1617.19 (s, C=N), 2842.25 (w, imine C-H), 3213.20 (w, pyrrole N-H).

2.3.3 Synthesis of (*E*)-*N*-benzyl-1-(1*H*-pyrrol-2-yl)methanimine

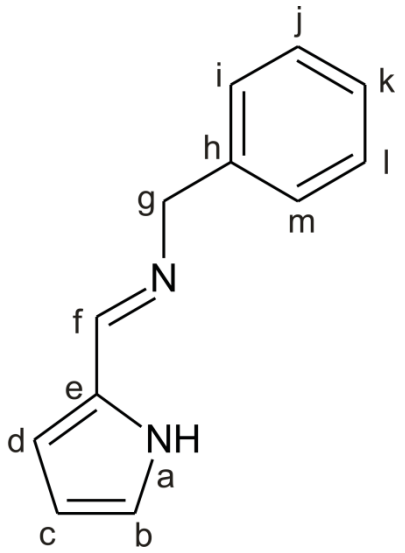

Figure 2.3.3: Structure and atom numbering scheme of (*E*)-*N*-benzyl-1-(1*H*-pyrrol-2-yl) methanimine (HL3).

Pyrrole-2-carboxaldehyde (1.000 g, 10.52 mmol) and benzyl amine (0.563 g, 52.58 mmol) were ground together in a warm (85 °C) pestle and mortar until the benzyl amine had fully reacted, approximately 10 minutes. The crude HL3 was dissolved in DCM (20 mL) and dried using anhydrous magnesium sulphate. The solution was filtered and allowed to evaporate. This resulted in a colourless crystalline solid (1.340 g, 69.2% yield). UV/vis (acetonitrile) [λ_{max}, nm; ε, mol^{-1} dm^3 cm^{-1}]: 281; 1.53 × 10^4. *Anal*. Calc. for ES^+: 184.10 m/z. *Exp*. ES^+: 185.11 m/z ($M + H^+$). ^1H NMR (400 MHz, DMSO-*d6*, 298 K) [δ, ppm]: 4.67 (s, 2H, g), 6.12 (m, 1H, c), 6.49 (m, 1H, d), 6.89 (s, 1H, b), 7.19 - 7.35 (m, 5H, i, j, k, l, m), 8.20 (s, 1H, f), 11.43 (s, 1H, a). ^{13}C NMR (100 MHz, DMSO-*d6*, 298 K) [δ, ppm]: 64.41 (g), 109.38 (c), 114.24(d), 122.64 (b), 127.64 (m), 127.47 (k), 128.51 (i), 128.71 (j, l), 130.48 (e), 140.59 (h), 153.05 (f). IR (cm^{-1}): 738.33 (s, pyrrole C-H bend), 1423.37 (s, C=C), 1632.18 (s, C=N), 2828.94 (w, imine C-H), 3142.25 (w, pyrrole N-H).

2.3.4 Synthesis of (*E*)-*N*-(naphthalen-2-ylmethyl)-1-(1*H*-pyrrol-2-yl) methanimine

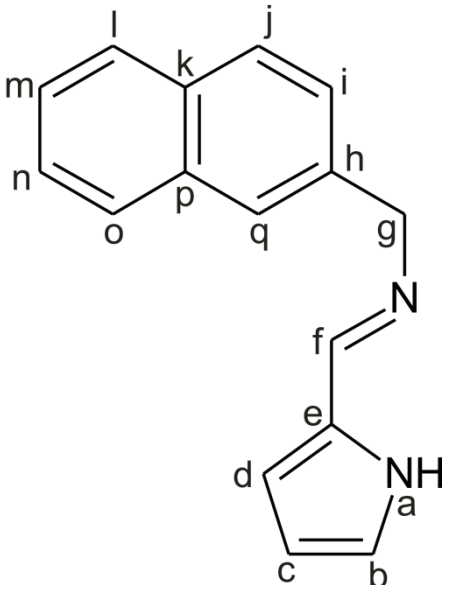

Figure 2.3.4: Structure and atom numbering scheme of (*E*)-*N*-(naphthalen-2-ylmethyl)-1-(1*H*-pyrrol-2-yl)methanimine (HL4).

Pyrrole-2-carboxaldehyde (0.500 g, 5.258 mmol) and 1-naphthylmethylamine (0.827 g, 5.28 mmol) were ground together in a warm (85 °C) pestle and mortar. This yielded HL4 as a white powder (1.134 g, 92.0% yield). UV/vis (acetonitrile) [λ_{max}, nm; ε, mol^{-1} dm^3 cm^{-1}]: 223; 5.36 × 10^4, 283; 2.03 × 10^4. *Anal*. Calc. for ES^+: 234.12 m/z. *Exp*. ES^+: 235.1237 m/*z* ($M + H^+$). ^{1}H NMR (400 MHz, DMSO-*d6*, 298 K) [δ, ppm]: 5.12 (s, 2H, g), 6.11 (t, 1H, c), 6.48 (m, 1H, d), 6.87 (s, 1H, b), 7.44 - 7.60 (m, 4H, i, j, n, o), 7.84 (d, 1H, k), 7.93 (m, 1H, m), 8.13 (d, 1H, p), 8.29 (s, 1H, f), 11.4052 (s, 1H, a). ^{13}C NMR (100 MHz, DMSO-*d6*, 298 K) [δ, ppm]: 61.33 (g), 109.40 (c), 114.23 (d), 122.71 (b), 124.41 (i, p), 126.03-126.50 (n, o, j), 127.78 (k), 128.90 (m), 130.49 (q), 131.67 (e), 133.78 (l), 136.61 (h), 153.30 (f). IR (cm^{-1}): 729.34 (s, pyrrole C-H bend), 1421.58 (s, C=C), 1643.69 (s, C=N), 2853.13 (w, imine C-H), 3170.73 (w, pyrrole N-H).

2.3.5 Synthesis of 2-phenyl-*N*-[(*E*)-1*H*-pyrrol-2-ylmethylidene]ethan amine

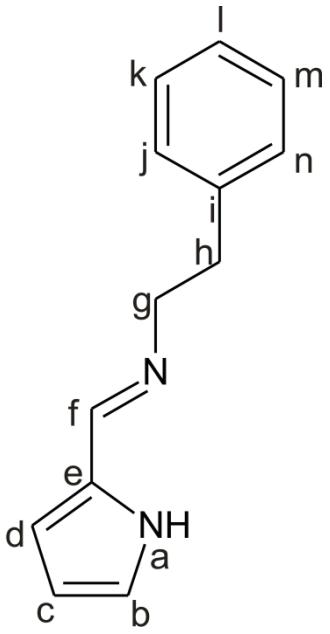

Figure 2.3.5: Structure and atom numbering scheme of 2-phenyl-*N*-[(*E*)-1*H*-pyrrol-2-yl methylidene]ethanamine (HL5).

Pyrrole-2-carboxaldehyde (1.000 g, 10.52 mmol) and phenylethylamine (6.371 g, 52.58 mmol) were ground together in a warm (85 °C) pestle and mortar. The resulting mixture was dissolved in DCM. Slow evaporation of the DCM solution yielded HL5 as a white powder (1.866 g, 89.5% yield). UV/vis (acetonitrile) [λ_{max}, nm; ε, mol^{-1} dm^3 cm^{-1}]: 279; 1.80×10^4. *Anal*. Calc. for ES^+: 198.12 m/z. *Exp*. ES^+: 199.1232 m/z ($M + H^+$). ^1H NMR (400 MHz, DMSO-*d6*, 298 K) [δ,ppm]: 2.89 (t, 2H, h), 3.70 (t, 2H, g), 6.07 (t, 1H, c), 6.39 (m, 1H, d), 6.89 (s, 1H, b), 7.15 – 7.29 (m, 5H, j, k, l, m, n), 8.00 (s, 1H, f), 11.35 (s, 1H, a). ^{13}C NMR (100 MHz, DMSO-*d6*, 298 K) [δ,ppm]: 37.24 (h), 64.20 (g), 108.73 (c), 113.26 (d), 121.93 (b), 125.87 (l), 128.17 (m, k), 128.81 (j, n), 129.94 (e), 140.01 (i), 151.97 (f). IR (cm^{-1}): 738.33 (s, pyrrole C-H bend), 1423.59 (s, C=C), 1642.87 (s, C=N), 2847.08 (w, imine C-H), 3162.43 (w, pyrrole N-H).

2.4 Synthesis of *tert*-ButylammoniumTetrachloroaurate(III)

Elemental gold pellets (170 mg, 0.863 mmol) were digested in a test tube in a 1:3 HCl_{conc}:HNO_{3conc} mixture, giving hydrogen tetrachloroaurate(III), as shown below in Equation 1.

$$Au(s) + HNO_3/HCl(excess) \rightarrow H[AuCl_4](aq) \quad ...1$$

The hydrogen tetrachloroaurate(III) was washed with concentrated HCl (35 %), while being stirred and heated to remove the acid. The gold(III) solution was diluted several times with deionised water, which was evaporated by heating, resulting in a concentrated solution of hydrogen tetrachloroaurate(III). After each addition of deionised water the pH of the vapours washing with deionised water removed all hydrochloric and nitric acid which remained evolved were tested (using litmus paper) until the vapours were no longer acidic. Removal of the majority of the water by heating, yielded a yellow solution of $H[AuCl_4]$. *Tert*-butylammonium hydrogensulphate (293 mg, 0.863 mmol) was added to the aqueous solution. This resulted in a bright yellow precipitate (Equation 2).

$$H[AuCl_4]\ (aq) + [Bu_4N][HSO_4]\ (s) \leftrightarrow [Bu_4N][AuCl_4]\ (s) + H_2SO_4\ (aq) \quad ...2$$

The $[Bu_4N][AuCl_4]$ was extracted into DCM (3 × portions), the organic portions were combined and dried over magnesium sulphate. The DCM was removed by rotary evaporation under reduced pressure, yielding a bright yellow crystalline solid (0.181 g, 36.0% yield).

2.5 Synthesis of Gold(III) Chelates

2.5.1 Synthesis of *cis*-dichloro-2-[(*E*)-(propylimino)methyl]pyrrol-1-ide aurate(III)

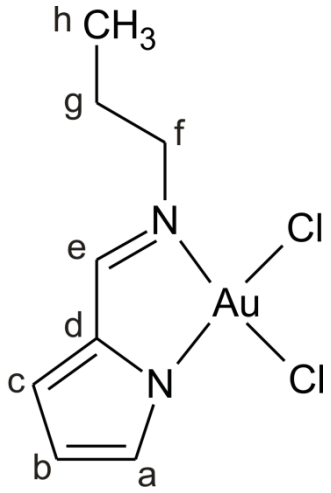

Figure 2.5.1: Structure and atom numbering scheme of *cis*-dichloro-2-[(*E*)-(propylimino) methyl]pyrrol-1-ide aurate(III) ([Au(L1)Cl_2]).

HL1 (0.023 g, 0.172 mmol) was dissolved in DCM (6 mL) and ethanol (2 mL). [Bu_4N][$AuCl_4$] (0.100 g, 0.172 mmol) was dissolved in DCM (2 mL) and added drop-wise to the heated solution of HL1. The resulting mixture was heated to reflux for three hours. The volume of the solution was reduced and [Au(L1)Cl_2] precipitated as a dark red solid. The precipitate was collected by filtration and dried (0.016 g, 23.0% yield). UV/vis (acetonitrile) [λ_{max}, nm; ε, mol^{-1} dm^3 cm^{-1}]: 294; 2.40 × 10^3, 364; 2.43 × 10^3. ^{1}H NMR (500 MHz, DMSO-*d6*, 298 K) [δ, ppm]: 0.89 (m, 3H, h), 1.75 (m, 2H, g), 3.75 (t, 2H, f), 6.40 (d, 1H, b), 7.01 (m, 1H, c), 7.28 (m, 1H, a), 8.26 (s, 1H, e). ^{13}C NMR (125 MHz, DMSO-*d6*, 298 K) [δ, ppm]: 10.80 (h), 24.23 (g), 60.01 (f), 110.98 (b), 122.24 (c), 135.07 (d), 136.44 (a), 165.23 (e). IR (cm^{-1}): 749.86 (s, pyrrole C-H bend), 1439.98 (s, C=C), 1576.10 (s, C=N), 2870.90 (w, imine C-H).

2.5.2 Synthesis of *cis*-dichloro-2-[(*E*)-(phenylimino)methyl]pyrrol-1-ide aurate(III)

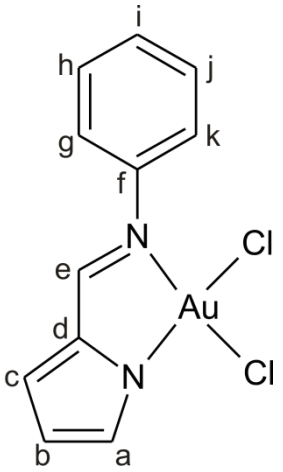

Figure 2.5.2: Structure and atom numbering scheme of *cis*-dichloro-2-[(*E*)-(phenylimino) methyl] pyrrol-1-ide aurate(III) ([$Au(L2)Cl_2$]).

HL2 (0.041 g, 0.241 mmol) was dissolved in DCM (10 mL) and ethanol (2 mL). [Bu_4N][$AuCl_4$] (0.102 g, 0.172 mmol) was dissolved in DCM (2 mL) and added drop-wise to the heated solution of HL2. The resulting mixture was heated to reflux for three hours and allowed to stand for ten days. The volume of the solution was reduced and [$Au(L2)Cl_2$] precipitated as a dark red solid. The precipitate was collected by gravity filtration and dried (0.023 g, 30.6% yield). UV/vis (acetonitrile) [λ_{max}, nm; ε, mol^{-1} dm^3 cm^{-1}]: 224; 2.55×10^4, 316; 7.81×10^3. ^{1}H NMR (500 MHz, DMSO-*d6*, 298 K) [δ, ppm]: 6.52 (q, 1H, b), 7.16 (m, 1H, c), 7.42 (m, 2H, g, k), 7.47 (m, 4H, a, h, i, j), 8.32 (s, 1H, e). ^{13}C NMR (125 MHz, DMSO-*d6*, 298 K) [δ, ppm]: 112.55 (b), 124.35 (c), 126.29 (g, k), 128.92 (h, j), 129.19 (i), 136.57 (d), 137.24 (a), 146.29 (f), 164.63 (e). IR (cm^{-1}): 736.51 (s, pyrrole C-H bend), 1440.21 (s, C=C), 1566.77 (s, C=N), 2870.57 (w, imine, C-H).

2.5.3 Synthesis of *cis*-dichloro-2-[(*E*)-(benzylimino)methyl]pyrrol-1-ide aurate(III)

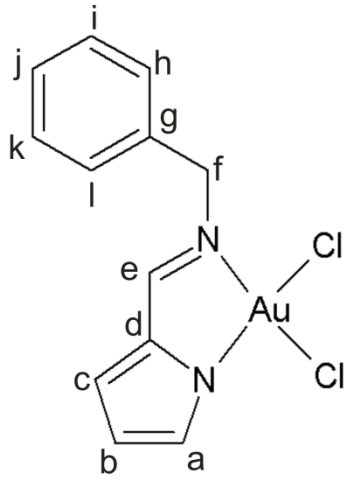

Figure 2.5.3: Structure and atom numbering scheme of *cis*-dichloro-2-[*(E)*-(benzylimino) methyl]pyrrol-1-ide aurate(III) ([Au(L3)Cl_2]).

HL3 (0.0317 g, 0.172 mmol) was dissolved in DCM (6 mL) and ethanol (2 mL) and heated. [Bu_4N][$AuCl_4$] (0.100 g, 0.172 mmol) was dissolved in DCM (2 mL) and added drop-wise to the heated HL3 solution. The mixture was refluxed for three hours and allowed to stand at room temperature for three days, the solvent volume was then reduced and [Au(L3)Cl_2] precipitated as a dark red/brown solid. The precipitate was collected by gravity filtration and dried (0.015 g, 18.4% yield). UV/vis (acetonitrile) [λ_{max}, nm; ε, mol^{-1} dm^3 cm^{-1}]: 297; 8.48 × 10^3, 368; 8.31 × 10^3. ^{1}H NMR (500 MHz, DMSO-*d6*, 298 K) [δ, ppm]: 5.04(s, 2H, f), 6.43 (m, 1H, b), 7.08 (m, 1H, c), 7.31 (m, 1H, a), 7.35 (m, 1H, a), 7.40 (m, 4H, i, j, k, l), 8.37 (s, 1H, e). ^{13}C NMR (125 MHz, DMSO-*d6*, 298 K) [δ, ppm]: 60.48 (f), 111.52 (b), 123.19 (c), 128.31 (j), 129.19 (h), 129.30 (a), 135.86 (k), 136.74 (i), 137.16 (d), 165.86 (e). IR (cm^{-1}): 736.48 (s, pyrrole C-H bond), 1440.20 (s, C=C), 1577.01 (s, C=N), 2869.00 (w, imine C-H).

2.5.4 Synthesis of *cis*-dichloro-2-[(*E*)-(naphthylimino)methyl]pyrrol-1-ide aurate(III)

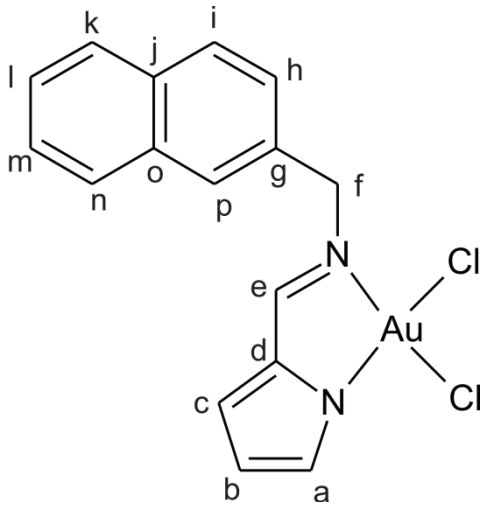

Figure 2.5.4: Structure and atom numbering scheme of *cis*-dichloro-2-[(*E*)-(naphthylimino) methyl] pyrrol-1-ide aurate(III) ([Au(L4)Cl_2]).

HL4 (0.031 g, 0.132 mmol) was dissolved in DCM (10 mL) and ethanol (2 mL). [Bu_4N][$AuCl_4$] (0.100 g, 0.172 mmol) was dissolved in DCM (2 mL) and added drop-wise to the heated HL4 solution. The mixture was refluxed for five hours and allowed to stand for two days, the solvent volume was reduced and [Au(L4)Cl_2] precipitated as a red solid. The precipitate was collected by gravity filtration and dried (0.031 g, 36.1% yield). UV/vis (acetonitrile) [λ_{max}, nm; ε, mol^{-1} dm^3 cm^{-1}]: 290; 1.31 × 10^4, 363, 1.03 × 10^4. ^{1}H NMR (500 MHz, DMSO-*d6*, 298 K) [δ, ppm]: 5.53 (s, 2H, f), 6.42 (q, 1H, b), 7.00 (m, 1H, c), 7.36 (m, 1H, a), 7.52 - 7.65 (m, 4H, h, I, m, n), 7.96 (m, 2H, l), 8.01 (m, 1H, o), 8.09 (m, 1H, e). ^{13}C NMR (125 MHz, DMSO-*d6*, 298 K) [δ, ppm]: 58.22 (f), 111.44 (b), 123.25 (o), 123.63 (c, i), 126.15 (m), 126.73 (n), 126.81 (l), 127.42 (p), 129.16 (d), 129.24 (h), 130.56 (j), 132.71 (k), 135.77 (g), 136.63 (a), 165.02 (e). IR (cm^{-1}): 748.78 (s, pyrrole C-H bond), 1439.22 (s, C=C), 1568.37 (s, C=N), 2958.73 (w, imine C-H).

2.5.5 Synthesis of *cis*-dichloro-2-[(*E*)-(phenylethylimino)methyl]pyrrol-1-ide aurate(III)

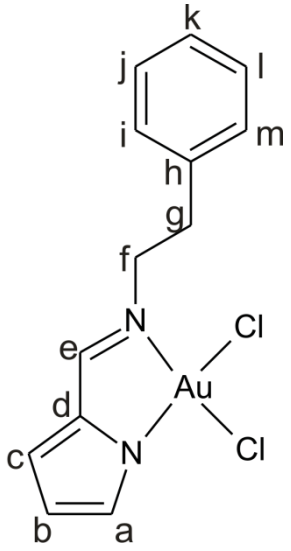

Figure 2.5.5: Structure and atom numbering scheme of *cis*-dichloro-2-[(*E*)-(phenyl ethylimino)methyl]pyrrol-1-ide aurate(III) ([Au(L5)Cl_2]).

HL5 (0.057 g, 0.288 mmol) was dissolved in DCM (10 mL) and ethanol (2 mL). [Bu_4N][$AuCl_4$] (0.100 g, 0.172 mmol) was dissolved in DCM (2 mL) and added drop-wise to the heated HL5 solution. The mixture was refluxed for five hours and allowed to stand for two days, the solvent volume was reduced and [Au(L5)Cl_2] precipitated as a dark red solid. The precipitate was collected by gravity filtration and dried (0.023 g, 28.8% yield). UV/vis (acetonitrile) [λ_{max}, nm; ε, mol^{-1} dm^3 cm^{-1}]: 292; 7.48 × 10^3, 366; 6.83 × 10^3. ^{1}H NMR (500 MHz, DMSO-*d6*, 298 K) [δ, ppm]: 3.06 (t, 2H, g), 3.99 (t, 2H, f), 6.39 (m, 1H, b), 6.98 (m, 1H, c), 7.24 (m, 1H, i), 7.26 - 7.34 (m, 5H, a, j, k, l, m), 8.05 (s, 1H, e). ^{13}C NMR (125 MHz, DMSO-*d6*, 298 K) [δ, ppm]: 36.82 (g), 59.47 (f), 111.15 (b), 122.48 (c), 127.13 (k), 128.86 (j), 129.45 (l), 135.57 (i), 136.42 (a, m), 138.18 (d), 165.16 (e). IR (cm^{-1}): 743.29 (s, pyrrole, C-H bond), 1443.89 (s, C=C), 1574.45 (s, C=N).

Chapter Three: Synthesis

3.1 Synthetic Arguments

3.1.1 Synthesis of Pyrrolide-Imine Schiff Base Ligands

Schiff base ligands are easily prepared by a condensation reaction between aldehydes or ketone and primary amines.[47] They can be successfully chelated to many different metals and allow for increased stability of metal ions in various oxidation states. Schiff bases are therefore very useful in a variety of applications.[47]

They can be synthesised using a variety of methods. These methods can be as simple as refluxing in a suitable solvent, or may require a Dean and Stark apparatus to remove water and drive the reaction forward. The synthesis of the pyrrolide-imine ligands with the exception of HL2, all use a synthetic technique which is very simple, but very effective. A solid state reaction whereby pyrrole-2-carboxaldehyde is ground with the desired amine (1:1 ratio) in a heated pestle and mortar is used. The reaction results in the generation of water, which spontaneously evaporates and the remaining product is the desired ligand in powder form (Scheme 3.1.1). The synthesis of HL2 differed in that it underwent a condensation reaction in ethanol. The reaction mixture was refluxed for twelve hours while the excess water was eliminated from the reaction using a Dean and Stark apparatus. Scheme 3.1.2 shows the mechanism for imine bond formation.

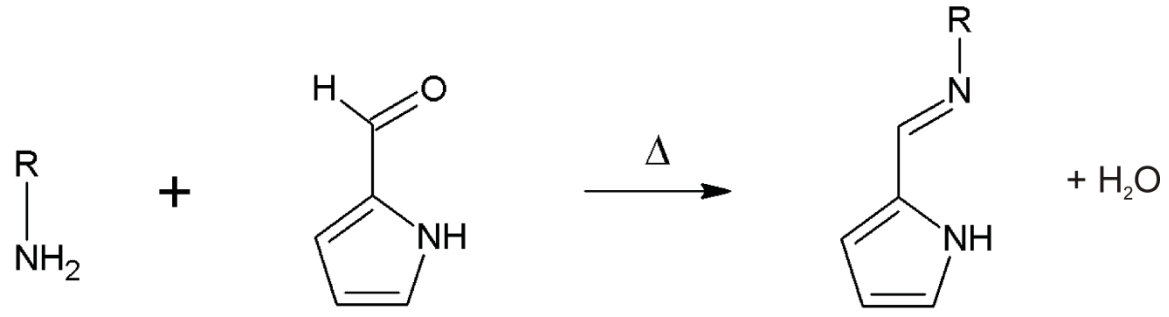

Scheme 3.1.1: Solid-state reaction, resulting in imine bond formation in the synthesis of the bidentate pyrrolide-imine ligands.[48] The R group represents any alkyl or aryl substituent.

The stability of the imine bond (and therefore formation of the solid product) is largely dependent on the substituent group. The pyrrolide-imine ligands in this work were all easily synthesised using the solid-state technique with the exception of ligand HL2, which required a twelve hour reflux using a Dean and Stark apparatus and three days of slow evaporation to allow for crystallisation of the product. The slow crystallisation process was necessary as the ligand formed a red oil, which contained many impurities, if the reaction mixture was not allowed to recrystallise slowly. This long crystallisation period and alternative method (use of the Dean and Stark) was required due to increased steric strain between the pyrrole β-H and imine H, this directly affected the rate of reaction and the ability of HL2 to crystallise. The steric strain within the molecule is further studied in chapter four.

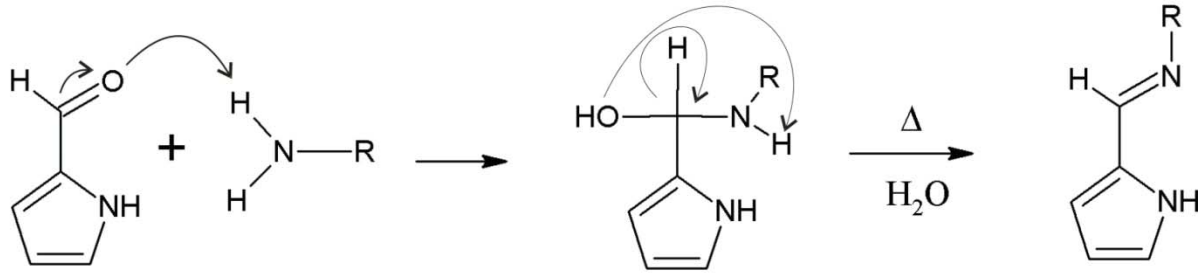

Scheme 3.1.2: Mechanism showing imine bond formation from pyrrole-2-carboxaldehyde and a primary amine.[48]

The synthetic method used for ligand HL2 in the formation of the imine bond was adapted from the reaction reported by Gomes *et al*, and was successful.[43] However, a preferable method of solid state synthesis has been reported by Akerman *et al*.[32] This was the chosen method in this work due to the shorter reaction time (< 15 minutes) compared to overnight refluxing. Additionally, the solid-state reactions resulted in moderately high yields of pure ligands which needed minimal post-synthetic work-up. The reflux in solvent method was only performed for the ligand HL2 due to the additional steric strain in the molecule, which rendered the solid-state technique ineffective.[11, 49-50] Both methods produced good yields, although the solid-state method was preferred because of its simplicity, speed and as it is a solvent-free reaction it can be considered environmentally friendly. The product from the solid state synthesis of HL4 is shown in the Figure 3.1.1 below.

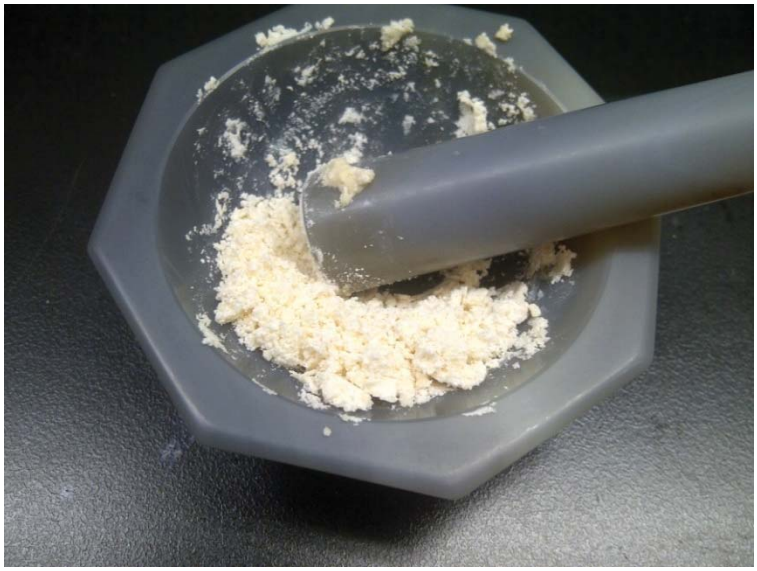

Figure 3.1.1: The solid product of HL4 after the solid-state reaction is performed.

A solid-state reaction is the physical grinding of two reactants together. In this case, pyrrole-2-carboxaldehye and the desired amine were ground in a pestle and mortar with no added solvent as the liquid amine acts as a solvent. The yields from the solid state reactions are high with all being > 85%. The benefit of solid-state reactions is the reduced cost due to the absence of solvents; therefore it can be classed as a green, environmentally friendly method as the by-product is water. This synthetic method is extremely fast and simple and requires no long hours of refluxing or expensive equipment. The product produced is in the solid state and is extremely pure, if reacted in a 1:1 ratio.

3.1.2 Metallation of ligands

The metallation of the pyrrolide-imine ligands was performed using $[Bu_4N_4][AuCl_4]$ as the source of the gold(III) ions.[51] The gold(III) salt chosen had specific advantages and characteristics which were favourable for this work. Firstly, the gold(III) salt is stable under atmospheric conditions, is not hygroscopic and is not as susceptible to reduction as other gold(III) salts such as $Na[AuCl_4]$ and $H[AuCl_4]$. Secondly, metal chelation by the ligand requires deprotonation of the pyrrole NH. The application of an acidic salt such as $H[AuCl_4]$ would hinder this deprotonation and slow the reaction. The chosen salt is neutral and so does not prevent deprotonation of the pyrrole NH.

$[Bu_4N_4][AuCl_4]$ was the source of the gold(III) cations in the reaction, in order to form the desired gold(III) chelates with dichloride substituents. This particular gold(III) salt is lipophilic; only being soluble in non-polar organic solvents.[52] The pyrrolide-imine ligands have a similar characteristic, once chelated to the gold(III) cation the chelates are neutral and still have a high affinity for non-polar solvents, this resulted in little to no gold(III) chelate precipitating out of solution. It was noticed that the chelate took several days to form and precipitate out of the reaction mixture. This is due to a slow chelation reaction. A potential risk about such a slow reaction time is the risk of forming gold colloids. In Figure 3.1.2 an image of red $[Au(L2)Cl_2]$ crystals in DCM/ethanol solution is shown, these took 10 days to form. The gold(III) salt is reacted with excess pyrrolide-imine ligand in order to shift the equilibrium of the chelation reaction towards the products. It is interesting to note that even with excess pyrrolide-imine ligand there would only be coordination of one ligand to the gold(III) ion, this suggests that the Au-Cl bond is relatively covalent and not kinetically labile. Similar patterns in the coordination behaviour of gold(III) have been previously reported. Wilson *et al.* have shown that even coordination of a potentially tetradentate ligand to the gold(III) ion results in a similar bidentate chelate with chloride ligands bound in a *cis* configuration.[18]

In this work, five novel, bidentate pyrrolide-imine gold(III) chelates were successfully synthesised. X-ray crystal structures of all five gold(III) chelates were determined. The crystal growth of the gold(III) chelates proved to be challenging. The most successful method was slow liquid diffusion by layering dichloromethane and hexane, this resulted in crystals being consistently produced. Excess gold starting material was removed by rinsing the crystals with acetonitrile and filtering by gravity filtration.

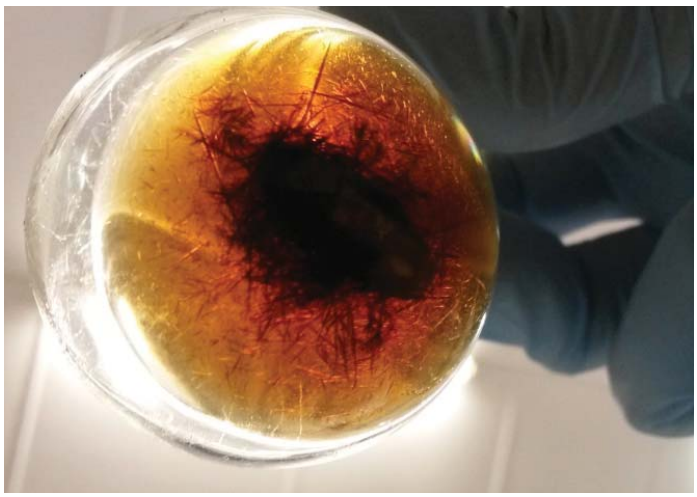

Figure 3.1.2: Formation of gold(III) crystalline material of $[Au(L2)Cl_2]$ after ten days.

Chapter Four: X-ray Crystallography

4.1 Introduction

4.1.1 Previously Reported Ligands

In this work five pyrrolide-imine ligands have been synthesised; four have been studied by X-ray crystallography. A search of the Cambridge Structural Database (CSD)[53] revealed that there are relatively few published X-ray structures related to the pyrrolide-imine ligands and bidentate pyrrolide-imine gold(III) chelates. The survey showed that only one of the pyrrolide-imine ligands synthesised in this work has been previously reported: ligand HL2. Table 4.1.1 gives details of some previously reported ligands which are closely related to the pyrrolide-imine ligands synthesised in this work. The structures of the previously reported ligands are illustrated in Figure 4.1.1.

Table 4.1.1: Reported X-ray crystal structures of pyrrolide-imine ligands.

CSD Ref. Code	Compound Name	Lit. Ref.
AWIKAT	4-Fluoro-*N*-(1*H*-pyrrol-2-ylmethylidene)aniline	43
AWIKEX	2-[(1*H*-pyrrol-2-ylmethylidene)amino]benzonitrile	43
BAWHEO	4-tert-Butyl-*N*-(1*H*-pyrrol-2-ylmethylene)aniline	54
CUKHUM	2-((Phenylimino)methyl)pyrrole	31
CUKHUM01	2-((Phenylimino)methyl)pyrrole	31
CUKJEY	2-((2,6-Diisopropylphenylimino)methyl)pyrrole	8
EWOLUX	4-Isopropyl-*N*-(2-pyrrolylmethylene)aniline	8
JETLIE	2-(((1*H*)-Pyrrol-2-ylmethylene)amino)phenol	55
SUZFUP	2,3-Dimethyl-*N*-(1*H*-pyrrol-2-ylmethylene)aniline	56
VIYWUW	4-((1*H*-Pyrrol-2-ylmethylene)amino)phenol	30

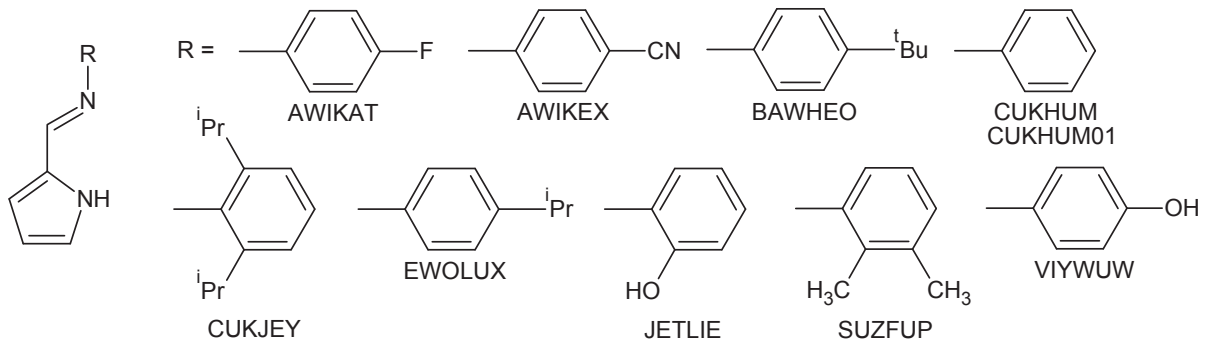

Figure 4.1.1: Structures of previously reported, bidentate N2-donor pyrrolide-imine ligands.

The pyrrolide-imine ligand HL2 (CSD reference CUKHUM) crystallised in the orthorhombic space group *Pbca* with a hydrogen-bonded dimer in the asymmetric unit and sixteen molecules in the unit cell ($Z = 16$).[31] This compound has been studied as two different polymorphs (CUKHUM and CUKHUM01). The second polymorph, CUKHUM01 crystallised in the monoclinic space group $P2_1/c$. Despite the different unit cell parameters and space groups both polymorphs exhibit the complementary hydrogen bonding ubiquitous in this class of ligand. The ligand HL2 was characterised by X-ray crystallography in this work, but showed no structural difference to that previously reported. A single molecule from the asymmetric unit of CUKHUM is shown below in Figure 4.1.2.

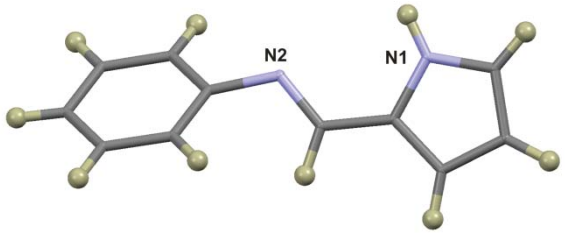

Figure 4.1.2: A partially labelled view of CUKHUM at 150K. All atoms have been rendered as spheres of arbitrary radius.

The X-ray crystal structure of CUKHUM, Figure 4.1.2, shows the geometry around the imine group is *trans*. This conformation is favoured over the *cis* isomer, as the *cis* isomer would have unfavourable steric interactions between the aromatic α pyrrole hydrogen atom and the imine hydrogen atom.[31] Since the molecule is a conjugated π-system it would be expected to be planar, this is not the case. The phenyl ring exhibits a torsion angle of 47.0(1)° relative to the pyrrole ring. It would seem that the deviation from the expected planar geometry is to alleviate unfavourable non-bonded repulsion between the imine hydrogen atom and the *o*-hydrogen atoms of the phenyl ring. A similar deviation from planarity is observed in all variants of HL2 and is attributed to the same non-bonded repulsion. The average bond lengths about the imine carbon atom, C4-C5 and C5-N2 measure 1.482(1) and 1.287(1) Å, respectively. While the C4-C5-N2 bond angle measures 123.84(7)°. These values highlight the sp^2 hybridised nature of imine carbon atom and are in good agreement with those of the structure of HL2 determined in this work. The structure of HL2 is discussed in section 4.3.1.

The X-ray crystal structures of the previously reported ligands show similar characteristics to those in this work. They all comprise a pyrrole ring bonded to various aromatic appendages through an imine bond. The structures all exhibit complementary hydrogen bonding between the pyrrole NH and the imine nitrogen of an adjacent molecule. In some cases the ligands show different hydrogen bonding motifs as a consequence of various functional groups on the aromatic moieties. These will be discussed.

Figure 4.1.3 illustrates the hydrogen bonding between the pyrrole NH and imine nitrogen atom of an adjacent molecule (the contents of the asymmetric unit of CUKHUM). The hydrogen bond parameters (bond lengths and bond angles) are summarised in Table 4.1.2. Most ligands in this class of compounds exhibit the same hydrogen bonding motif.

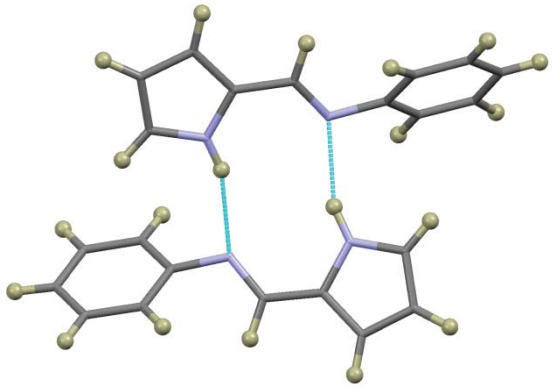

Figure 4.1.3: Complementary hydrogen bonding between the pyrrole NH (hydrogen bond donor) and the imine nitrogen atom (hydrogen bond acceptor) of CUKHUM. Most derivatives of this ligand exhibit similar hydrogen bonding.

Table 4.1.2: Hydrogen bond lengths (Å) and bond angles (°).

	D–H	H···A (Å)	D···A (Å)	D–H···A (°)
N1A–H101···N2B	0.900(1)	2.140(1)	2.990(2)	156(1)
N1B–H102···N2A	0.880(2)	2.160(2)	3.003(1)	161(1)

This $N_{pyrrole}$–H···N_{imine} hydrogen bonding motif is typical of this class of ligands.[4, 11, 26, 49, 57] The predictability of this hydrogen bonding motif suggests that it could be used to stabilise porous three-dimensional networks for use in gas storage applications.[8]

The hydrogen bond lengths reported for this hydrogen bonding motif are all shorter than the sum of the van der Waals radii of the interacting atoms, the mean H···N_{imine} bond length of the previously reported structures measures 2.16(6) Å.[26] Although hydrogen bond length does not necessarily correlate linearly with bond strength due to packing constraints in the lattice[58] this mean bond length is shorter than that associated with C–H···O interactions.[11] In general, C–H···O interactions are considered to be weak interactions, since the $N_{pyrrole}$–H···N_{imine} bond lengths are shorter than the mean associated with C–H···O interactions (>2.20 Å) and the $N_{pyrrole}$–H···N_{imine} bond angles do not deviate significantly from ideality (180°) they are likely to be moderately strong hydrogen bonds.

Complementary $N_{pyrrole}$–H···N_{imine} hydrogen bonding is evident in most pyrrole-imine structures, indicating a stable hydrogen bonding motif. However, structures with alternative hydrogen bonding moieties such as JETLIE and VIYWUW, which have hydroxyl groups in the *ortho* and *para* positions of the phenyl ring, respectively show preferential hydrogen bonding to these functional groups. This suggests that although the pyrrole NH is a good hydrogen bond donor the hydroxyl group, with the more electronegative oxygen atom, leads to more stable hydrogen bonds. The hydroxyl group in the *ortho* position in JETLIE leads to a two-dimensional hydrogen bonded network as opposed to a dimeric structure. The hydroxyl group in the *para* position leads to a one-dimensional hydrogen-bonded network (Figure 4.1.4).

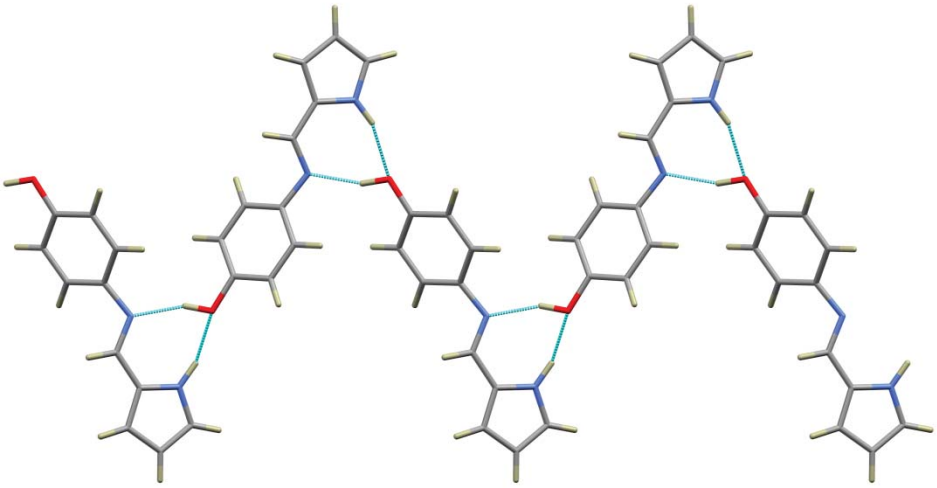

Figure 4.1.4: One dimensional hydrogen-bonded network of VIYWUW viewed down the *c* -axis. The network is supported by hydrogen bonds between the pyrrole NH, the imine nitrogen atom and the hydroxyl group.

4.1.2 Previously Reported Metal Chelates

A survey of previously reported X-ray structures related to the gold(III) chelates synthesised in this work was carried out using, the Cambridge Structural Database (CSD).[53] The survey showed that none of the bidentate pyrrolide-imine gold(III) chelates have been previously synthesised therefore all structures reported herein are novel. Although the gold(III) chelates in this work are novel, several closely related gold(III) chelates with *N*,*N*'-donor bidentate ligands have been previously reported. These structures are described in Table 4.1.3.

Table 4.1.3: Reported X-ray crystal structures of pyrrolide-imine metal chelates and structurally related gold(III) chelates.

CSD Ref. Code	Compound Name	Lit. Ref.
CESMUJ	Dichloro-(2-(*N*-isopropylaminomethyl)pyridine)-gold(III) tetrachloroaurate	19
ERAHUA	bis(*N*-Benzyl-2-pyrrolylcarbaldimine-*N,N′*)-copper(II)	59
KUMYIB	Dichloro-(4,4'-dimethoxy-2,2'-bipyridine)-gold hexafluorophosphate	60
QIRRAK	Dichloro-(1,10-phenanthroline)-gold(III) chloride monohydrate	61
SAYMUC	(m2-2-(pyridin-2-yl)-1*H*-benzimidazolato)-trichloro-di-gold	51
WIQYIG	*cis*-Dichloro{(pyridin-2-ylcarbonyl)[2-[(pyridin-2-ylcarbonyl)amino]ethyl]azanido}gold(III)	18
WIQYOM	*cis*-Dichloro{(pyridine-2-yl-carbonyl)[3-[(pyridin-2-ylcarbonyl)amino]propyl]azanido}gold(III)	18
WIQYUS	*cis*-Dichloro[(4-methoxyphenyl)(pyridin-2-ylcarbonyl)azanido]gold(III)	18
WIQZAZ	*cis*-dichloro{(isoquinolin-3-ylcarbonyl)[2-[(isoquinolin-3-ylcarbonyl)amino]phenyl]azanido}gold-(III)	18

The bis(pyrrolide-imine) copper(II) chelate (ERAHUA, Figure 4.1.5) has a nominally square planar coordination sphere with two bidentate ligands chelated to the copper(II) ion in a *trans* configuration. The Cu–$N_{pyrrole}$ and Cu–N_{imine} bond lengths measure 1.965(2) and 2.038(2) Å, respectively. The phenyl ring of the ligand is in perpendicular orientation relative to the coordination sphere. The torsion angle of the phenyl ring relative to the coordination sphere measures 84.4(2)°. Seemingly, the near perpendicular orientation is favoured as it alleviates steric strain between the phenyl and pyrrole rings of the chelate.

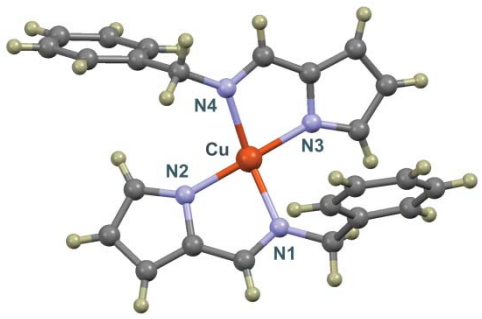

Figure 4.1.5: Partially labelled diagram of ERAHUA, showing the nominally square planar coordination geometry and the *trans* configuration of the ligands. Atoms have been rendered as spheres of arbitrary radius.

The most relevant structures are those reported for the gold(III) chelates of the pyridine-imine ligands, SAYMUC[51] and CESMUJ[19]. These structures are shown in Figure 4.1.6 and 4.1.7. These structures highlight the square planar coordination geometry of the gold(III) ion as well as the displacement of the aromatic appendage (which is bonded to the pyridine ring through an imine bond) from planarity.

The gold(III) ion of CESMUJ is stabilised by a bidentate pyridyl-imine ligand. The other two coordination sites are occupied by chloride ligands. The bidentate ligand and the two chloride ligands form a nominally square planar coordination sphere. The coordination geometry is consistent with the d^8 electronic configuration of the gold(III) ion. The vacant $d(x^2- y^2)$ orbitals of the gold(III) ion favour a square planar coordination geometry. Chelation of the gold(III) ion by a neutral *N*,*N*' donor ligands and two anionic chloride ligands yields a monocationic complex. The complex has been isolated as the tetrachloroaurate(III) salt. Isolation of cationic gold(III) chelates as either the tetrachloroaurate(III) or dichloroaurate(I) complex salts is a relatively common occurrence and greatly reduces the solubility of the complex salts.[19] These pyridyl-imine chelates have a coordination sphere closely resembling that of the gold(III) chelates presented in this work.

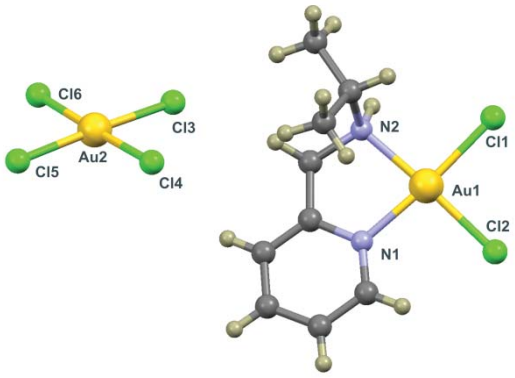

Figure 4.1.6: Partially labelled X-ray crystal structure of CESMUJ showing the square planar coordination geometry of the gold(III) ion.

The Au–Cl1 and Au–Cl2 bond distances for the above chelate measure 2.266(4) and 2.264(2) Å, respectively. The Au–N1 and Au–N2 bonds measure 2.024(7) and 2.046(7) Å, respectively. The N1–Au–N2 angle measures 82.7(3)°. This bond angle is more acute than the ideal bond angle for a square planar coordination geometry. This is attributed to the relatively small bite angle of the bidentate ligand. Similar traits were also observed in the SAYMUC complex, shown in Figure 4.1.7. The Au–N1 and Au–N2 bonds measure 1.97(3) and 2.05(1) Å, respectively. The N1–Au–N2 angle measures 78.7(8)°.

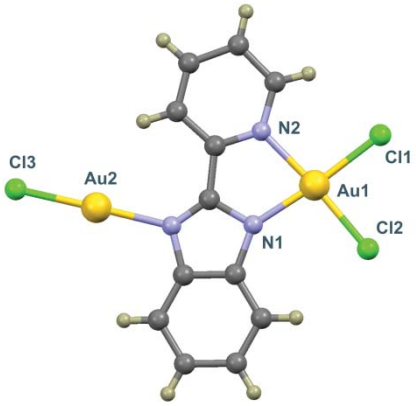

Figure 4.1.7: Partially labelled X-ray crystal structure of SAYMUC showing the square planar coordination geometry of the gold(III) ion.

The number of gold(III) chelates with a *cis*-chloride configuration[12-15] would suggest that this geometry is particularly stable. Seemingly after coordination of a single bidentate N_2-donor ligand the chloride ligands become substitution-inert. This statement is strongly supported by the fact that Wilson *et al*. reported a *cis*-chloride complex after attempted chelation of dianioinc tetradentate ligands (Figure 4.1.8).[18]

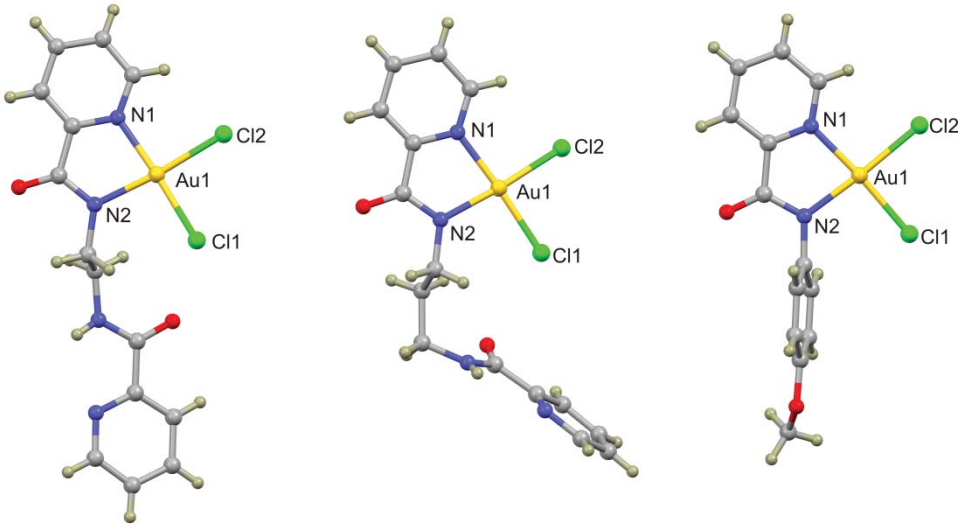

Figure 4.1.8: Structures of WIQYIG, WIQYOM and WIQYUS[15] illustrating the preference for gold(III) chelates to adopt a *cis*-chloride configuration even in the presence of tetradentate N_4-donor ligands.

4.1.3 Objectives

The main objective of the X-ray crystal diffraction experiments is to determine the solid state structures of the novel pyrrolide-imine ligands and bidentate pyrrolide-imine gold(III) chelates. This could expand the limited available literature relating to gold(III) chelates. These solid-state structures could also provide insight into solid-state reactions as well as valuable information as to whether these chelates will be effective DNA intercalators.

4.2 Experimental

The X-ray data were recorded on a Bruker Apex Duo diffractometer equipped with an Oxford Instruments Cryojet operating at 100(2) K and an Incoatec microsource operating at 30 W power. Crystal and structure refinement data are given in Table 4.6.1 and 4.6.2. In all cases the data were collected with Mo Kα (λ = 0.71073 Å) radiation at a crystal-to-detector distance of 50 mm. The data collections were performed using omega and phi scans with exposures taken at 30 W X-ray power and 0.50° frame widths using APEX2. [62] The data were reduced with the programme SAINT [62] using outlier rejection, scan speed scaling, as well as standard Lorentz and polarisation correction factors. A SADABS semi-empirical multi-scan absorption correction [62] was applied to the data. Direct methods, SHELXS-97 [63] and WinGX [64] were used to solve all structures. All non-hydrogen atoms were located in the difference density map and refined anisotropically with SHELXL-97. [63] All hydrogen atoms were included as idealised contributors in the least squares process. Their positions were calculated using a standard riding model with C–$H_{aromatic}$ distances of 0.95 Å and U_{iso} = 1.2 U_{eq} and C–$H_{methylene}$ distances of 0.99 Å and U_{iso} = 1.2 U_{eq}. The pyrrole N-H atoms were located in the difference density map and refined isotropically.

In the case of the gold(III) chelates there is residual electron density in the E-map. These peaks are located near the gold(III) ion and are the result of the strong absorption by the metal ion. This is most evident in [Au(L3)Cl_2] which has a peak of 3.92 eÅ^{-3} located 2.45 Å from C10. The data completeness for [Au(L4)Cl_2] is less than the ideal as data were collected for an orthorhombic unit cell based on preliminary measurements, but the lattice did not have symmetry consistent with the orthorhombic crystal system and was solved as monoclinic.

The atomic coordinates, crystal data and crystal refinement tables for the ligands and metal chelates are available in **Appendix B**. All crystallographic information files for the ligands and metal chelates as well as the IUCR CIFcheck reports can be found in **Appendix C**.

4.3 X-ray Crystallography of Ligands

4.3.1 X-ray Structural Analysis of HL2

The X-ray crystal structure of HL2 was elucidated from the data collected at 100 K. The ligand crystallised in the orthorhombic space group *Pbca*, with the asymmetric unit containing two molecules, $Z = 16$. The structure has been previously reported, but minimal discussion of geometric parameters were discussed in that report.[31] The ligand structure is shown below in Figure 4.3.1.

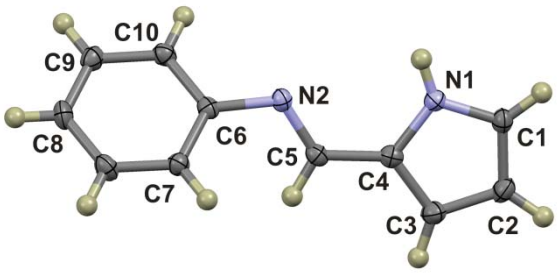

Figure 4.3.1: Labelled X-ray structure of HL2, shown at the 50% probability level. Hydrogen atoms have been rendered as spheres of arbitrary radius.

The C4–C5 and C5–N2 bond lengths measure 1.427(2) and 1.287(2) Å, respectively. The C4–C5–N2 bond angle measures 124.9(1)°. These bond lengths and angles highlight the sp^2 hybridised nature of the imine carbon atom. One would expect HL2 to be a planar molecule as a planar configuration would allow for π-conjugation throughout the molecule, but this is not the case. The N1–C4–C6–C7 torsion angle measures 57.3(1)°, this angle illustrates how the molecule deviates from planarity; the phenyl ring and pyrrole-imine moiety do not occupy the same plane. This unexpected configuration is attributed to the potential steric strain between the hydrogen atoms of C5 and C7 that would be caused by a planar configuration. Figure 4.3.2 highlights the atoms between which there would be steric strain if the geometry were planar.

A dimeric supramolecular structure is stabilised by complementary hydrogen bonding between the pyrrole NH and the imine nitrogen atom. This hydrogen bonding motif will be discussed in more detail in section 4.3.5.

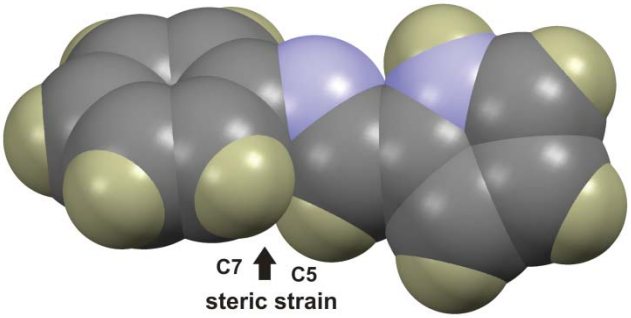

Figure 4.3.2: Partially labelled space-filling view of HL2 showing steric strain between the hydrogen atoms of C5 and C7.

4.3.2 X-ray Crystal Structural Analysis of HL3

The molecule HL3 crystallised in the monoclinic space group $P2_1/n$. The unit cell contains eight molecules with each asymmetric unit containing a hydrogen-bonded dimer. These hydrogen-bonded dimers are shown in Figure 4.3.4, a single molecule from the asymmetric unit of HL3 is shown below in Figure 4.3.3.

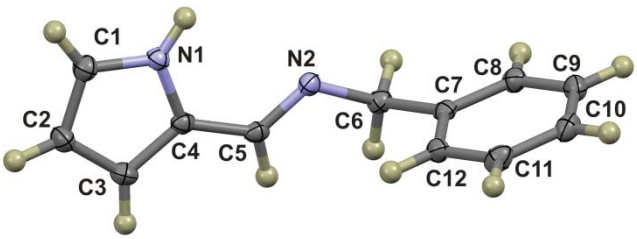

Figure 4.3.3: Labelled thermal ellipsoid plot of HL3, shown at the 50% probability level. Hydrogen atoms have been rendered as spheres of arbitrary radius.

The structure of HL3 (Figure 4.3.3) is similar to the previously reported structure of HL2, the only difference being a methylene group located between the imine nitrogen atom and phenyl ring. This methylene spacer allows for increased rotation, resulting in the aromatic ring lying approximately perpendicular to the pyrrolide-imine moiety, with an N1–C4–C7–C8 torsion angle of 92.54(9)°.

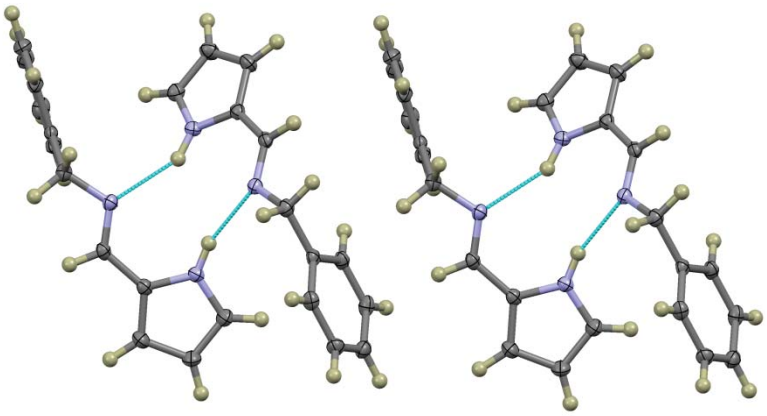

Figure 4.3.4: Dimers of HL3 stabilised by complementary hydrogen bonding (hydrogen bonds shown as dashed blue lines). Adjacent dimers are related by crystallographically imposed inversion symmetry, but are not linked by any significant intermolecular interaction.

As in the case of HL2 the molecules have crystallised as discrete dimers supported by complementary hydrogen bonds between the pyrrole NH and imine nitrogen atoms. Adjacent dimers are related by crystallographically imposed inversion symmetry. There are no notable intermolecular interactions linking the adjacent dimers into an extended network. The hydrogen bonds will be discussed in more detail in section 4.3.5.

4.3.3 X-ray Structural Analysis of HL4

The ligand HL4 crystallised in the triclinic space group *P*-1with a single molecule in the asymmetric unit and $Z = 2$. The content of the asymmetric unit is shown in Figure 4.3.5 below.

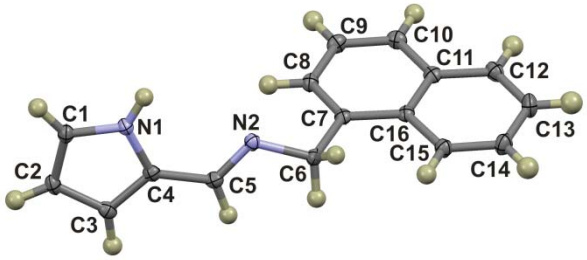

Figure 4.3.5: Labelled thermal ellipsoid plot of HL4, shown at the 50% probability level. Hydrogen atoms have been rendered as spheres of arbitrary radius.

The bonds of the pyrrole ring: N1–C1, C1–C2 and C2–C3 measure 1.362(2), 1.376(1) and 1.411(2) Å, respectively. These bonds compare favourably to those of previously reported structures.[2-8] The imine C=N bond measures 1.277(1) Å and the C–C=N bond angle measures 124.1(1)°. Figure 4.3.5 shows that the naphthyl region lies perpendicular to the pyrrolide-imine group, with an N1–C4–C7–C8 torsion angle of 70.6(1)°.The perpendicular orientation of the naphthyl rings relative to the pyrrole rings allows two adjacent molecules to approach more closely, maximising the hydrogen bonding interactions.

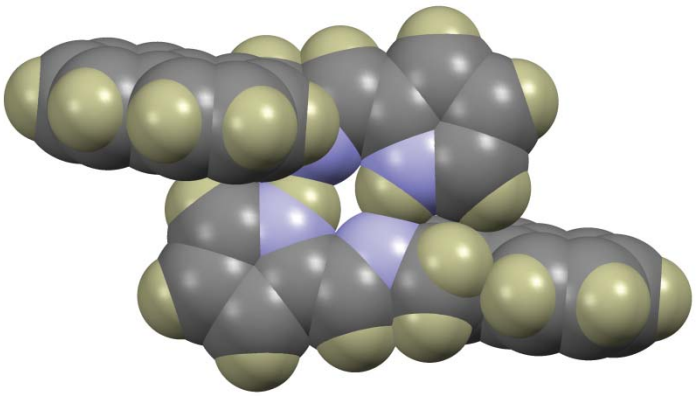

Figure 4.3.6: Spacefilling model of HL4 showing how the perpendicular orientation of the naphthyl rings allows the molecules of the hydrogen-bonded dimer to approach more closely, enabling hydrogen bonding.

4.3.4 X-ray Structural Analysis of HL5

The ligand HL5 crystallised in the monoclinic space group $P2_1/c$, with four molecules in the unit cell ($Z = 4$) and a single molecule in the asymmetric unit as shown in Figure 4.3.7 below.

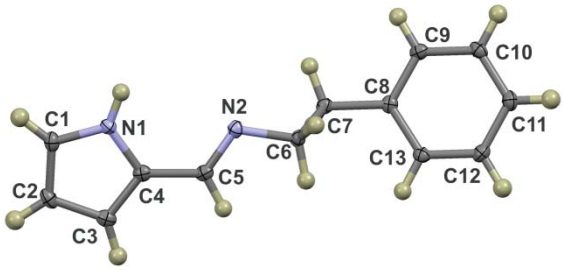

Figure 4.3.7: Labelled thermal ellipsoid plot of HL5, shown at the 50% probability level. Hydrogen atoms have been rendered as spheres of arbitrary radius.

Figure 4.3.7 shows that the aromatic region is approximately co-planar with the pyrrolide-imine group with a torsion angle of 3.4(1)°, this is attributed to the two methylene spacers which gives additional degrees of freedom allowing for comparatively free rotation. The C4–C5 and C5–N2 bond lengths measure 1.441(2) and 1.271(2) Å, respectively. The C5–N2 bond length is relatively short, illustrating the double bond character. These distances are in accord with previously reported ligands.[31] The C4–C5–N2 bond angle measures 125.0(1)° which is significantly larger than that measured for ligands HL2, HL3 and HL4. This may be attributed to the extended two methylene chain.

4.3.5 Hydrogen-Bonded Dimers

The four ligands that were studied by X-ray crystallography all exhibit complementary hydrogen bonding between the pyrrole NH and the imine nitrogen atom. The pyrrole NH acts as the hydrogen-bond donor while the imine nitrogen atom of an adjacent molecule acts as a hydrogen-bond acceptor. These hydrogen bonds link two adjacent molecules into a dimeric supramoleular structure (Figure 4.3.8).

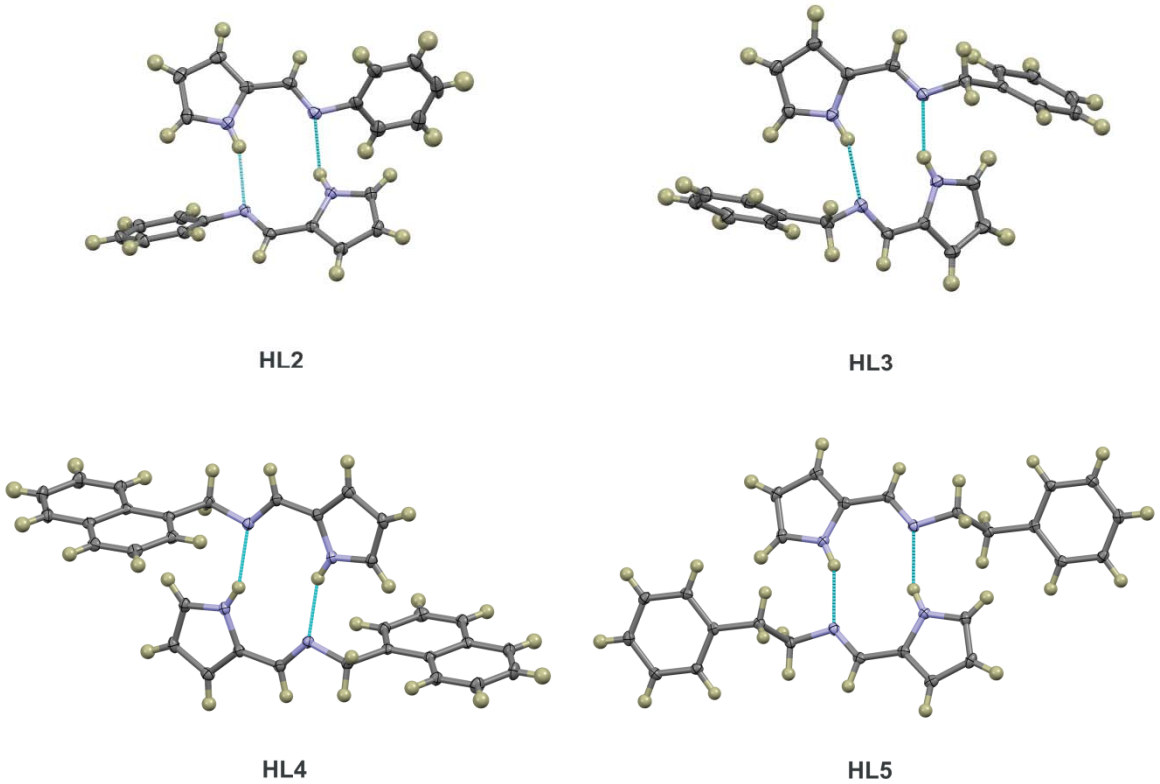

Figure 4.3.8: Dimeric structures of the pyrrolide-imine ligands HL2, HL3, HL4 and HL5. The dimeric structures are supported by hydrogen bonding interactions between the pyrrole NH and imine nitrogen atom. HL4 and HL5 are inversion dimers (C_i symmetry); the dimeric structures of HL2 and HL3 are of C_1 symmetry.

The dimeric structures are supported by hydrogen bonds between the pyrrole NH (hydrogen bond donor) and imine nitrogen atom (hydrogen bond acceptor). The dimeric structures are linked by weak C–H···π interactions forming an extended network. Figure 4.3.8 shows that these relatively strong hydrogen bonds exist in all four ligands. These hydrogen bonds yield a ten-membered hydrogen-bonded ring. The $N_{pyrrole}$–H···N_{imine} hydrogen bonding is a common feature in pyrrolide-imine ligands.[2-8,32] The hydrogen bond lengths and bond angles associated with the dimeric structures are summarised in Table 4.3.1.

Table 4.3.1: Hydrogen bond lengths (Å) and bond angles (°).

	D–H	H···A (Å)	D···A (Å)	D–H···A (°)
HL2				
N1A–H101···N2B	0.859(1)	2.188(1)	2.984(1)	153.93(7)
N1B–H102···N2A	0.860(1)	2.185(1)	3.000(1)	158.09(1)
HL3				
N1A–H101···N2B	0.880(1)	2.217(1)	3.025(5)	152.52(6)
N1B–H102···N2A	0.881(1)	2.292(1)	3.073(1)	147.88(6)
HL4				
N1–H101···N2	0.879(8)	2.164(1)	2.996(1)	157.49(7)
HL5				
N1–H101···N2	0.880(1)	2.166(1)	2.994(2)	156.55(8)
Mean	0.873(2)	2.202(5)	3.012(1)	154.41(6)

It is generally accepted that the strength of a hydrogen bond is not necessarily reflected in the distance of the interaction. For example a shorter D–H···A distance does not necessarily mean that it is a strong hydrogen bond, this is because of crystal packing effects, orientation angles and other intermolecular interactions.[58] However, these are relatively short bond lengths and the bond angles do not deviate too significantly from ideality (180°) this would suggest that they are likely to be moderately strong interactions.

However, structures with alternative hydrogen bonding moieties such as JETLIE and VIYWUW,[5,7] which have hydroxyl groups in the *ortho* and *para* positions, respectively show preferential hydrogen bonding to these functional groups. This suggests that although the pyrrole NH is a good hydrogen bond donor the hydroxyl group with the more electronegative oxygen atom leads to more stable hydrogen bonds.

4.4 X-ray Structures of Gold(III) Complexes

4.4.1 X-ray Structural Analysis of [Au(L1)Cl_2]

The gold(III) complex [Au(L1)Cl_2] crystallised in the orthorhombic space group *Pca*2_1. The asymmetric unit (Figure 4.4.1) contains one chelate, $Z = 4$. A search of the CSD showed that no gold(III) chelates of any bidentate pyrrolide-imine ligands have been previously reported, making all the following gold(III) complexes novel.

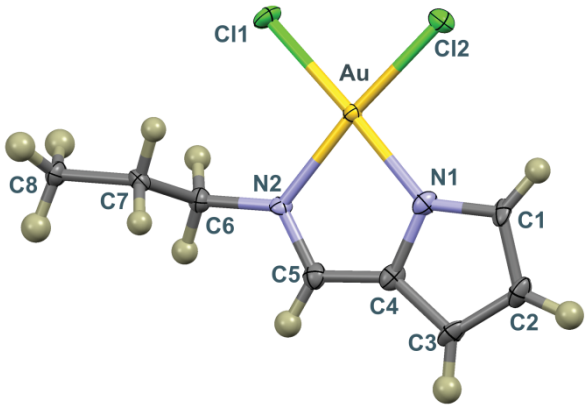

Figure 4.4.1: Thermal ellipsoid plot of the gold(III) chelate [Au(L1)Cl_2] shown at the 50% probability level. Hydrogen atoms have been rendered as spheres of arbitrary radius.

Metal chelation with concomitant deprotonation of the pyrrole NH affords a monoanionic, bidentate *N*,*N*' donor ligand, this ligand occupies two of the available coordination sites of the gold(III) ion. The other two coordination sites of the metal are occupied by two chloride ligands in a *cis* configuration affording a square planar, neutral metal chelate. The preference of gold(III) to form a square planar coordination geometry is attributed to the d^8 electronic configuration with vacant d(x^2-y^2) orbitals. Selected bond lengths and bond angles which describe the coordination sphere of the metal ion are summarised in Table 4.4.1.

Table 4.4.1: Summary of the coordination sphere bond lengths and bond angles of [Au(L1)Cl_2].

Bond	Length (Å)	Bond	Angle (°)
Au–N1	1.993(4)	N1–Au–N2	81.02(2)
Au–N2	2.035(6)	Cl1–Au–Cl2	91.08(6)
Au–Cl1	2.275(1)	N1–Au–Cl2	92.7(2)
Au–Cl2	2.276(2)	N2–Au–Cl1	95.3(2)

It is interesting to note that the Au–$N_{pyrrole}$ bond length is significantly shorter than the Au–N_{imine} bond length. This is attributed to the imine having a neutral charge therefore a weaker bond to the gold(III) ion is formed compared to the pyrrole nitrogen which has a negative charge which results in a stronger bond to the gold(III) ion. This stronger bond manifests as a shorter bond length.

The pyrrolide-imine moiety, chloride ligands and gold(III) ion are all co-planar, the propyl substituent has free rotation around the N2–C6 bond with minimal steric hindrance and is displaced from the mean plane defined by the gold(III) ion and the four coordinating atoms. The structure exhibits Au···π interactions with a distance of 3.454(1) Å between the 5-atom mean plane of the pyrrole ring and the gold(III) ion of an adjacent molecule, this is illustrated in Figure 4.4.2. This type of interaction stems from the fact that the gold(III) ion is relatively electron deficient and can therefore accept electron density from neighbouring aromatic systems. This can be considered a Lewis acid/base interaction. As electron rich DNA is the intended cellular target of the gold(III) chemotherapeutic agents the presence of Au···π interactions in the solid state structures is an encouraging result. It shows the complexes will form favourable interactions with electron rich π systems and they are therefore likely to interact favourably with DNA.

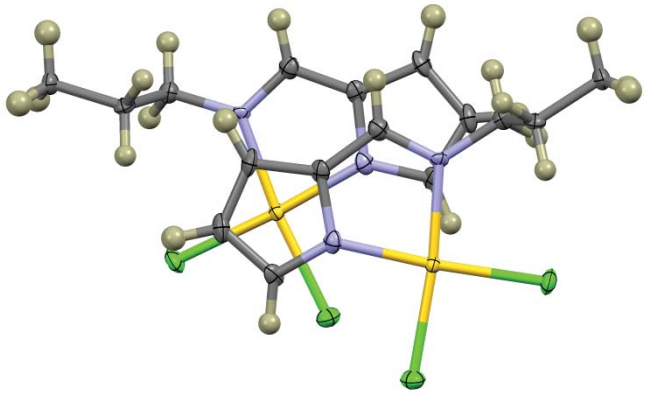

Figure 4.4.2: X-ray crystal structure of [Au(L1)Cl_2] showing Au···π interactions between the pyrrole rings and gold(III) ion of two adjacent chelates.

4.4.2 X-ray Structural Analysis of [Au(L2)Cl_2]

The gold(III) chelate [Au(L2)Cl_2] crystallised in the monoclinic space group $P2_1/c$ with a single molecule in the asymmetric unit and Z = 4 (Figure 4.4.3). The gold(III) chelate exhibits square planar geometry which is consistent with the former gold(III) chelate, [Au(L1)Cl_2]. The geometrical parameters which illustrate the nominally square planar coordination geometry of the chelate are summarised in Table 4.4.2.

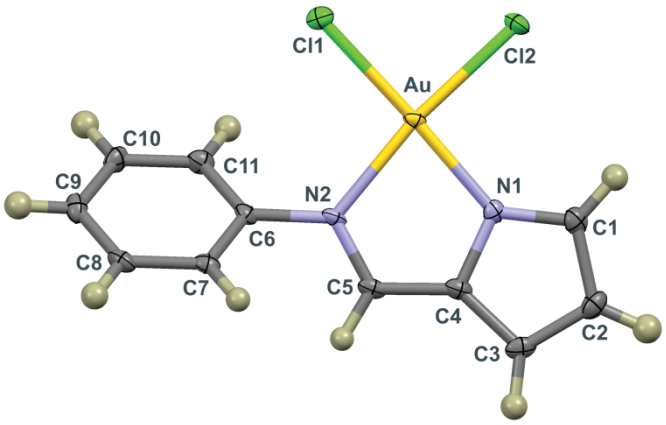

Figure 4.4.3: Thermal ellipsoid plot of the gold(III) chelate $[Au(L2)Cl_2]$ shown at the 50% probability level. Hydrogen atoms have been rendered as spheres of arbitrary radius.

Table 4.4.2: Summary of the bond lengths and bond angles of $[Au(L2)Cl_2]$.

Bond	Length (Å)	Bond	Angle (°)
Au–N1	1.985(4)	N1–Au–N2	80.8(1)
Au–N2	2.045(3)	Cl1–Au–Cl2	90.1(1)
Au–Cl1	2.2834(9)	N1–Au–Cl2	92.9(4)
Au–Cl2	2.273(1)	N2–Au–Cl1	95.6(4)

Table 4.4.2 shows again that the Au–$N_{pyrrole}$ bond length is significantly shorter than the Au–N_{imine} bond length due to the imine having a neutral charge therefore a weaker bond is formed compared to the pyrrole nitrogen, which carries a negative charge which contributes to a stronger bond which results in a shorter bond length. The N1-Au-N2 bond angle is significantly more acute than the ideal angle for a square planar coordination geometry. This is a consequence of the relatively small bite angle of the bidentate ligand. The Cl1-Au-Cl2 bond angle, which is not restricted, has adopted the ideal angle: 90°.

The pyrrolide-imine moiety, chloride ligands and gold(III) ion are all co-planar, the aromatic appendage is rotated relative to this plane with a torsion angle of 36(1)° relative to the pyrrole ring. This out-of-plane distortion is seemingly required to alleviate steric strain between the *ortho*-phenyl hydrogen atom and the imine hydrogen atom as well as relieves potential strain between the *ortho*-hydrogen atom and chloride ligand.

Weak C–H···Cl interactions link the molecules into an infinite one-dimensional network this is shown in Figure 4.4.4. There are weak Au···π interaction between the pyrrole ring and gold(III) ion of an adjacent molecule with a separation of 3.399(5) Å. There are also weak π···π interactions between the phenyl rings of two adjacent molecules. The 6-atom means planes of the phenyl rings are separated by 3.620(2) Å. This is longer than the interplanar spacing in graphite, which measures 3.35 Å and is therefore likely to be a relatively weak interaction.

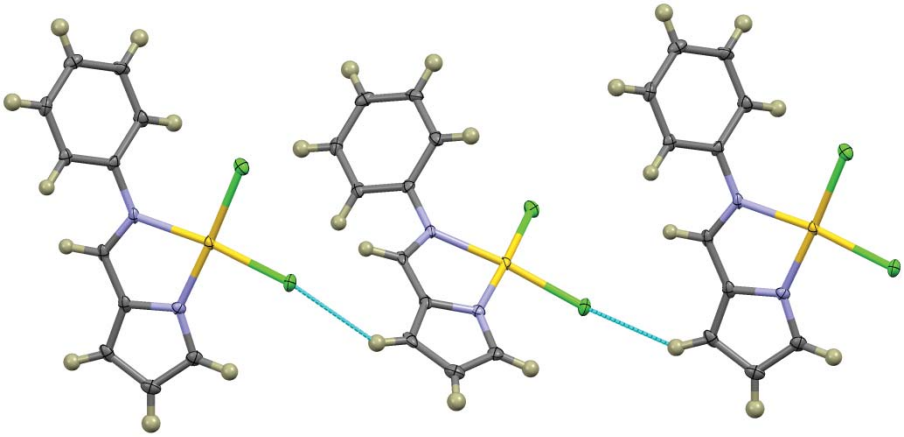

Figure 4.4.4: Non-classical C–H···Cl hydrogen bonding between the chloride ion and the β-pyrrole C–H.

4.4.3 X-Ray Structural Analysis of [Au(L3)Cl_2]

The gold(III) complex [Au(L3)Cl_2] crystallised in the monoclinic space group $P2_1/c$ with a single molecule in the asymmetric unit, $Z = 4$ (Figure 4.4.6).

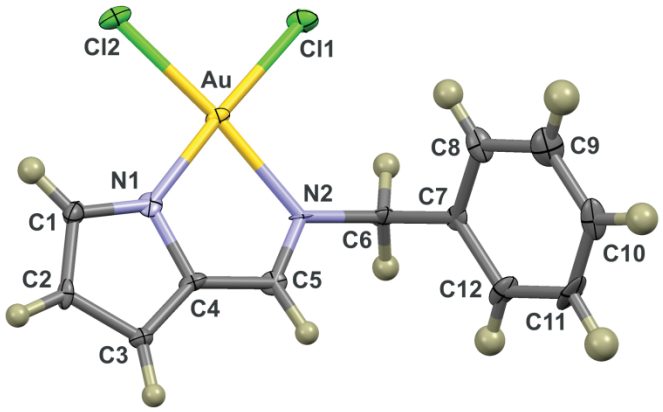

Figure 4.4.6: Labelled thermal ellipsoid plot of [Au(L3)Cl_2]. Non-hydrogen atoms have been drawn at the 50% probability level. Hydrogen atoms have been rendered as spheres of arbitrary radius.

Table 4.4.3 shows the Au–N1 and Au–N2 bond lengths measure 1.970(1) and 2.050(1) Å, respectively. The data in Table 4.4.3 compare favourably to the equivalent bond lengths of [Au(L1)Cl_2] and [Au(L2)Cl_2]. The coordination of gold(III) by the bidentate ligand yields a five-membered chelate ring, comprising the imine and pyrrole nitrogen atoms as well as the bridging carbon atoms C4 and C5 this is illustrated above in Figure 4.4.6. The phenyl ring

has adopted an orientation almost perpendicular to the planar coordination sphere. The angle subtended by the six-atom mean plane defined by the phenyl ring and the 11-atom mean plane defined by all remaining non-hydrogen atoms measures 71.6(3)°. This angle illustrates the near perpendicular orientation.

In the previously reported copper(II) chelate ERAHUA the Cu–N1 and Cu–N2 bond lengths measured 1.965(2) and 2.038(2) Å, respectively. These are very similar to the gold structure in this work even though it contains a different metal centre. In ERAHUA it is noted that the phenyl ring is similarly perpendicular to the planar aromatic region, with a torsion angle of 84.4(2)°. This is larger than that seen in this work, possibly due to the ligand being bis-chelated to the copper(II) ion, this results in increased steric strain between the phenyl rings and pyrrole moiety.

Table 4.4.3: Summary of the coordination sphere bond lengths and bond angles of [Au(L3)Cl_2].

Bond	Length (Å)	Bond	Angle (°)
Au–N1	1.970(1)	N1–Au–N2	81.5(5)
Au–N2	2.050(1)	Cl1–Au–Cl2	90.1(1)
Au–Cl1	2.292(4)	N1–Au–Cl2	92.9(4)
Au–Cl2	2.274(4)	N2–Au–Cl1	95.6(4)

The N1–Au–N2 bond angle is significantly more acute than the ideal bond angle for a square planar coordination geometry. This is attributed to the relatively small 5-atom chelation ring. An additional carbon atom spacer would allow for a more favourable bond angle. Similarly to [Au(L2)Cl_2], [Au(L3)Cl_2] has formed a one dimensional hydrogen-bonded network supported by weak C–H···Cl interactions between the chloride ligands and the β-pyrrole hydrogen atom. This is illustrated in Figure 4.4.7.

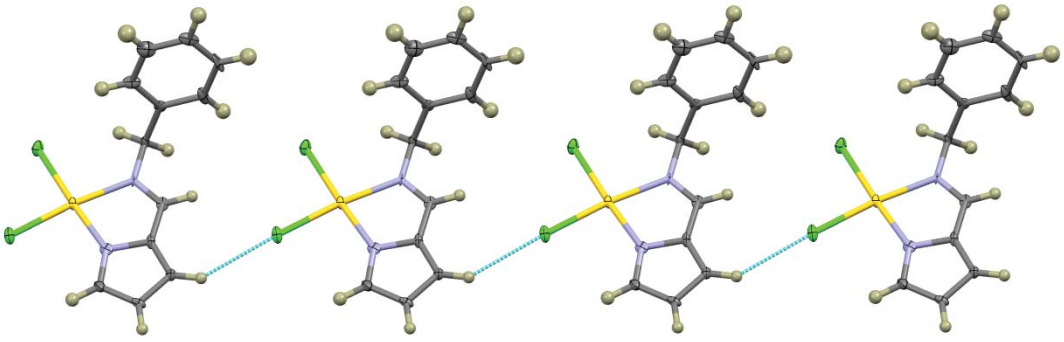

Figure 4.4.7: Non-classical hydrogen bonding between the chloride ligand and the β-pyrrole C–H of an adjacent molecule. This interaction leads to an infinite, one-dimensional network parallel to the b-axis.

4.4.4 X-ray Structure Analysis of [Au(L4)Cl_2]

The gold(III) chelate, [Au(L4)Cl_2], crystallised in the monoclinic space group $P2_1/n$, with a single molecule in the asymmetric unit, $Z = 4$ (Figure 4.4.8). Table 4.4.5 summarises the key bond lengths and bond angles which describe the square planar coordination sphere of the gold(III) ion.

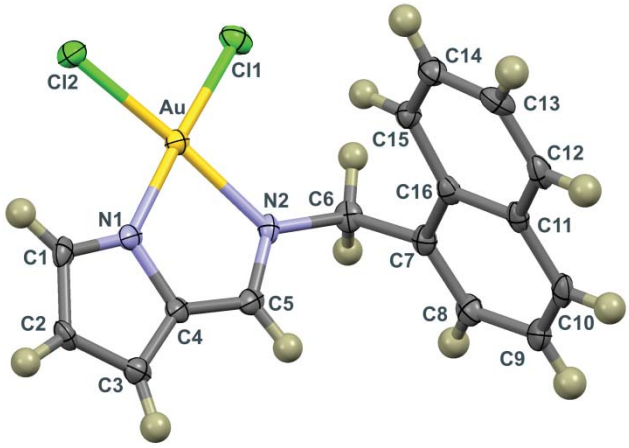

Figure 4.4.8: Labelled thermal ellipsoid plot of the complex [Au(L4)Cl_2]. Non-hydrogen atoms are shown at the 50% probability level. Hydrogen atoms have been rendered as spheres of arbitrary radius.

Table 4.4.4: Summary of the bond lengths and bond angles of [Au(L4)Cl_2].

Bond	Length (Å)	Bond	Angle (°)
Au–N1	1.985(4)	N1–Au–N2	80.8(1)
Au–N2	2.045(3)	Cl1–Au–Cl2	90.44(4)
Au–Cl1	2.276(1)	N1–Au–Cl2	95.6(1)
Au–Cl2	2.270(1)	N2–Au–Cl1	93.3(1)

The bond parameters which describe the coordination sphere of the gold(III) ion of [Au(L4)Cl_2] are in good agreement with those of the gold(III) chelates reported in this work and structurally related gold(III) chelates that have been previously reported.[19] The $Au–N_{pyridine}$ and $Au–N_{imine}$ bond lengths for the previously reported gold(III) chelate CESMUJ are approximately equal, measuring 2.024(7) and 2.046(7) Å, respectively. The $Au–N_{imine}$ bond lengths reported in this work compare favourably with these data. Similarly, the Au–Cl bond lengths which average 2.265(2) Å in CESMUJ are statistically comparable (within three standard deviations) to those reported in this work. The only notable difference is that the $Au–N_{pyrrole}$ bond lengths reported herein are substantially shorter. This reflects the stronger bonding of the metal ion to this strong σ-donor atom.

As with the previous structures, $[Au(L4)Cl_2]$ exhibits Au···π interactions between the gold(III) ion and the pyrrole ring (Figure 4.4.9). The distance between the centroid of the pyrrole ring and the gold(III) ion measures 3.372(2) Å. As in the case of $[Au(L2)Cl_2]$ and $[Au(L3)Cl_2]$, the aromatic appendage of $[Au(L4)Cl_2]$ has adopted an orientation nearly perpendicular to the coordination sphere. This near perpendicular orientation is illustrated by the N1–C4–C7–C8 torsion angle which measures 62.6(4)°. This perpendicular orientation relieves any potential steric interaction between the naphthyl ring and the chloride ligands.

The structure exhibits a number of weak intermolecular interactions. Adjacent molecules are linked into dimeric structures through both Au···π and π···π interactions (Figure 4.4.9). There are π···π interactions between the naphthyl rings of adjacent molecules with a separation of 3.45(2) Å between the 10-atom mean planes of two adjacent molecules. This interplanar spacing is comparable to that of graphite (3.35 Å) and suggests that it is a reasonably significant interaction.

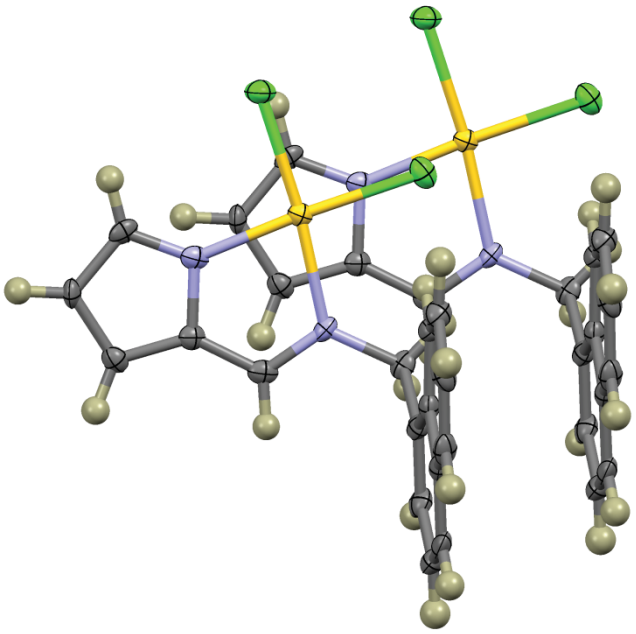

Figure 4.4.9: X-ray crystal structure of $[Au(L4)Cl_2]$ showing Au···π interactions between the pyrrole rings and gold(III) ion of two adjacent chelates as well as the π···π interactions between adjacent naphthyl rings.

Figure 4.4.10 shows the non-classical hydrogen bonds between the β-pyrrole hydrogen and the chloride ligand. These link the molecules into an infinite one-dimensional chain. The D–H, H···A and D···A distances measure 0.949(4), 2.684(1) and 3.611(4) Å, respectively. The D–H···A angle measures 165.4(3) °.

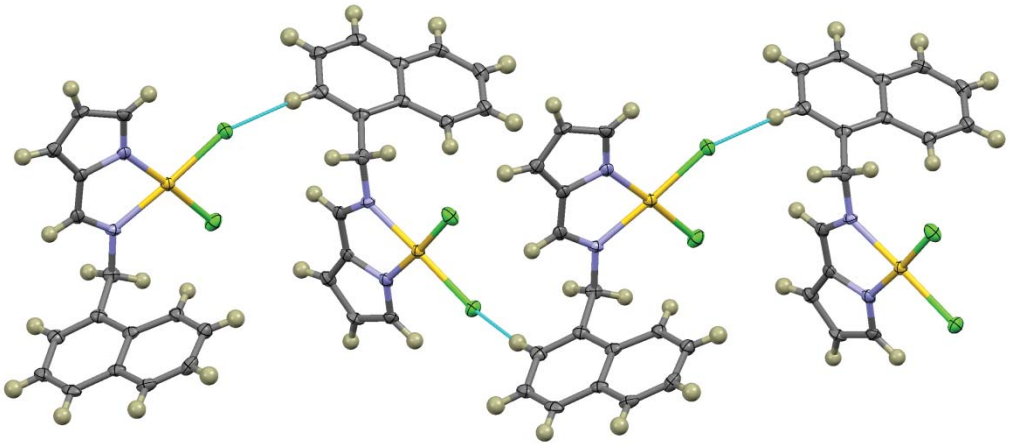

Figure 4.4.10: One-dimensional hydrogen bonded chain of [Au(L4)Cl_2] supported by hydrogen bonds between the β-pyrrole H and chloride ligand viewed down the a-axis. The chain is co-linear with the b-axis.

4.4.5 X-ray Structural Analysis of [Au(L5)Cl_2]

The gold(III) chelate [Au(L5)Cl_2] crystallised in the monoclinic space group $P2_1/n$. with a single molecule in the asymmetric unit, $Z = 4$ (Figure 4.4.11). The chelate comprises a pyrrole-imine moiety linked to a phenyl ring through an two methylene spacer. The X-ray structure shows that the phenyl ring lies co-planar with respect to the five-membered pyrrole ring.

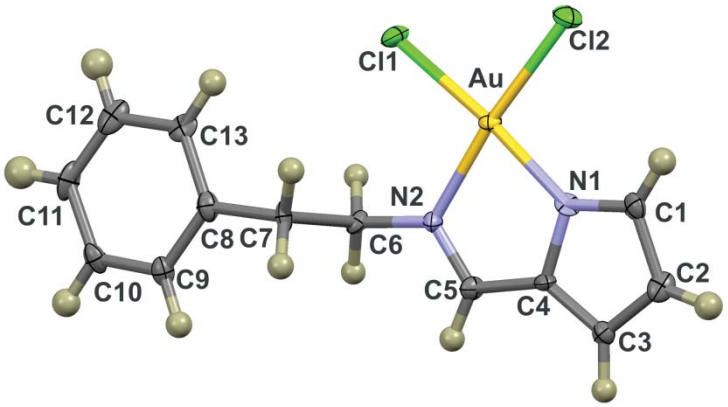

Figure 4.4.11: Labelled thermal ellipsoid plot of the complex [Au(L5)Cl_2]. Non-hydrogen atoms have been drawn at the 50% probability level. Hydrogen atoms have been rendered as spheres of arbitrary radius.

The chelates $[Au(L3)Cl_2]$ and $[Au(L4)Cl_2]$ both comprise a pyrrole-imine moiety linked to an aromatic appendage (phenyl and napthyl, respectively) through a single methylene spacer and in both cases the aromatic appendages are orientated perpendicular to the coordination sphere. $[Au(L5)Cl_2]$ has two methylene spacer between the imine group and the aromatic appendage, the additional degrees of freedom this affords results in a phenyl ring which is co-planar with the coordination sphere. A similar pattern is observed in the free ligand structures.

Table 4.4.5 shows the Au–N1 and Au–N2 bond lengths measure 1.980(1) and 2.040(1) Å, respectively. The data in Table 4.4.5 compare favourably to the equivalent bond lengths of $[Au(L3)Cl_2]$ and $[Au(L4)Cl_2]$. The coordination of gold(III) by the bidentate ligand yields a five membered chelate ring, comprising the imine and pyrrole nitrogen atoms as well as the bridging carbon atoms C4 and C5, this is shown above in Figure 4.4.11.

Table 4.4.5: Summary of the bond lengths and bond angles of $[Au(L5)Cl_2]$.

Bond	**Length (Å)**	**Bond**	**Angle (°)**
Au–N1	1.980(1)	N1–Au–N2	80.4(6)
Au–N2	2.040(1)	Cl1–Au–Cl2	91.3(1)
Au–Cl1	2.275(4)	N1–Au–Cl2	93.4(4)
Au–Cl2	2.281(4)	N2–Au–Cl1	94.4(4)

In the spacefilling model of $[Au(L5)Cl_2]$, Figure 4.4.12, it is shown that the methylene groups allow for free roatation and the extended length allows for the orientation of the aromatic region to be co-planar with a torsion ange of 177.06(2)° with respect to the pyrrole ring.

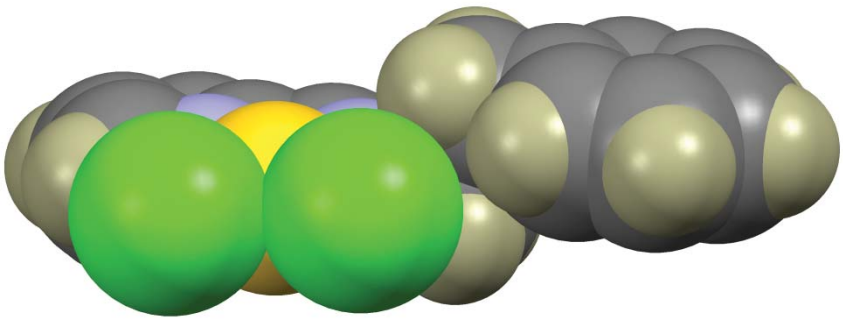

Figure 4.4.12: Spacefilling diagram of $[Au(L5)Cl_2]$ showing the co-planar, stepped configuration of the phenyl ring and pyrrole-imine moiety.

4.5 Conclusion

The structures of four free ligands and five gold(III) chelates were studied by single crystal X-ray diffraction. The aromatic appendages of ligands HL3 and HL4 were found to be in a perpendicular orientation relative to the pyrrole-imine moiety. The additional degrees of freedom afforded by the ethyl linkage unit of HL5 allowed the phenyl ring to adopt an orientation co-planar with the pyrrole-imine unit. Owing to the extended aromaticity of HL2 it would be expected that the structure would be planar. However, to alleviate non-bonded repulsion between the *o*-phenyl and imine hydrogen atoms an out-of-plane rotation is required. All the free ligands exhibited complementary hydrogen bonding between the pyrrole NH and the imine nitrogen atom of an adjacent molecule. The D···A hydrogen bond lengths range from 2.984(1) to 3.073(1) Å (average = 3.012(1) Å). The D–H···A bond angles range from 147.88(6) to 158.09(1)° (average = 154.41(6)°).

The gold(III) ion exhibits a nominally square planar coordination geometry in all cases, consistent with the d^8 electronic configuration. Metal chelation occurred with concomitant deprotonation of the pyrrole NH yielding a monoanionic, bidentate N_2-donor ligand. The remaining coordination sites were occupied by two chloride ligands in a *cis*-configuration. The The Au–N_{imine} bond length (average = 2.037(3) Å) which is considerably longer than the Au–$N_{pyrrole}$ bond length (average = 1.983(3) Å). This is attributed to the partial negative charge on the deprotonated pyrrole nitrogen atom, making it a stronger σ-donor. The N1–Au–N2 *ca*. 82°, which is more acute than the ideal bond angle for a square planar geometry. This is attributed to the relatively small bite angle of the ligand.

4.6 Summary of X-ray Data

4.6.1 Summary of X-ray Data for the Pyrrolide-Imine Ligands

Table 4.6.1: Crystal data and structure refinement details for HL2, HL3, HL4 and HL5.

Crystal Data	**HL2**	**HL3**	**HL4**	**HL5**
Chemical formula	$C_{11}H_{10}N_2$	$C_{12}H_{12}N_2$	$C_{16}H_{14}N_2$	$C_{13}H_{14}N_2$
Molar Mass(g. mol^{-1})	170.21	184.24	234.29	198.26
Crystal system, space group	Orthorhombic, *Pbca*	Monoclinic, $P2_1/n$	Triclinic, *P*-1	Monoclinic, $P2_1/c$
Temperature(K)	100(2)	100(2)	100(2)	100(2)
a, b, c (Å)	9.4092(8), 18.1595(16), 21.2310(18)	9.8555(5), 17.3532(9), 11.7790(6)	5.3017(3), 8.8579(5), 13.9265(8)	7.0928(5), 16.0355(12), 9.2398(7)
α , β, γ (°)	α = γ = β = 90.00	α = γ = 90, β = 94.184(2)	α= 104.896 (3) γ= 96.675 (2) , β = 99.212 (2)	α= γ = 90, β = 96.261(3)
V($Å^3$)	3627.7(5)	2009.13(18)	615.33(6)	1044.64(13)
Z	16	8	2	4
Radiation type	Mo Kα	Mo Kα	Mo Kα	Mo Kα
μ(mm^{-1})	0.08	0.07	0.08	0.08
Crystal size (mm)	0.25 × 0.37 ×0.42	0.60 × 0.45 × 0.30	0.40 × 0.35 × 0.30	0.35 × 0.20 × 0.03
Data collection				
Diffractometer	Bruker APEXII CCD diffractometer			
Absorption Correction	Multi-scan*SADABS*, Bruker 2012			
T_{min}, T_{max}	0.962, 0.991	0.957, 0.978	0.971, 0.978	0.974, 0.998
No. of measured, independent and observed [I>2σ(I)] reflections	14939, 3555, 3121	31276, 4118, 3683	9165, 2397, 2260	10061, 2080, 1836
R_{int}	0.026	0.026	0.022	0.023
Refinement				
$R[F^2> 2\sigma(F^2)]$, $wR(F^2)$, *S*	0.037, 0.147, 1.21	0.037, 0.104, 1.04	0.039, 0.117, 1.03	0.038, 0.104, 1.07
No. of reflections	3555	4118	2397	2080
No. of parameters	235	253	163	136
No. of restraints	0	0	0	0
H-atom treatment	H atoms treated by a mixture of independent and constrained refinement			
$\Delta\rho_{max}.\Delta\rho_{min}$ (e $Å^{-3}$)	0.18, −0.27	0.23, −0.27	0.22, −0.31	0.24, −0.26

4.6.2 Summary Of X-Ray Data for Pyrrolide-Imine Gold(III) Chelates

Table 4.5.2: Crystal data and structure refinement details for the gold(III) chelates [Au(L1-5)Cl_2].

Crystal Data	**[Au(L1)Cl_2]**	**[Au(L2)Cl_2]**	**[Au(L3)Cl_2]**	**[Au(L4)Cl_2]**	**[Au(L5)Cl_2]**
Chemical formula	$C_8H_{11}AuCl_2N_2$	$C_{11}H_9AuCl_2N_2$	$C_{12}H_{11}AuCl_2N_2$	$C_{16}H_{13}AuCl_2N_2$	$C_{13}H_{13}AuCl_2N_2$
M_r (g mol^{-1})	403,06	437.07	451.09	501.15	465.12
Cryst. Syst. space group	Orthorhombic, *Pca2₁*	Monoclinic, *P2₁/c*	Monoclinic, $P2_1$	Monoclinic, *P2₁/n*	Monoclinic, *P2₁/n*
Temp (K)	100(2)	100(2)	100(2)	100(2)	100(2)
a,b,c (Å)	19.1684(9), 7.3679(4), 7.2571(3)	18.4739(10), 4.1151(2), 15.1775(8)	7.096(5), 4.557(4), 19.792(5)	4.8648(3), 13.9634(8), 21.7386(13)	19.0672(14), 7.2240(4), 20.2020(14)
α , β, γ (°)	α = γ = β =90.00	α = γ = 90, β =99.534(2)	α = γ = 90, β =99.298(5)	α = γ = 90.00 β = 90.060(1)	α = γ = 90, β = 92.602(3)
V($Å^3$)	1048.99(9)	1137.89(10)	631.6(8)	1476.68(15)	2779.8(3)
Z	4	4	2	4	4
Radiation	Mo Kα	Mo Kα	Mo Kα	Mo Kα	Mo Kα
M (mm^{-1})	14.49	13.37	12.05	10.32	10.95
Size (mm)	0.55 × 0.20 × 0.03	0.60 × 0.08 × 0.04	0.15 × 0.02 × 0.02	0.45 × 0.12 × 0.07	0.60 × 0.21 × 0.15
Data collection					
Diffractom.	Bruker APEXII CCD diffractometer				
Abs. Corr.	Multi-scan*SADABS*, Bruker 2012				
T_{min}, T_{max}	0.046, 0.670	0.046, 0.617	0.265, 0.795	0.090, 0.532	0.059, 0.290
No. of meas., ind. and obs. [I > 2σ (I)] reflections	15023, 2051, 1968	8873, 2214, 2086	5254, 1457, 1402	11020, 2100, 1880	27749, 6772, 6109
R_{int}	0.032	0.023	0.034	0.031	0.041
Refinement					
$R[F^2> 2\sigma(F^2)]$, $wR(F^2)$, *S*	0.021, 0.057, 0.75	0.017, 0.041, 1.05	0.036, 0.084, 1.23	0.019, 0.046, 1.04	0.069, 0.204, 1.19
No. reflect.	2051	2214	1457	2100	6772
No. of par.	119	145	154	190	325
No. of restraints	7	0	13	0	6
H-atom	H atoms treated by constrained refinement				
$\Delta\rho_{max}.\Delta\rho_{min}$ (e $Å^{-3}$)	1.04, −1.06	1.19, −1.20	3.26, −3.71	0.79, −0.57	6.95, −3.72

Chapter Five: Spectroscopy

5.1 Infrared Spectroscopy

Four of the free ligands and all the gold(III) chelates have been studied by infrared spectroscopy. Infrared spectra were recorded using a Bruker Alpha FTIR spectrometer equipped with an ATR platinum Diamond 1 reflectance accessory. The machine acquired the information in 32 scans with a spectral resolution of 1.0 cm^{-1}.

Infrared spectroscopy is based on the fact that covalent bonds absorb different frequencies in the infrared region. The crucial region is 4000 to 400 cm^{-1}, which is the vibrational region. The total energy of a molecule is the sum of three variables 1) the rotation of the molecule, 2) the vibrations of each atom in the molecule, and 3) the movement of the electrons in the molecule. This is shown in the equation below.

$$E_{total} = E_{el} + E_{vib} + E_{rot} \qquad 5.1.1...$$

Each functional group of a molecule absorbs a specific frequency of IR radiation. This results in a unique spectrum in which individual functional groups can be recognized.

5.1.1 Results and Discussion: Infrared Spectroscopy

The most noticeable absorption band for the pyrrolide-imine ligands in this work is the imine (C=N) stretching vibration, this vibration occurs in the region of 1610-1640 cm^{-1}. This bond also shows the greatest spectral shift when the free ligand is coordinated to the gold(III) ion.[18] The vibrational frequencies for both the free ligands and the gold(III) chelates are shown in Table 5.1.1.

Table 5.1.1: Imine stretching vibrations of the pyrrolide-imine ligands and gold(III) chelates.

Pyrrolide-imine ligand	**Free ligand (cm^{-1})**	**Gold(III) chelate (cm^{-1})**
HL1	1581.70	1576.10
HL2	1617.19	1566.77
HL3	1632.18	1577.01
HL4	1643.69	1568.37
HL5	1642.87	1574.45

The frequencies shown in the above table for υ(C=N) stretching vibrations of the gold(III) chelates shift to lower energy and therefore have lower wavenumbers than the free ligands.[59] Although there is an overall trend that there is a decrease in the wavenumbers upon chelation to gold(III), it is noted that the ligands with the lower stretching frequency do not necessarily have the lower stretching frequency when chelated to the gold(III) ion. This is due to the gold(III) ion removing electron density from the ligand, resulting in a lower imine stretching.[59]

A noticeable point is that the ligand which has no alkyl spacer between the imine bond and aromatic appendage has the lowest υ(C=N) stretching frequency. This is due to extended aromaticity which removes electron density from the C=N bond resulting in a weaker imine bond, which therefore results in a lower stretching frequency. The ligands with methylene spacer groups break the aromaticity and thus no electron density is removed from the imine bond and a higher stretching frequency is observed.

One of the most notable points in the IR spectra is the disappearance of the pyrrole NH stretching frequency upon metal chelation. The frequencies of the pyrrole NH stretching vibrations are shown in Table 5.1.2.

Table 5.1.2: Pyrrole NH stretching frequencies for the pyrrolide-imine ligands.

Pyrrolide-Imine ligand	**δ(NH, pyrrole) /cm^{-1}**
HL2	3213.20
HL3	3142.25
HL4	3170.73
HL5	3162.43

A comparison of the data in Table 5.1.2 with previously reported stretching frequencies shows that the frequencies of the pyrrole NH stretches are lower than that of previously reported secondary amines, which have frequencies in the range of (3300-3500),[18, 51, 57, 66] This is attributed to the hydrogen bonding in the solid state between the pyrrole NH and imine nitrogen atom of an adjacent molecule. This intermolecular interaction results in a lower force constant of the pyrrole N-H bond and in turn lowers the frequency of the absorption band.[67]

Figure 5.1.1 and 5.1.2 show the IR spectra of a representative free ligand and gold(III) chelate, HL3 and [Au(L3)Cl_2]. These figures illustrate some of the key differences in the free ligand and metal chelate spectra.

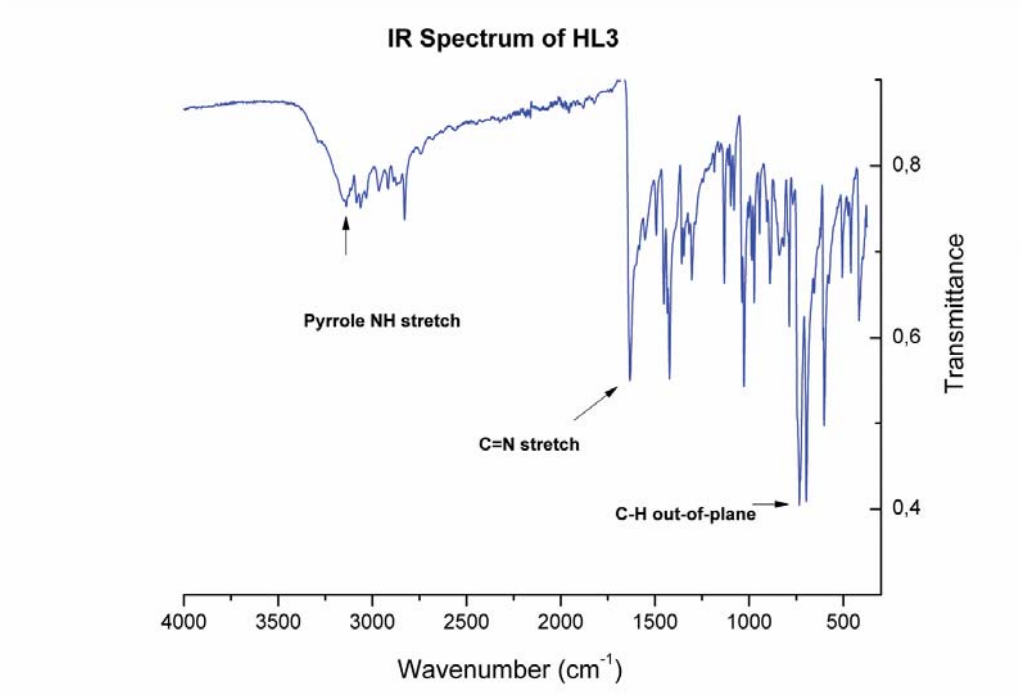

Figure 5.1.1: IR spectrum of HL3.

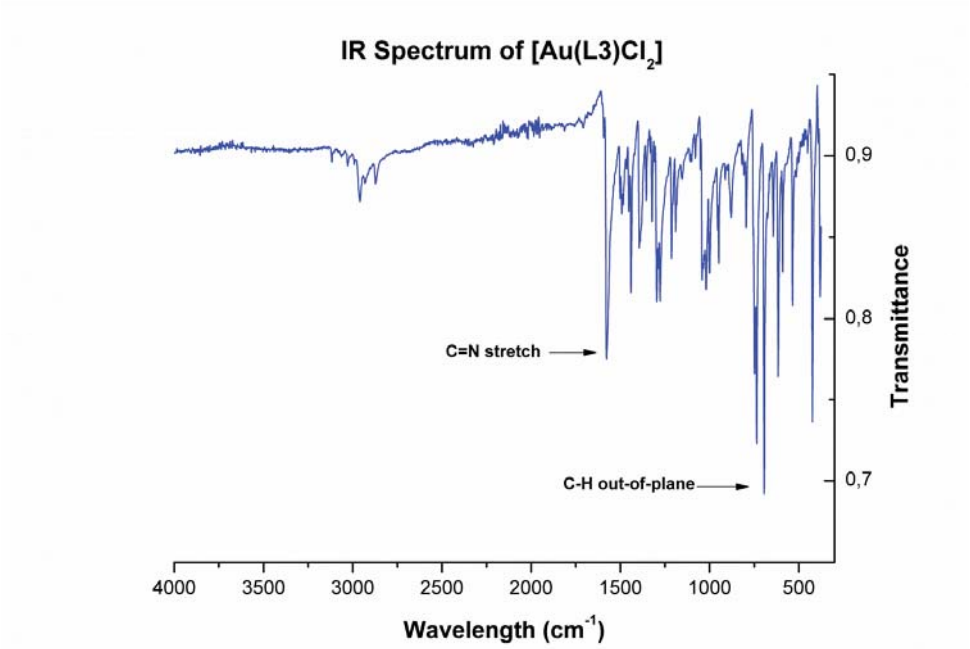

Figure 5.1.2: IR spectrum of the gold(III) complex $[Au(L3)Cl_2]$.

A comparison of Figure 5.1.1 and 5.1.2 and their associated stretching frequencies show a few noteworthy characteristics. Firstly, the lack of a peak in the region 3250-3500 cm^{-1} for the gold(III) chelate, but the presence of a peak in this region in the free ligand.[66] This peak corresponds to the pyrrole N-H stretching vibration. This indicates that chelation of the metal ion has occurred with concomitant deprotonation of the pyrrole ring. Secondly, it is noted that there is a shift towards a lower frequency for the C=N stretch upon chelation. This occurs because of the electron deficient nature of the gold(III) ion, which results in a weakening of the imine bond as the gold ion removes electron density from the ligand. This is consistent with previously reported Schiff base metal chelates.

5.2 UV/visible Spectroscopy

In a UV/visible spectrophotometer, light from a constant source is passed through a monochromator to select a single wavelength.[67] The wavelength has a specific Intensity, $I_{0,}$ which strikes the sample in the cell of length, l. The beam then exits the sample with an intensity, I ($I<I_0$). A spectrometer is capable of measuring the transmittance, T, which is defined as the fraction of the original light passing through the sample. However, the absorbance is more useful and it can be calculated from the transmittance (Equation 5.2.1).

$$A = log\left(\frac{I_0}{I}\right) = -logT \qquad 5.2.1$$

According to Beer's law (Equation 5.2.2), absorbance is directly proportional to the concentration of the sample.

$$A = \varepsilon \text{ x } c \text{ x } l \qquad 5.2.2$$

In equation 5.2.2, A is the absorbance (dimensionless), ε is the extinction coefficient (mol^{-1} dm^3 cm^{-1}), c is the concentration of the sample (M) and l is the path length (cm).

When a continuous light source is passed through a transparent medium, a selection of light may be absorbed. This absorption results in gaps in the intensity at different wavelengths this in turn results in an absorption spectrum. Due to this continuous radiation and the absorption of energy by atoms or molecules, it causes these atoms or molecules to move from a lower state of energy to an excited state. With regard to the ultraviolet and visible portion of the electromagnetic spectrum the energy transitions link to the transitions between the highest occupied molecular orbital (HOMO) and lowest unoccupied molecular orbital (LUMO).[67] There are different transitions of electrons that can occur between numerous orbitals, the most relevant transitions are those from the lowest energy state as shown in Figure 5.2.1.

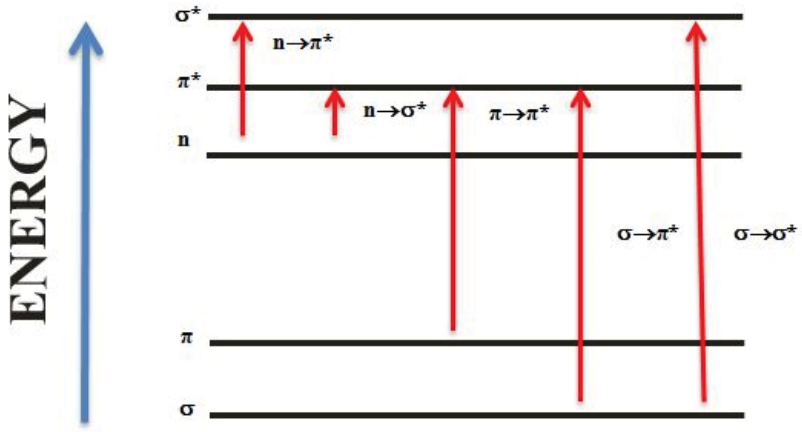

Figure 5.2.1: Electronic energy levels and possible transitions.[68]

Not all the transitions shown in Figure 5.2.1 are observed. Some are forbidden transitions, this is due to the transition requiring a change in the spin quantum number of the electron during the transition which is not allowed.[67]

The electronic spectrum for the pyrrolide-imine ligands should all be similar as they are dominated by the aromatic pyrrole-imine moiety, the alkyl spacers having minimal effect on the absorption bands in the ligand spectra. The main absorption bands will be due to strong intraligand π→π* transitions. These result from the absorption of the conjuncted π system of the imine bond and pyrrole ring. These π→π* transitions should be found in the region between 270 to 320 nm.[67] For the ligands chelated to gold(III) there is expected to be an additional absorption band which will be apparent in the region of 300-400 nm.[61] This region corresponds to the ligand-to-metal charge transfer (LMCT) bands.

5.2.1 Results and Discussion

The electronic spectra of HL3 and [Au(L3)Cl_2] are given as representative examples in Figures 5.2.2 and 5.2.3. The UV-visible spectrum of HL3 shows the intraligand π→π* transition at 281 nm. This is characteristic of the free and chelated pyrrolide-imine ligands.

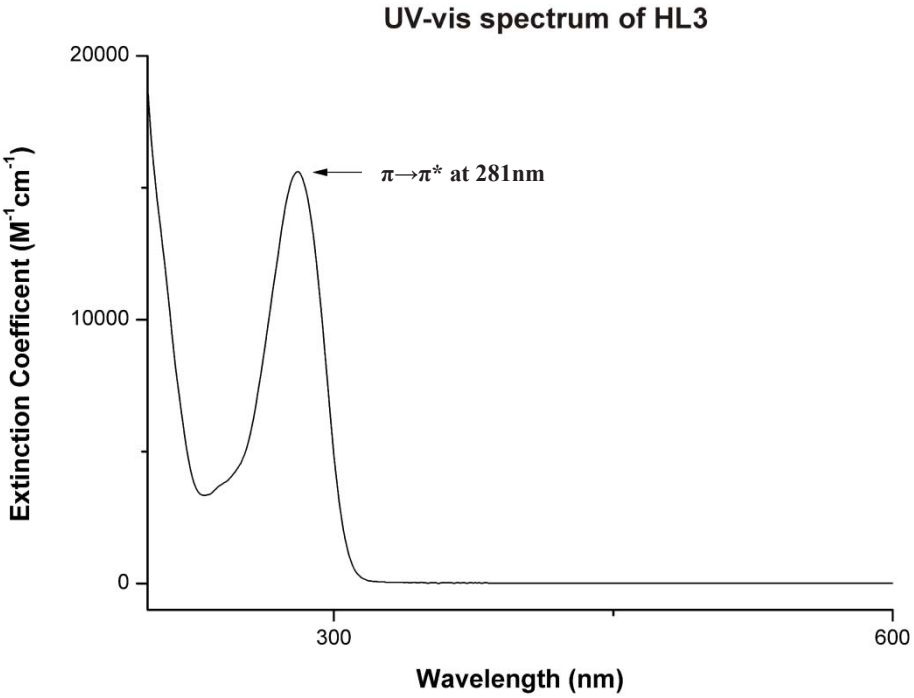

Figure 5.2.2: Electronic spectrum of HL3 at 298 K in acetonitrile showing the π→π* band (281 nm).

The wavelength at which the maximum absorbance occurs (λ_{max}) and the extinction coefficients of the absorption bands for the pyrrolide-imine ligands reported in this work are summarised in Table 5.2.1.

Table 5.2.1: Summary of λ_{max} and molar absorbance values for the absorption bands of the pyrrolide-imine ligands in this work.

Compound	λ_{max}/nm (ε / $M^{-1}cm^{-1}$)
HL1	277(2.14×10^4)
HL2	322 (2.11×10^4)
HL3	281 (1.50×10^4)
HL4	223 (5.36×10^4), 283 (2.03×10^4)
HL5	279 (1.80×10^4)

The data in Table 5.2.1 illustrate a few key points. The spectra of HL1, HL3 and HL5 are all very similar, suggesting that the absorption spectra are dominated by the pyrrole-imine moiety. The π-π* band of HL2, which has extended aromaticity, shows a bathochromic shift. Finally, the fused aromatic rings of the napthyl group of HL4 lead to an additional π-π* transition at higher energy.

Figure 5.2.3, shows that the electronic spectrum of [Au(L3)Cl_2] has two peaks, one corresponds to the intraligand π→π* transition at a wavelength of 297 nm. Comparing this to the wavelength of the free ligand it is noted that gold(III) chelation has resulted in a slight bathochromic shift. The metallation of the ligand has also resulted in a new absorption peak at 368 nm. This absorption band is mainly due to a π→σ* transition, that occurs because of the transfer of electrons between the ligand and square planar gold(III) cation commonly known as a ligand-to-metal charge transfer (LMCT) band. The spectral assignment of the electronic spectrum was based on DFT calculations (refer to Chapter 6). The high oxidation state of the gold(III) ion means that the more common metal-to-ligand charge transfer (MLCT) bands are not possible. The spectrum shows that the intensity of the band agrees with this assignment, it also shows that there is potentially mixing of the ligand π-orbitals and the metal d-orbitals, this results in an increased intensity of the absorption band.[61]

Comparing the free ligand and gold(III) chelate spectra it is noted that the energy of the π→π*transition at 281 nm for HL3 is higher than [Au(L3)Cl_2] (at 297 nm), this is consistent with the coordination of HL3 to a metal ion and is observed in all the UV-visible spectra for the free ligands and gold(III) chelates. This trend has also been shown in previous studies that involve strong intraligand charge-transfer transitions.[68]

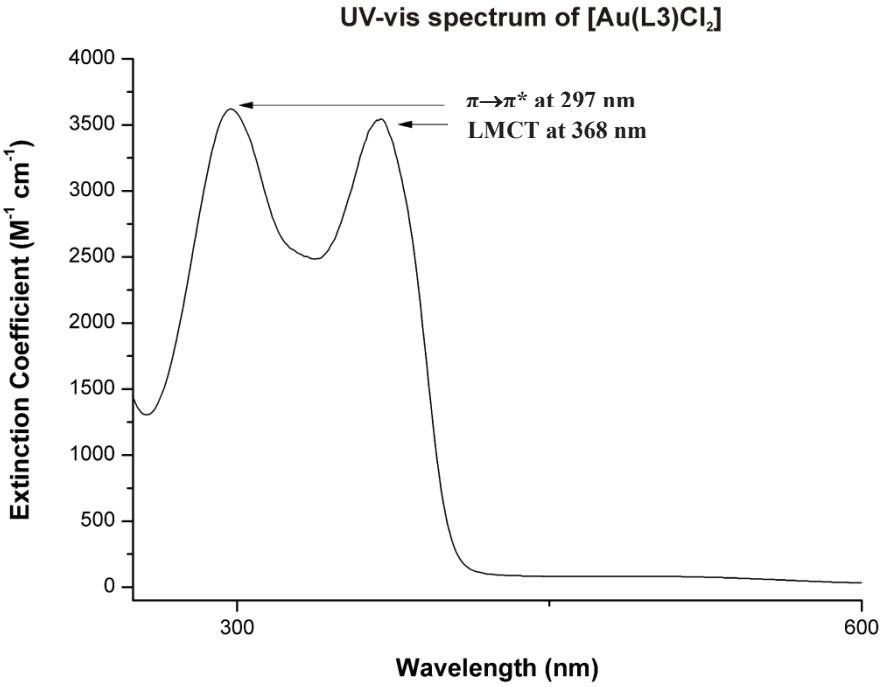

Figure 5.2.3: Electronic spectrum of $[Au(L3)Cl_2]$ at 298K in acetonitrile showing the $\pi \rightarrow \pi^*$ band (297 nm) and LMCT band (368 nm).

The wavelengths and extinction coefficients of the π-π^* and LMCT bands for the gold(III) chelates are reported in Table 5.2.2.

Table 5.2.2: Summary of λ_{max} values and extinction coefficients of the gold(III) complexes.

Compound	λ_{max} / nm (ε / $M^{-1}cm^{-1}$)	λ_{max} / nm (ε / $M^{-1}cm^{-1}$)
$[Au(L1)Cl_2]$	294 ($2.40x10^3$)	364 ($2.93x10^3$)
$[Au(L2)Cl_2]$	224 ($2.55x10^4$)	316 ($7.18x10^3$)
$[Au(L3)Cl_2]$	297 ($8.48x10^3$)	368 ($8.31x10^3$)
$[Au(L4)Cl_2]$	290 ($1.31x10^4$)	363 ($1.03x10^4$)
$[Au(L5)Cl_2]$	292 ($7.48x10^3$)	366 ($6.83x10^3$)

Table 5.2.2 shows that there is very little difference shown between the λ_{max} values of the gold(III) chelates. $[Au(L1)Cl_2]$, $[Au(L3)Cl_2]$, $[Au(L4)Cl_2]$ and $[Au(L5)Cl_2]$ have approximately the same λ_{max}. This is expected as the addition of a methylene spacer group will have little effect on the absorbance of the complex. The exception is $[Au(L2)Cl_2]$, which absorbs at a lower wavelength compared to the other gold(III) chelates this is likely due to the extended aromaticity of the ligand.

5.3 NMR Spectroscopy

NMR spectroscopy is based on the principle that nuclei exhibit magnetic properties such as nuclear spin (I) and magnetic moment (μ). Magnetic resonance is only observed when a nucleus with $I \neq 0$ is placed in a magnetic field (B_0).[69-70] When radio frequency energy (rf) is applied as a pulse to the nucleus in NMR spectroscopy, this results in a transition between different energy states.[70] The excited nucleus emits radiation as it is a time dependent decay, this emitted radiation is obtained and Fourier transformed into a frequency-domain spectrum. Different functional groups give rise to peaks at different chemical shifts due to being located in different molecular environments. The intensities of the peaks can be directly related to the number of nuclei responsible.[69-70]

The ligands and complexes reported here have been studied by ^{1}H, ^{13}C, cosy, hmbc, hsqc and dept NMR experiments. The ^{1}H and ^{13}C NMR spectra for the pyrrolide-imine ligand and gold(III) chelates are expected to be similar. The main difference will be the lack of the pyrrole N-H signal in the ^{1}H NMR spectra for the gold(III) chelates. There is also expected to be a downfield shift of all the other signals, this is due to the deshielding that the carbon and hydrogen nuclei experience with gold(III) ion chelation. The gold(III) ion acts as an electron withdrawer, therefore there will be less valence electron density around the pyrrole α-C and α-H. This reduced valence electron density results in less shielding of the carbon and hydrogen nuclei from the applied magnetic field. This deshielding results in a downfield shift in the proton and carbon signals. This shift should be most evident in the atoms closest to the gold(III) ion.

5.3.1 Results and Discussion of NMR spectroscopy

A summary of the chemical shifts for the ^{1}H NMR spectra for both HL3 and $[Au(L3)Cl_2]$ are shown in Table 5.3.1. The data in Table 5.3.1 and 5.3.2 shown that there was the expected shift downfield in both the ^{1}H and ^{13}C NMR spectra.

Table 5.3.1: Summary of the ^{1}H NMR chemical shifts for the pyrrolide-imine ligand HL3 and gold(III) chelate $[Au(L3)Cl_2]$.

Proton	HL3 (ppm)	$[Au(L3)Cl_2]$ (ppm)
Pyrrole δ-H	6.89	7.31
Pyrrole γ-H	6.12	6.43
Pyrrole β-H	6.49	7.08
Imine	8.20	8.37
CH_2	4.67	5.04
Phenyl ring	7.19-7.35	7.35-7.40

Figure 5.3.1 below shows the fully assigned ^{1}H NMR spectrum of HL3. This is shown as a representative example for all the free ligands.

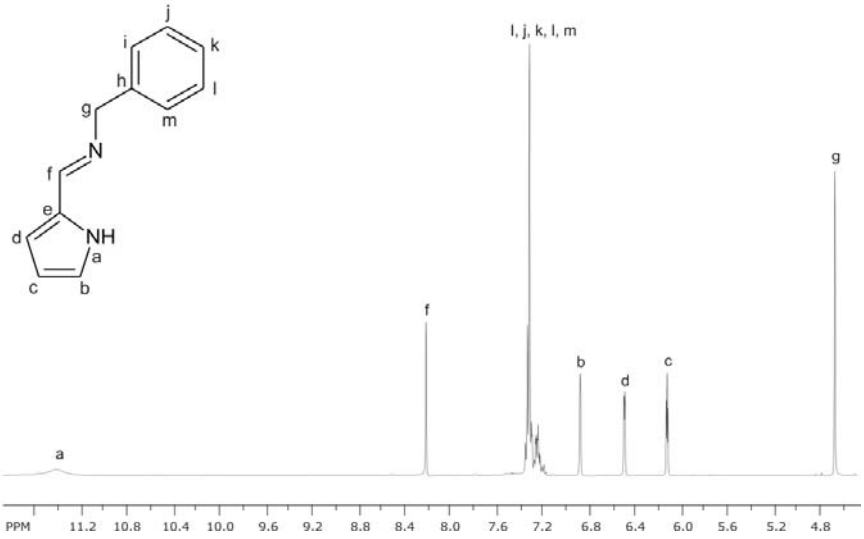

Figure 5.3.1: ^{1}H NMR spectrum of HL3 in DMSO at 298 K showing the spectral assignments.

Comparing the chemical shifts of the ^{1}H NMR signals for HL3 and $[Au(L3)Cl_2]$ shows an overall downfield shift for all the signals in the gold(III) spectrum relative to the free ligand. The δ-H exhibits the greatest shift downfield, because of its close proximity to the gold(III) ion. Correspondingly, the β-H experiences less deshielding and therefore exhibits a smaller downfield shift as it is located further from the gold(III) ion. The spectral assignments for the pyrrolide-imine ligands and gold(III) chelates are available in Chapter 2. A comparison with previous studies shows that the imine hydrogen atom is in the expected region of the spectrum with a chemical shift of approximately 8.40 ppm.[52, 68]

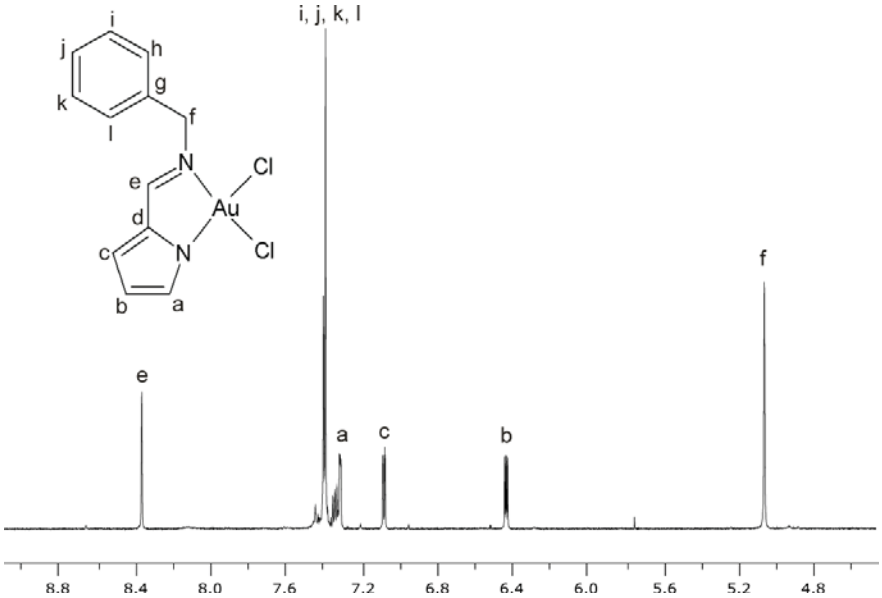

Figure 5.3.2: ^{1}H NMR spectrum of $[Au(L3)Cl_2]$ in DMSO at 298 K showing the spectral assignments.

Table 5.3.2 summaries the ^{13}C NMR chemical shifts of HL3 and $[Au(L3)Cl_2]$.

Table 5.3.2: Summary of the ^{13}C NMR chemical shifts for the pyrrolide-imine ligand HL3 and gold(III) chelate $[Au(L3)Cl_2]$.

Carbon	HL3 (ppm)	$[Au(L3)Cl_2]$(ppm)
Pyrrole δ-C	122.64	129.30
Pyrrole γ-C	109.38	111.52
Pyrrole β-C	114.24	123.19
Pyrrole α-C	130.48	137.16
Imine	153.05	165.8
CH_2	64.41	60.48
α-Phenyl	140.59	129.19
β-phenyl	128.51	136.49
γ-phenyl	128.71	128.31
δ-phenyl	127.47	135.86
ε-phenyl	128.71	129.30
ζ-phenyl	127.64	136.74

Fully assigned ^{13}C NMR spectra of HL3 and $[Au(L3)Cl_2]$ are shown in Figures 5.3.3 and 5.3.4, respectively.

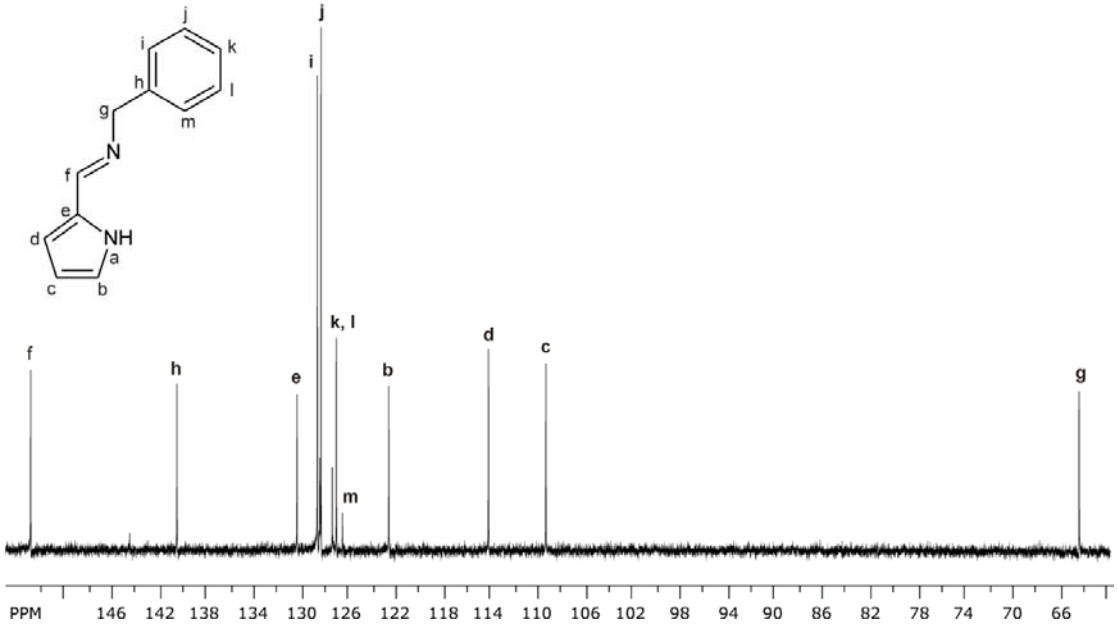

Figure 5.3.3: ^{13}C NMR spectrum of HL3 in DMSO at 298 K showing the spectral assignments.

Table 5.3.2 compares the ^{13}C NMR chemical shifts of the ligand HL3 and gold(III) chelate [Au(L3)Cl_2]. It shows an overall downfield shift upon chelation to the gold(III) cation. The pyrrole β-C exhibits the largest shift. This large shift is due to the deshielding effect of the gold(III) cation. The pyrrole γ-C has the smallest downfield shift as it is located furthest from the gold(III) cation, therefore it experiences minimal deshielding. This is in agreement with previously reported results.[18] The ^{13}C NMR spectral assignments for all the pyrrolide-imine ligands and gold(III) chelates are available in Chapter 2, these were assigned with the assistance of DFT calculations and two-dimensional NMR experiments.

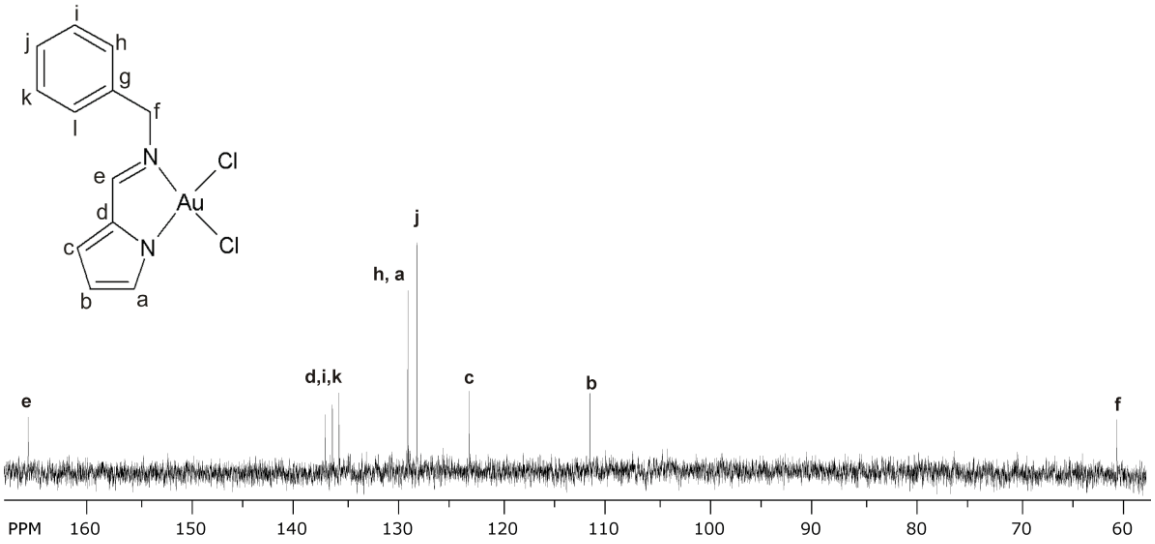

Figure 5.3.4: ^{13}C NMR spectrum of [Au(L3)Cl2] in DMSO at 298 K showing the spectral assignments.

5.4 Mass Spectrometry

Mass spectrometry is a technique used to determine the molecular mass of a compound. The instrumentation is made up of five components, these are illustrated in Figure 5.4.1. The first is the sample inlet, this is kept under vacuum. This takes the sample from the laboratory and places it under low pressure. The second chamber is the ion source which is under high pressure. This is where the sample is converted into the gaseous phase, this enters the mass analyser. The mass analyser separates the ions of the sample according to their mass-to-charge (*m/z)* ratio. These ions are then counted by the detector and then recorded and processed by the data system. The data is outputted as a mass spectrum, an example of which is shown in Figure 5.4.2.

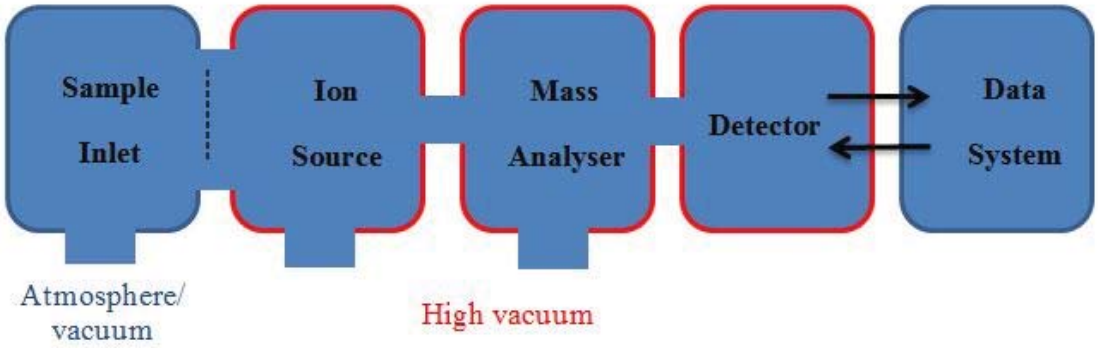

Figure 5.4.1: General layout of a mass spectrometer.[67]

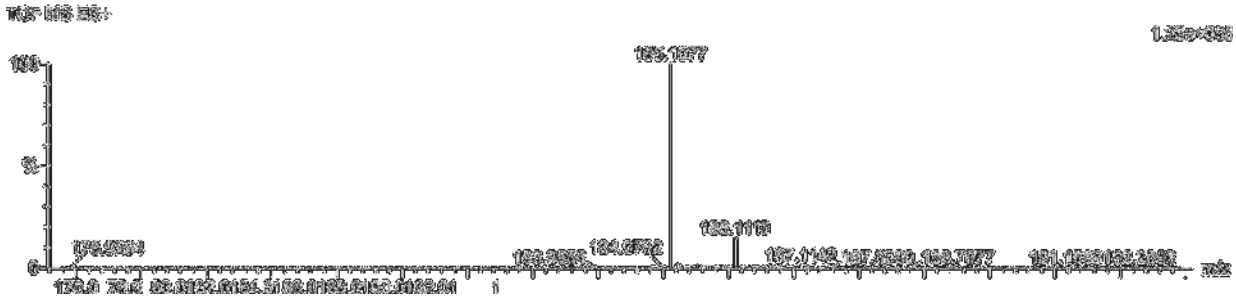

Figure 5.4.2: A high resolution mass spectrum of HL3.

The high resolution mass spectrum (Figure 5.4.2) recorded in the ES^+ mode clearly shows a peak at 185.11 m/z, which corresponds to the structure of the pyrrolide-imine ligand HL3, thus proving that the ligand was successfully synthesised. The mass spectrum values for the other ligands in this work are available in Chapter 2. Mass spectrometry of the gold(III) chelates was not possible as they broke into various fragments that were not easily analysed. This has been shown to be problematic in previous studies where the gold(III) ion breaks away from the ligand and leaves the fragmentation ion or the gold(III) chelate loses the chloride ligands in the ionisation process resulting in a charged gold(III) chelate.[66, 68, 71]

Chapter Six: Computational Chemistry

6.1 Introduction

6.1.1 The Density Functional Theory Method

Density Functional Theory (DFT) is a method which uses computational tools to study and predict properties of isolated molecules, bulk solids and material interfaces. The objective of DFT is to describe a many-body interacting system via particle density and not by its many-body wavefunction. The reasoning for DFT methods is to reduce the 3N degrees of freedom of an N-body system to three spatial coordinates in its particle density.[72] Once reduced, the characteristics of the system can be determined. (e.g. the lowest energy geometry, the NMR, electronic and vibrational spectra can be calculated). The size of the basis set and density functional used all influence the accuracy of a DFT simulation. For an accurate calculation an infinite number of functions need to be defined for a basis set, this is impossible due to time constraints, therefore computational restrictions have to be imposed on the basis set. The number of allowed positions of electrons is directly related to the computational time taken for a calculation. Therefore, the more restrictions placed on the region of space in which an electron is situated decreases the computational time taken, but also decreases the accuracy of the simulations.

The density functional used for all the calculations is B3LYP (Beck, 3-parameter, Lee-Yang-Parr).[73] This method takes into account the ionization potentials, proton affinities and total atomic energies.[73] Common inaccuracies with using B3LYP are increasing errors on C-X bond energies with increased alkylation and poor description of van der Waals interactions.[73]

The basis set used was either LanL2DZ or 6-311G. The basis set 6-311G was used for the free ligands. The basis set applies 6-311G to first-row atoms and the McLean-Chandler basis set to second-row atoms.[74-75] The basis set 6-311G was used because it is known to produce accurate results as it is a large basis set.[72] The 6-311G basis set can be applied for all atoms up to the end of the third row. The basis set LanL2DZ (Los Alamos National Laboratory 2 Double-Zeta) was used for the gold(III) chelates. This basis set can be used for atoms in the range H, Li-Ba, La-Bi and makes use of a combination of effective core potentials (ECP) and valence basis sets.

6.1.2 Previous Computational Studies of Pyrrolide-Imine Schiff Base Ligands

Munro *et al.*, reported a computational study for a ligand that has similarities to HL2.[49] This Schiff base ligand with a 1,2-diaminobenzene based spacer is shown below. A wide range of DFT methods have been used to study Schiff base ligands. In several reports, Munro *et al.* have probed the stability of hydrogen-bonded supramolecular structures supported by the pyrrole NH···imine hydrogen bond. Due to the limited computational power available at the time and the relative complexity of the supramolecular structures, semi-empirical AM1 calculations were used in the studies. These low level theory calculations still, however, yielded accurate results. They correctly predicted the geometry of the supramolecular structures and could explain in simple electrostatic terms the stability of this hydrogen bonding motif.[49]

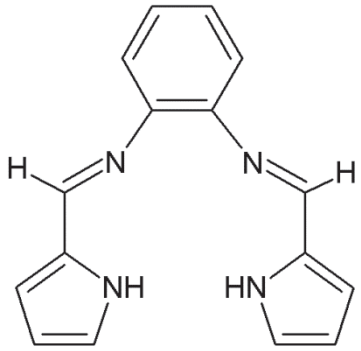

Figure 6.1.1: Structure of the 1,2-diaminobenzene Schiff base ligand.[49]

In later work, Munro *et al.* made use of DFT methods and the relatively large 6-31G** basis set while simulating the supramolecular structure of the monocondensation product of the 1,2-diaminobenzene Schiff base ligand. The Mullikan charges were calculated for the monomer and dimer structures of the hydrogen-bonded network. The gas-phase structure was calculated at the B3LYP/6-31G** level of theory. Overall there was reasonable agreement with the crystallographically observed conformation. One noticeable difference was that the calculated structure was more twisted then the X-ray structure.[11] This was illustrated by the torsion angle between the pyrrole and phenyl rings. The simulations showed that this deviation was possibly due to the geometric constraints imposed by the pair of hydrogen bonds between the interacting dimers in the experimental structure. The root-mean-square deviation (RMSD) between the two conformations is 0.37 Å for all non-H atoms of the calculated and experimental structures.[11] For the hydrogen-bonded dimer the RMSD is 0.413 Å for all non-hydrogen atoms. The mean calculated hydrogen bond distance was 2.32(1) Å, there is a slight deviation from the experimental value, but this is attributed to steric or other crystal packing interactions in the solid state structure.[11] Looking closely at the charge distribution it was observed that the natural atomic charge distributions for the monomer and dimer show good complementary electrostatic interactions for the H-bonded

dimer. The pyrrole NH carries an overall positive charge and the imine nitrogen atom carries a partial negative charge. If a hydrogen bond is considered to be a simple electrostatic interaction then the simulations clearly explain this hydrogen bonding motif.

The optimised geometries compared favourably with the experimental X-ray structures as shown with least squares fits of the calculated and experimental structures. These fits showed that a small degree of conformational distortion from the true low energy structure was required to allow for optimal hydrogen bonding in the case of the ligands.

6.1.3 Previous Computational Studies of Gold(III) Chelates

There are a limited number of examples of DFT calculations that have been performed on gold(III) chelates.[66, 71, 76-77] The basis set that is most widely used is LanL2DZ, which was used in this work. Various hybrid functions were implemented, but the most common was B3LYP which was applied in this work. It has consistently been shown that this hybrid functional gives reliable results.[77]

DFT simulations on gold(III) chelates have been reported by Wilson *et al*.[18] An example of the chelates studied in that work is shown in Figure 6.1.2. The simulations were performed at the LanL2DZ/HSEH1PBE level of theory. Overall there was good agreement between the experimental and DFT-calculated structures with RMSDs of < 0.100 Å. It was noted that the isoquinoline rings deviated from the experimental structures, this is due to the *in vacuo* DFT-calculated structures not taking into account the hydrogen bonding and π-stacking between the isoquinoline rings of the X-ray structure.[18]

The *cis* Au-Cl bonds have the same asymmetry observed in the X-ray structures with the Au-Cl *trans* to the amido N-donor being 0.033 Å longer (5%) than the other Au-Cl bond. The chelates had a mean Au-N_{amido} bond length of 2.014(5) Å and an Au-$N_{pyridine}$ bond distance of 2.035(3) Å.

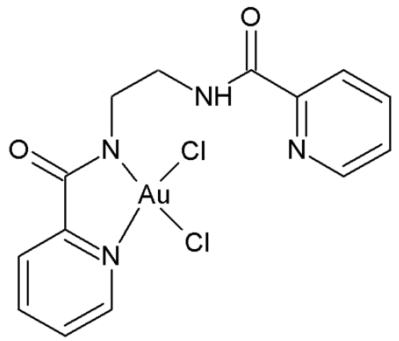

Figure 6.1.2: Structure of *cis*-dichloro{(pyridin-2-ylcarbonyl)[2-[(pyridin-2ylcarbonyl) amino]ethyl]azanido}gold(III).

Qin *et al*. reported the study of gold(III) complexes (Figure 6.1.3) under a C_{2v} symmetry constraint using the B3LYP functional and LanL2DZ basis set. This study showed good correlation between peak energies as well as electronic properties for the gold(III) complexes.[77] The DFT studies of gold(III) chelates described above have all made use of the B3LYP/LanL2DZ level of theory. The accuracy of these reported simulations would suggest that this level of theory is effective and that the use of effective core potentials for the gold(III) ion has not compromised the results. This level of theory has therefore been applied in this work.

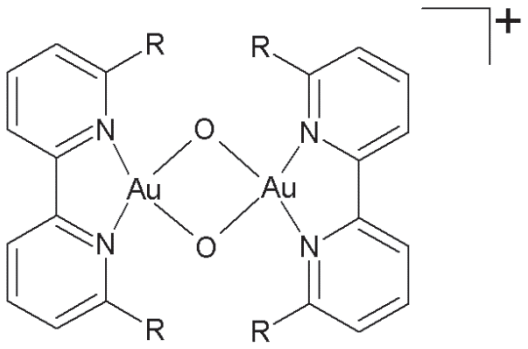

Figure 6.1.3: Structure of 4,4,2-di-*tert*-butyl-2,22-bipyridine (4,4,2-tBu$_2$bipy).[77]

6.2 Computational Method

The simulations for the ligands were performed at the B3LYP/6-311G(d,p) level of theory.[74-75, 78-82] Single first polarization functions (d,p) were added to the basis set to increase the accuracy of the simulations. 6-311G specifies the 6-311G basis set for first-row atoms and the McLean-Chandler (12s, 9p) basis sets for second-row atoms. The simulations for the gold(III) chelates were performed at the B3LYP/LanL2DZ (Los Alamos National Labs Double Zeta) level of theory.[83-85] The LanL2DZ basis set makes use of effective core potentials for the gold(III) ion. All simulations were performed using Guassian 09W. The X-ray coordinates were used for input structures in all cases except HL1 for which the input structure was generated using GaussView 5.0. Normal geometry convergence criteria were applied with no symmetry constraints imposed. Transition energies and oscillator strengths were calculated for 16 excited singlet states using the TD-DFT method[86-92] at the same level of theory applied to the geometry optimisations. The molecular orbitals were assigned by studying the spatial distributions of their isosurfaces. The input files were prepared using GaussView 5.0;[93] the same program was used to analyse the output files. The Guassian output files for the free ligands, ligand dimers and gold(III) chelates are available in **Appendix D**.

6.3 Computational Chemistry of Ligands

6.3.1 Geometry Optimisation Results

Geometry optimisation calculations were carried out on the pyrrolide-imine ligands synthesised in this work. It was noted that there was strong hydrogen bonding in the solid state leading to supramolecular dimeric structures; therefore the optimised structures were also calculated for these dimers. The same level of theory was used for the ligand monomers and dimers.

The geometry of the optimised structures are in good agreement with the solid state structures (Figure 6.3.1). The geometry optimisations were run *in vacuo* and are therefore free of intermolecular interactions. A comparison of the calculated and solid-state structures shows that the geometries of the solid-state structures are influenced by hydrogen bonding. The main differences between the experimental and calculated structures are discussed below. A summary of the average bond lengths and angles are shown in Table 6.3.1.

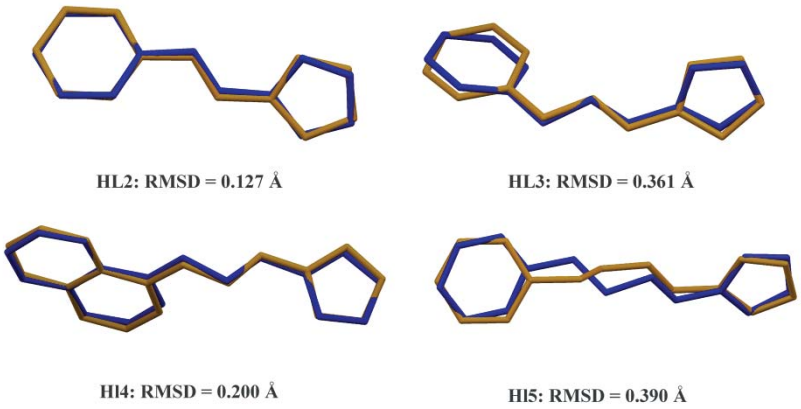

Figure 6.3.1: Least-squares fit of the non-H atoms of the DFT-calculated (orange) and X-ray crystal structures (blue) of the ligands that were studied by X-ray crystallography in this work, below each diagram is the RMSD.

The root-mean-square deviation is a measure of similarity between two structures; the lower the RMSD, the more similar the structures. Figure 6.3.1 shows that HL2 has the lowest RMSD of 0.127 Å compared to the other ligands. The lack of an alkyl spacer reduces the number of degrees of freedom in the structure and is hence more accurately simulated. The structure with the largest RMSD has the three methylene spacers. This is likely due to the increase in the number of degrees of freedom afforded by this extra spacing unit making it more susceptible to packing constraints in the solid state.

Table 6.3.1: Summary of the experimental and calculated bond lengths and bond angles of the pyrrolide-imine ligands.

Ligand	Torsion angle* (Å)		C=N-C angle (°)		C=N length (Å)	
	Calc.	**Exp.**	**Calc.**	**Exp.**	**Calc.**	**Exp.**
HL2	45.81	57.3(1)	121.17	124.3(1)	1.2839	1.287(2)
HL3	55.48	92.54(9)	121.61	123.7(1)	1.2764	1.277(1)
HL4	50.06	70.6(1)	121.74	124.1(1)	1.2764	1.277(1)
HL5	150.22	161.3(1)	121.66	125.0(1)	1.2761	1.271(2)

*Torsion angle between the pyrrole ring and aromatic moiety.

The most noticeable difference between the calculated and experimental free ligand structures lies in the position of the aromatic region relative to the pyrrole-imine moiety, as illustrated by the torsion angles in Table 6.3.1. The experimental data shows a non-zero torsion angle between the pyrrole ring mean plane and the aromatic moiety. This deviation between the calculated and experimental structures is possibly due to the lack of intermolecular interactions in the calculated structures, a similar trend was noted in previous work.[18] In the solid state it is observed that there is strong hydrogen bonding between two adjacent molecules, forming a dimer. It is possible that the molecules in the solid state undergo a degree of deformation from the lowest energy structure to allow for optimum hydrogen bonding. This hypothesis is probed further in section 6.3.2. The calculated imine bond parameters are all in good agreement with the experimental data. The accuracy of the optimised structures suggests that the level of theory applied in the simulations is appropriate.

6.3.2 Geometry Optimisation Results of Hydrogen-Bonded Dimers

The lowest energy conformations of the hydrogen-bonded dimers were calculated and compared to the experimental X-ray structures. The lowest energy conformations of the DFT calculated and experimental structures are shown in Figure 6.3.2, with corresponding RMSDs.

The root-mean-square deviations (RMSD) showed that the experimental and computational structures were in good agreement (Figure 6.3.2). It was noted that the monomeric structures of HL3 and HL5 have a higher RMSD value compared to the dimeric structures. This is an unusual result as usually there is an increase in the RMSD with an increase in the number of atoms used in the fits. This would suggest that the monomers undergo a moderate degree of conformational distortion from the lowest energy structure to allow for optimal hydrogen-bonding. Seemingly, the stability gained through the favourable hydrogen bonding is sufficient to offset the energy required for the deviation from the lowest energy geometry of the monomeric units.

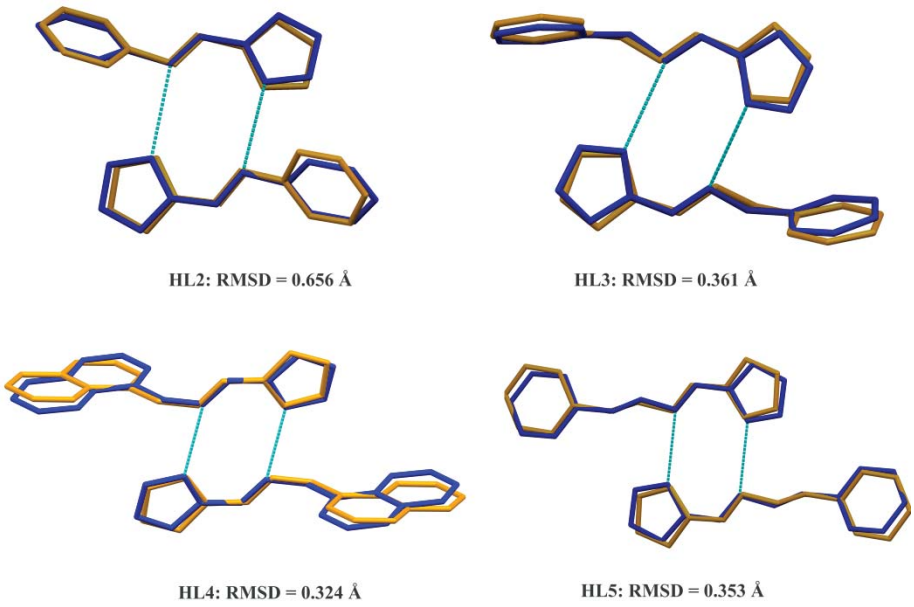

Figure 6.3.2: Lowest energy conformations of the DFT calculated (orange) and X-ray crystal structures (blue) of the hydrogen-bonded structures. The RMSD values were calculated using all non-hydrogen atoms. The hydrogen bonds are shown in blue.

6.3.3 Electrostatics of the Hydrogen-Bonded Dimers.

The NBO partial charges on the atoms of the hydrogen-bonded dimers were calculated since the partial charge distribution can give insight into the hydrogen bonding motifs.[32] Figure 6.3.3 below shows a labelled dimeric ligand with its partial charges. Table 6.3.2 summarises the partial charges for atoms involved in the pyrrole-imine hydrogen-bonded structures.

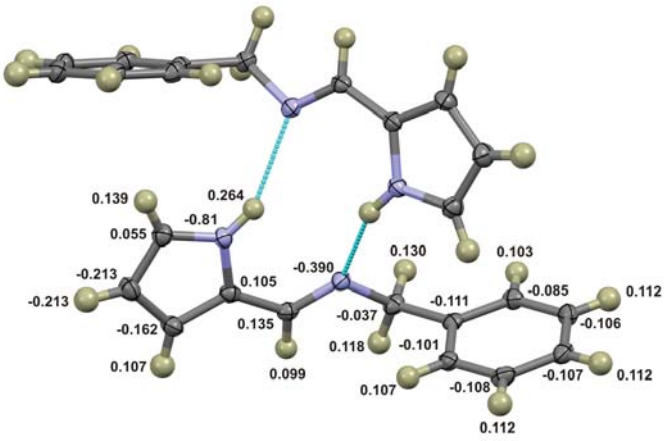

Figure 6.3.3: Partial charges for the dimeric structure of compound HL3. Due to the inversion symmetry of the dimer the partial charges are the same for each molecule, therefore only half of the dimer is labelled.

Table 6.3.2: Summary of average NBO partial charges that have been calculated for the hydrogen-bonded dimeric ligand structures (units of electrons).*

Ligand (Dimer)	N_{imine}	$N_{pyrrole}$	Pyrrole NH
HL1	-0.532	-0.516	0.448
HL2	-0.547	-0515	0.446
HL3	-0.535	-0.519	0.449
HL4 (A)	-0.531	-0.520	0.449
HL4 (B)	-0.541	-0.519	0.449
HL5	-0.535	-0.517	0.448

*The partial charges shown are those calculated for the atoms directly involved in hydrogen bonding.

The above table shows that overall the N_{imine} has the most negative partial charge while the pyrrole NH hydrogen atom is the most electropositive, as shown in Figure 6.3.3. If hydrogen bonding is considered to be a simple electrostatic interaction then the stability of this hydrogen bonding motif is clearly supported by the NBO charges. This follows the same trend that was stipulated in Munro *et al*.[11] A comparison of hydrogen bond lengths between the calculated and experimental data is shown in Table 6.3.3.

Table 6.3.3: Summary of calculated and experimental hydrogen bond lengths (Å) for the pyrrolide-imine ligands in this work.

Bond	HL1		HL2		HL3		HL4		HL5	
	Exp.	Calc.	Exp.	Calc.	Exp.	Calc.	Exp.	Calc.	Exp.	Calc.
N···N	N/A	3.024	2.99(1)	3.000	3.04(1)	3.025	2.96(1)	2.996	2.99(2)	2.993

Table 6.3.3 shows that in general, the calculated bond lengths are shorter than the experimental hydrogen bond lengths. In the absence of the packing constraints experienced in the solid state it is possible for the molecules comprising the dimer to approach more closely, leading to a shorter interaction distance.

6.3.4 Vibrational Frequency Results for the Pyrrolide-Imine Ligands

The vibrational frequencies were calculated to firstly determine if the geometry optimisation results were at a true minimum on the global potential energy surface and secondly to compare the frequencies of the calculated spectra to the experimental IR data. The frequencies were compared by plotting a superposition of the experimental IR spectra with the calculated frequency data. An example of these superposition plots is shown in Figure 6.3.4 below. As the other complexes have similar vibrational frequencies they have not been shown here, but are available in **Appendix E**.

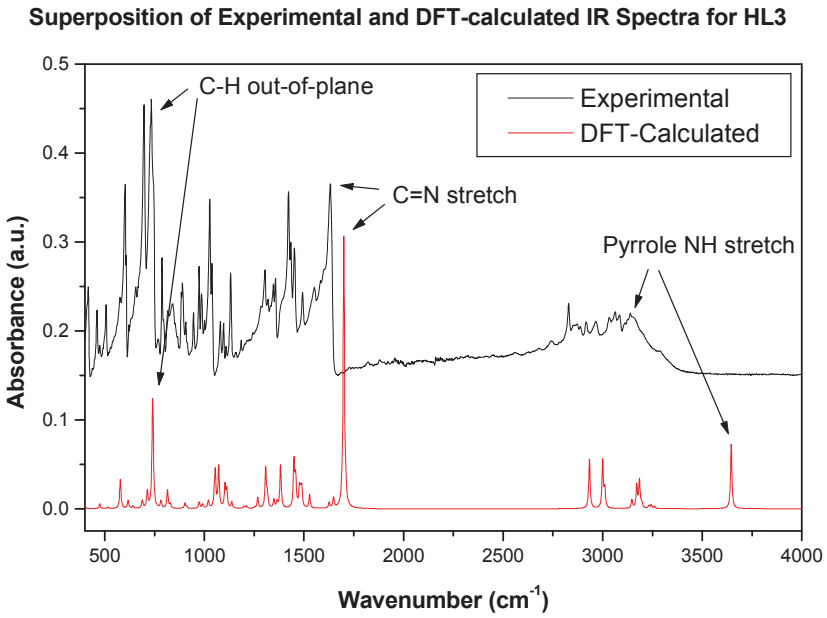

Figure 6.3.4: Superposition of experimental and DFT-calculated IR spectra for ligand HL3. The DFT-calculated spectrum has been scaled to match the intensity of the experimental spectrum.

The overlay of experimental and calculated frequency data in Figure 6.3.4 shows moderate correlation between experimental and calculated results. The relative intensities of the IR spectra show a satisfactory correlation, but there is consistent overestimation of the frequency of the absorption bands with regard to the calculated data. It is noteworthy that the higher energy peaks, such as the pyrrole NH stretching frequencies, are poorly calculated, whereas the lower frequency peaks are more accurately predicted. The data in Table 6.3.4 shows a comparison of experimental and calculated frequencies for the pyrrolide-imine ligands which overall show moderate correlation. Figure 6.3.5 shows a plot of DFT-calculated versus experimental frequencies, which shows a linear correlation between the two sets of data suggesting that the error in the simulated spectra is systematic and could be improved by applying a correction factor (the slope of the line gives the correction factor).

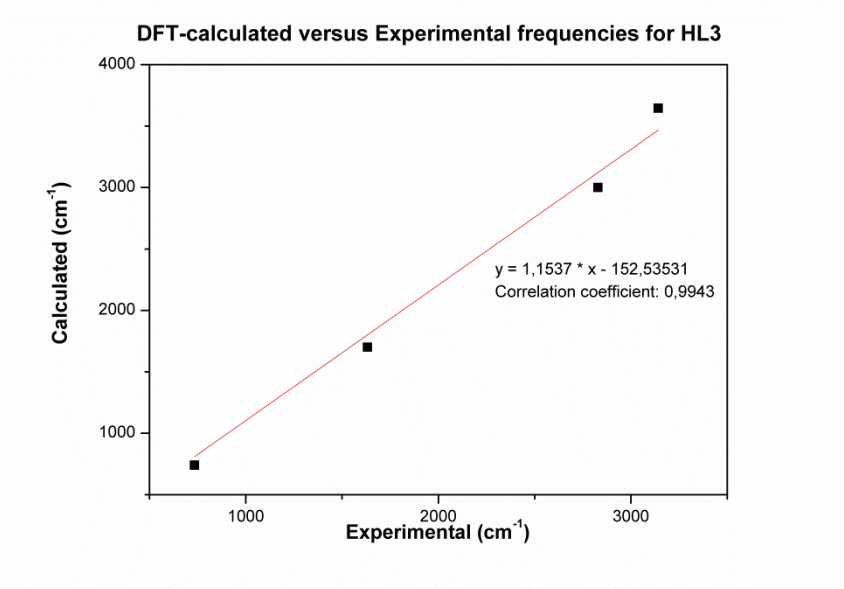

Figure 6.3.5: Linear plot of DFT-calculated and experimental frequencies for HL3.

Table 6.3.4 shows the calculated and experimental frequency data; there is good correlation with the C=N and imine C-H stretch with the average percentage difference below 7%. The pyrrole N-H difference is much greater, up to 16%. The pyrrole C-H out-of-plane bend was very accurately calculated with errors below 1%.

Table 6.3.4: Comparison of experimental and calculated frequencies of pyrrolide-imine ligands.

Proton		C=N	Imine C-H	Pyrrole N-H	Pyrrole C-H bend
HL2	Exp.	1617.19	2842.25	3213.20	741.5
	Calc.	1673.92	3035.24	3645.27	741.726
	% Dif.	-3.51	-6.79	-13.45	-0.03
HL3	Exp.	1632.18	2828.94	3142.25	734.0
	Calc.	1700.04	2999.72	3645.38	739.646
	% Dif.	-4.16	-6.04	-16.01	-0.77
HL4	Exp.	1643.69	2853.13	3170.73	729.34
	Calc.	1701.02	3002.46	3647.06	739.31
	% Dif.	-3.49	-5.23	-15.02	-1.37
HL5	Exp.	1642.87	2847.01	3162.43	739.6
	Calc.	1698.79	2999.40	3645.75	737.449
	% Dif.	-3.40	-5.35	-15.28	0.29

*Percentage difference is calculated as $\left(\frac{\text{Exp}-\text{Calc}}{\text{Exp}}\right) \times 100\%$

6.3.5 Electronic Transition Results for the Schiff Base Ligands

The electronic transitions were calculated for the pyrrolide-imine ligands using the TD-DFT method solving for 16 excited states. The results from the simulations were compared to the experimental UV/visible absorption spectra. In general, the correlation between the experimental and calculated results is satisfactory. Shown below in Figure 6.3.1 is an overlay of the calculated and experimental results for ligand HL3 as a representative example. The electronic transition calculations were also used to show which ligand orbitals are involved in the transitions.

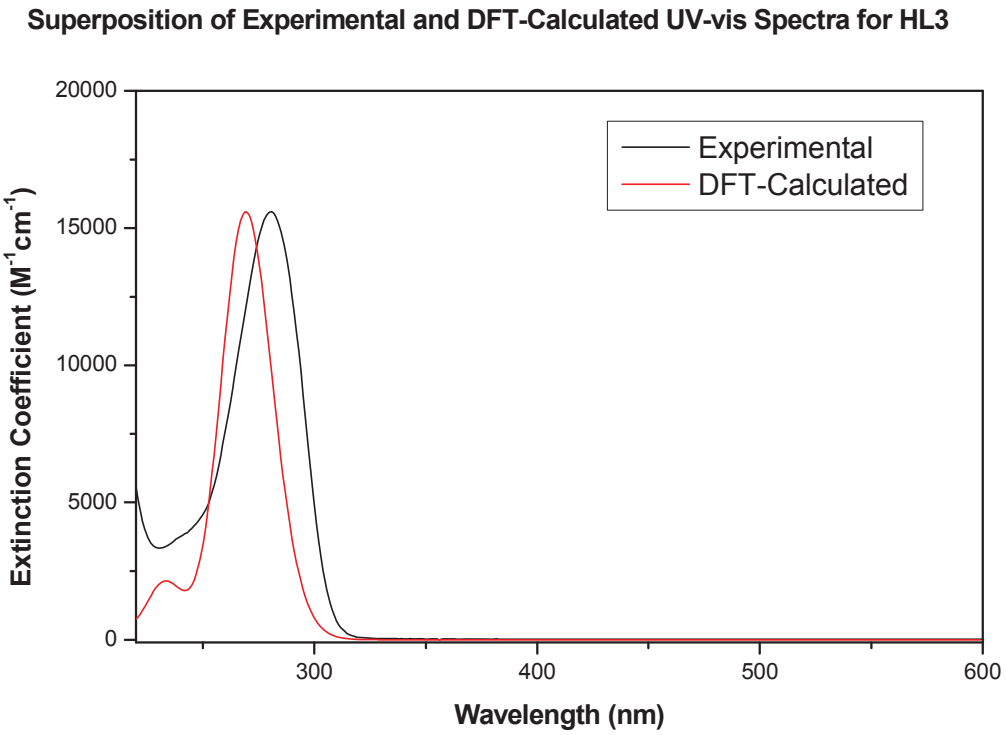

Figure 6.3.6: Superposition of the experimental and DFT-calculated UV/visible spectra of ligand HL3. The λ_{max} values are 281 and 261 nm for the experimental and calculated spectra, respectively. The calculated spectrum has been scaled.

The overlay of calculated and experimental UV/visible data for ligand HL3 shows excellent correlation. The absorption bands depicted in Figure 6.3.6 are made up of several electronic transitions with various oscillator strengths. The calculated transitions are summarised in Table 6.3.5 for HL3 for both the monomer and dimer. The electronic transitions responsible for the absorption spectra for the bulk of the ligands and their dimers are summarised in Table 6.3.6.

Table 6.3.5: Summary of calculated electronic transitions for the ligand HL3, and the electronic orbitals involved.

MONOMER			
Wavelength(nm)	**Molecular Orbitals**	**Symmetry of Orbitals**	**Oscillator strength**
232.54	HOMO-3 → LUMO	π→π*	0.0822
	HOMO→ LUMO+3	π→σ*	
261.85	HOMO-4→LUMO	π→π*	0.0862
	HOMO-1→LUMO	π→π*	
270.21	HOMO→LUMO	π→π*	0.6054
	HOMO-1→LUMO	π→π*	
DIMER			
272.36	HOMO→LUMO	π→π*	1.1761
	HOMO-1→LUMO+1	π→π*	
281.67	HOMO-1→LUMO	π→π*	0.0725
	HOMO→ LUMO+1	π→π*	

The major orbitals that are involved in the different transitions in HL3 are shown in Figure 6.3.7. The molecular orbitals of the remaining ligands are similar to those of HL3 and are therefore not shown here, but are available in **Appendix E.** The transitions shown in Table 6.3.5 all involve ligands of π-symmetry, except the π→σ* transition seen at a wavelength of 232.54 nm. The most significant transition, as determined by oscillator strength, involves a $\pi \rightarrow \pi^*$ transition between the HOMO and LUMO orbitals. The transition with the largest oscillator strength for the dimer of HL3 is between the HOMO and LUMO orbitals as well as between the HOMO-1 and LUMO+1 orbitals both of which are $\pi \rightarrow \pi^*$ transitions.

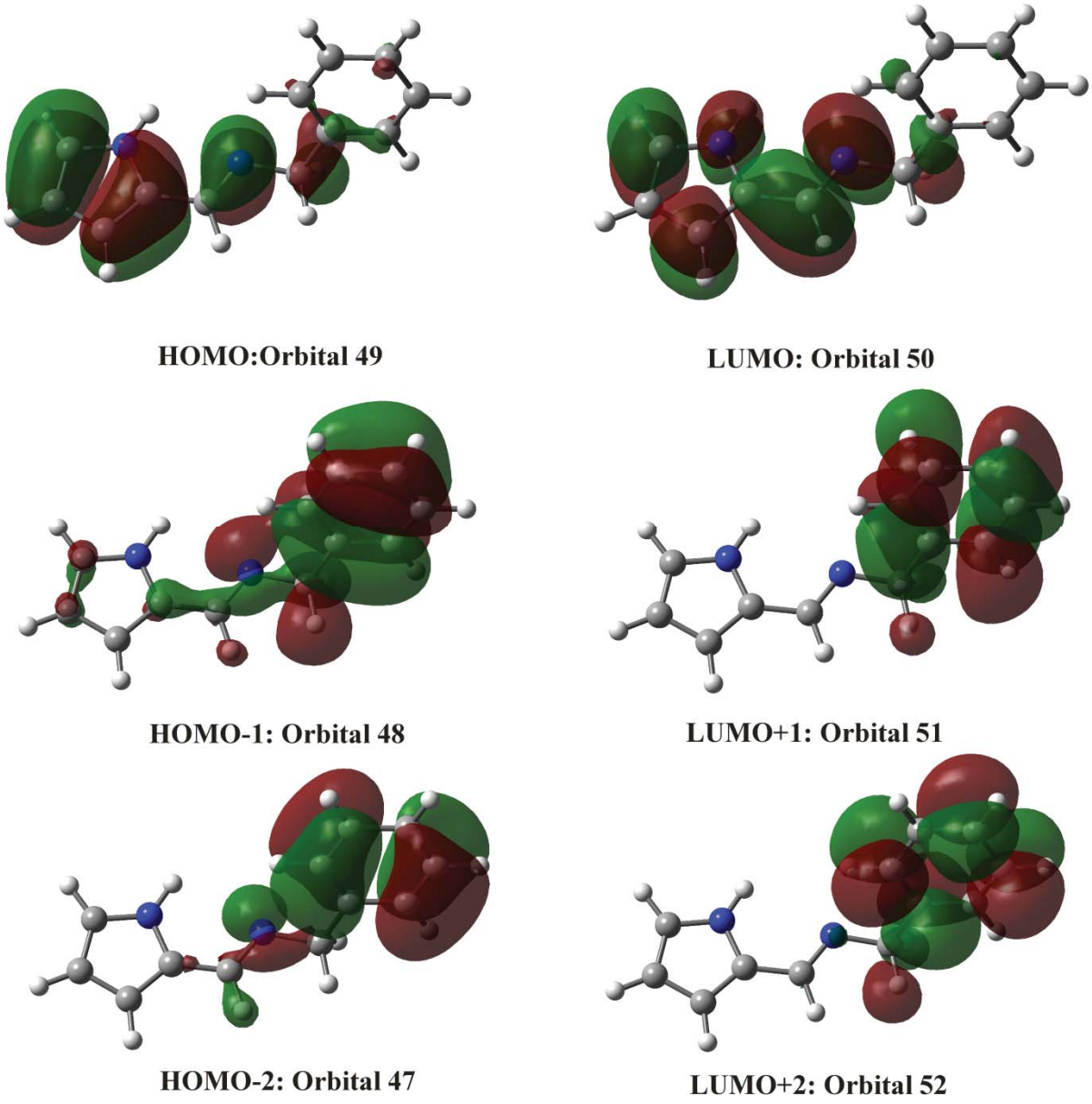

Figure 6.3.7: The molecular orbitals of HL3 responsible for the major electronic transitions. All the orbitals shown are of π-symmetry.

Figure 6.3.8 below shows that the HOMO and LUMO orbitals are delocalised over both monomeric units of the dimer structures. The orbitals located on each monomer are approximately equal in size, this suggests that the dimer molecular orbitals consist of approximately 50% mix and thus there is contribution from each of the monomers to the electronic structure of the dimer. This mixing has previously been seen where the HOMO resides on both monomers of the dimer. If mixing did not occur the HOMO orbital would be localised on one monomer and the HOMO-1 orbital would be located on the alternative monomer in the dimer. The other ligands show a similar mixing of electronic orbitals, this indicates that the monomers become electronically mixed when they form dimers.[11]

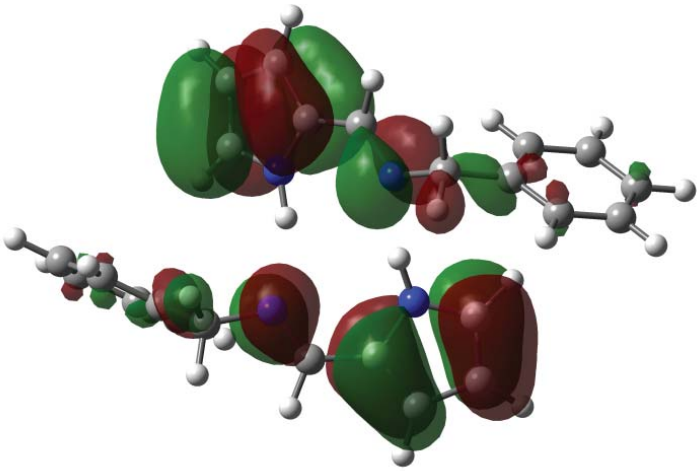

Figure 6.3.8: HOMO of the hydrogen-bonded dimer HL3 showing equal sized lobes on each monomer.

Table 6.3.6: Summary of calculated and experimental electronic transitions for the ligands and the molecular orbital involved.

Ligand	Exp. (nm)		Calc. (nm)	Symmetry Orbitals	Type	Oscillator Strength
HL1	277	Monomer	176.6	HOMO-3→LUMO	π→π*	0.334
				HOMO→LUMO+2	π→π*	
			184.84	HOMO-3→LUMO	π→π*	0.082
				HOMO→ LUMO+1	π→π*	
			231.64	HOMO-1→LUMO	π→π*	0.070
			276.98	HOMO→LUMO	π→π*	0.763
		Dimer	236.11	HOMO-3→LUMO+1	π→π*	0.1236
				HOMO-2→LUMO	π→π*	
			260.58	HOMO-1→LUMO	π→π*	1.30
				HOMO→LUMO+1	π→π*	
			288.82	HOMO-1→LUMO	π→π*	0.0236
HL2	322	Monomer	244.35	HOMO → LUMO+1	π→π*	0.0516
			251.83	HOMO-3 → LUMO	π→π*	0.047
				HOMO-2 → LUMO	π→π*	
			282.45	HOMO-1 → LUMO	π→π*	0.1645
				HOMO-4 → LUMO	π→π*	
			325.64	HOMO → LUMO	π→π*	0.7731
				HOMO-1 → LUMO	π→π*	
		Dimer	256.03	HOMO-4 → LUMO	π→π*	0.0799
				HOMO-6 → LUMO	π→π*	
				HOMO-5 → LUMO+1	π→π*	
			275.1	HOMO-3 → LUMO	π→π*	0.2052
				HOMO-2 → LUMO	π→π*	
			313.26	HOMO-1 → LUMO+1	π→π*	1.3808
				HOMO → LUMO	π→π*	
			326.98	HOMO-1 → LUMO	π→π*	0.1727
				HOMO → LUMO+1	π→π*	
HL4	223	Monomer	233.28	HOMO–3→LUMO+1	π→π*	0.0712
	283		267.64	HOMO→LUMO+1	π→π*	0.6523
				HOMO-1→LUMO	π→π*	
			288.91	HOMO-1→LUMO	π→π*	0.1846
			298.03	HOMO→LUMO+1	π→π*	0.702
		Dimer	287.89	HOMO→LUMO+2	π→π*	0.0609
				HOMO-2→LUMO	π→π*	
			289.83	HOMO-3→LUMO	π→π*	0.0679
			289.99	HOMO-2→LUMO	π→π*	0.0479
			304.99	HOMO-1→LUMO	π→π*	0.3463
				HOMO→LUMO+1	π→π*	
HL5	279	Monomer	205.25	HOMO-1→LUMO+2	π→π*	0.0259
			231.3	HOMO-3→LUMO	π→π*	0.0557
				HOMO-1→LUMO	π→π*	
			269.6	HOMO→LUMO	π→π*	0.7658
		Dimer	239.1	HOMO-4→LUMO	π→π*	0.0636
				HOMO-3→LUMO	π→π*	
			266.3	HOMO→LUMO+1	π→π*	1.6303
			292.19	HOMO-1→LUMO	π→π*	0.037
				HOMO→LUMO+1	π→π*	

6.3.5 Calculated NMR Spectral Data of the Pyrrolide-Imine Ligands

The ^{1}H and ^{13}C NMR spectra of the pyrrolide-imine ligands were calculated using the GIAO method at the same level of theory used to optimise the ligand geometries. A dimethyl sulfoxide solvent model was also included in the simulations to allow for any solvent effects. The agreement between the experimental and calculated ^{1}H NMR values is acceptable. The calculated and experimental shifts are summarised in Table 6.3.6. Table 6.3.6 shows the chemical shifts for the calculated ^{1}H NMR spectra are consistently overestimated compared to the experimental shifts. The pyrrole N-H is the only exception to this trend, the calculated chemical shifts being consistently underestimated compared to the experimental chemical shifts.

The experimental data was plotted against the calculated data in order to determine if there was a systematic correlation between the experimental and calculated data. This showed that the error was systematic as there is a linear correlation between the two parameters. Table 6.3.6 shows that the percentage differences were moderate. It is noted that the imine and pyrrole NH chemical shifts both have much higher percentage differences compared to the other proton in the molecule. The poor estimation of the pyrrole NH is likely due to hydrogen bonding interactions in the experimental spectra which are not accounted for in the simulations.

Table 6.3.6: ^{1}H NMR chemical shifts for the experimental and calculated structures of the ligands in this work and their percentage difference.

Proton		δ	γ	β	Imine	NH
HL1	Exp.	6.85	6.09	6.44	8.04	11.34
	Calc.	7.62	6.97	7.18	8.91	9.56
	% Dif.	-11.24	-14.45	-11.49	-10.82	15.70
HL2	Exp.	7.02	6.20	6.71	8.28	11.73
	Calc.	7.79	7.08	7.47	8.94	9.80
	% Dif.	-10.97	-14.19	-11.33	-7.97	16.45
HL3	Exp.	6.89	6.89	6.89	8.20	11.43
	Calc.	7.73	7.03	7.29	9.02	9.78
	% Dif.	-12.19	-2.03	-2.03	-10	14.44
HL4	Exp.	6.87	6.11	6.48	8.29	11.41
	Calc.	7.77	7.07	7.34	9.16	9.87
	% Dif.	-13.10	-15.71	-13.27	-10.49	13.50
HL5	Exp.	6.89	6.07	6.39	8.00	11.35
	Calc.	7.66	6.99	7.22	8.96	9.61
	% Dif.	-11.18	-15.16	-12.98	-12.00	15.33

*Percentage difference is calculated as $\left(\frac{Exp-Calc}{Exp}\right) \times 100\%$

The calculated ^{13}C NMR chemical shifts shown in Table 6.3.7 compare favourably with the experimental data, the average percentage difference for the δ and imine carbon chemical shifts being below 2.5%. The mean percentage difference for the chemical shifts of the α, β and γ carbon atoms are less than 4%. This difference is minimal and shows that there is good agreement between the experimental and calculated chemical shifts. The percentage differences are mainly negative errors; this means that the calculated chemical shifts are consistently downfield relative to the experimental data. Therefore the DFT calculations are not calculating precise shielding tensors; the calculated carbon atoms are less shielded than the experimental carbons. In HL2 there are only two positive percentage errors, for the γ and β carbons, this shows that the error in the calculated shielding tensor of each carbon atom for this ligand is not systematic.

The experimental data were plotted against the calculated data (Figure 6.3.9) to determine if the error in the data is systematic and could therefore be accounted by applying a correction or scaling factor.

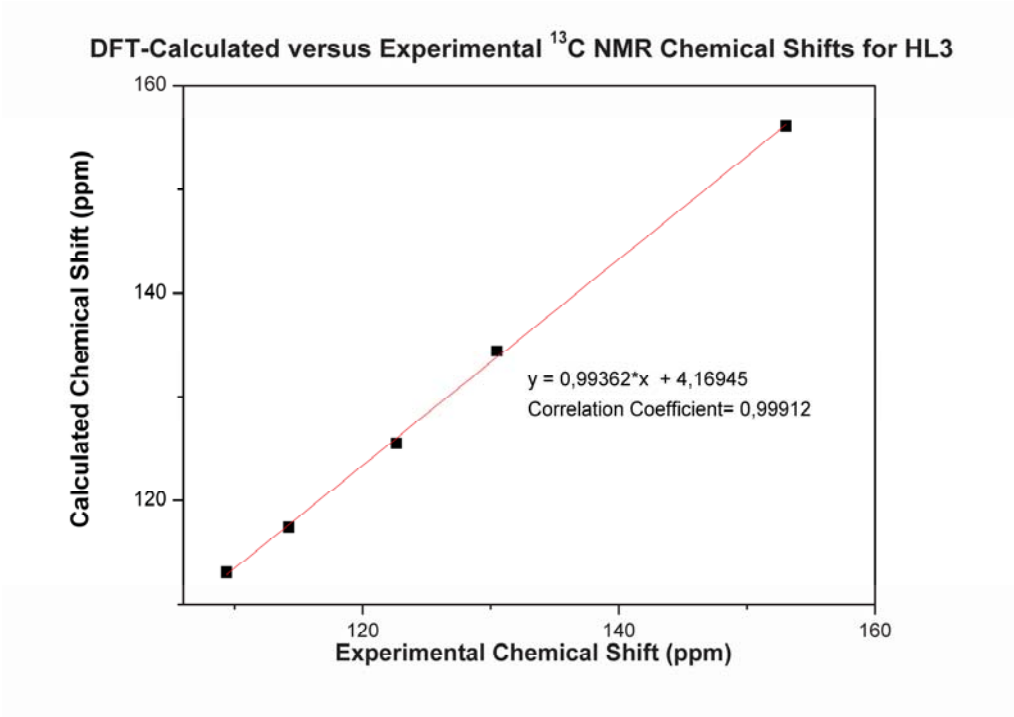

Figure 6.3.9: Plot of DFT-calculated and experimental ^{13}C NMR chemical shifts for HL3.

The linear correlation in Figure 6.3.9 shows that the error in the calculated ^{13}C NMR chemical shifts is systematic and a correction factor could therefore be applied to improve the accuracy of the data. Similar plots for the bulk of the ligands are available in **Appendix E**.

Table 6.3.7: Summary of experimental and calculated ^{13}C NMR chemical shifts for the Schiff base ligands.

Ligand		δ	γ	β	α	Imine
HL1	Exp.	122.30	109.24	113.59	130.53	151.99
	Calc.	124.71	112.80	116.37	134.49	152.72
	% Dif.	-1.97	-3.26	-2.45	-3.03	-0.48
HL2	Exp.	123.77	116.35	120.69	130.48	150.51
	Calc.	127.05	114.07	120.02	135.42	151.22
	% Dif.	-2.65	1.96	0.56	-3.79	-0.47
HL3	Exp.	122.64	109.38	114.24	130.48	153.05
	Calc.	125.53	113.09	117.44	134.44	156.12
	% Dif.	-2.36	-3.39	-2.80	-3.03	-2.01
HL4	Exp.	122.71	109.40	114.23	131.67	153.30
	Calc.	125.75	113.24	117.70	134.62	156.16
	% Dif.	-2.45	-3.51	-3.04	-2.24	-1.87
HL5	Exp.	121.93	108.73	113.26	129.94	151.97
	Calc.	125.02	112.92	116.89	134.26	153.41
	% Dif.	-2.53	-3.86	-3.21	-3.32	-0.95

*Percentage difference is calculated as $\left(\frac{\text{Exp}-\text{Calc}}{\text{Exp}}\right) \times 100\%$

The ^{13}C and ^{1}H NMR chemical shifts of the calculated spectra were in moderate agreement with the experimental chemical shifts (Table 6.3.6 and 6.3.7). This shows that the basis set 6-311G (dp) was effective for these calculations.

6.4 Computational Chemistry of Gold Chelates

6.4.1 Geometry Optimisation Results

The lowest energy geometries for the bidentate pyrrolide-imine gold(III) chelates were calculated. These calculated structures were compared to the X-ray structures as a measure of the accuracy of the simulations.

As the calculations were carried out in the gas phase there will be no intermolecular forces taken into account. It has been shown that intermolecular forces play a role in influencing the geometry of the chelates in the solid state. The X-ray diffraction studies (Chapter Four) showed that there are multiple interactions between the gold chelates such as π···π, Au···π and Au···Au all of which influence the geometry of the chelates. The imine and pyrrole region are planar in the calculated structure, this is expected as there is a preference for the

ligand to be square planar around the gold(III) ion due to its vacant $d(x^2\text{-}y^2)$ orbitals. The aromatic appendage of the chelates do not occupy the same plane as the gold(III) ion and pyrrole ring.

A least squares fit was used to determine the accuracy of the calculated structures compared to the X-ray structures, the similarity is measured in terms of the RMSD values which are shown in Figure 6.4.1. The similarity of the calculated and experimental structures suggests that although intermolecular interactions are important they do not greatly influence the geometry of the structures. This is possibly due to the fact that gold(III) ion forms a rigid square planar chelate with the pyrrole-imine moiety and thus resists distortions. Although the pyrrolide-imine region is planar, the aromatic substituents showed an out-of-plane rotation for all the chelates except [Au(L5)Cl_2]. The extended linkages between the aromatic appendages and imine bonds of [Au(L5)Cl_2] allow for a co-planar orientation to be adopted. This is because the chelates with a shorter chain length experience steric strain between the phenyl hydrogen atoms and chloride ligands, and therefore rotate out-of-plane to alleviate this strain.

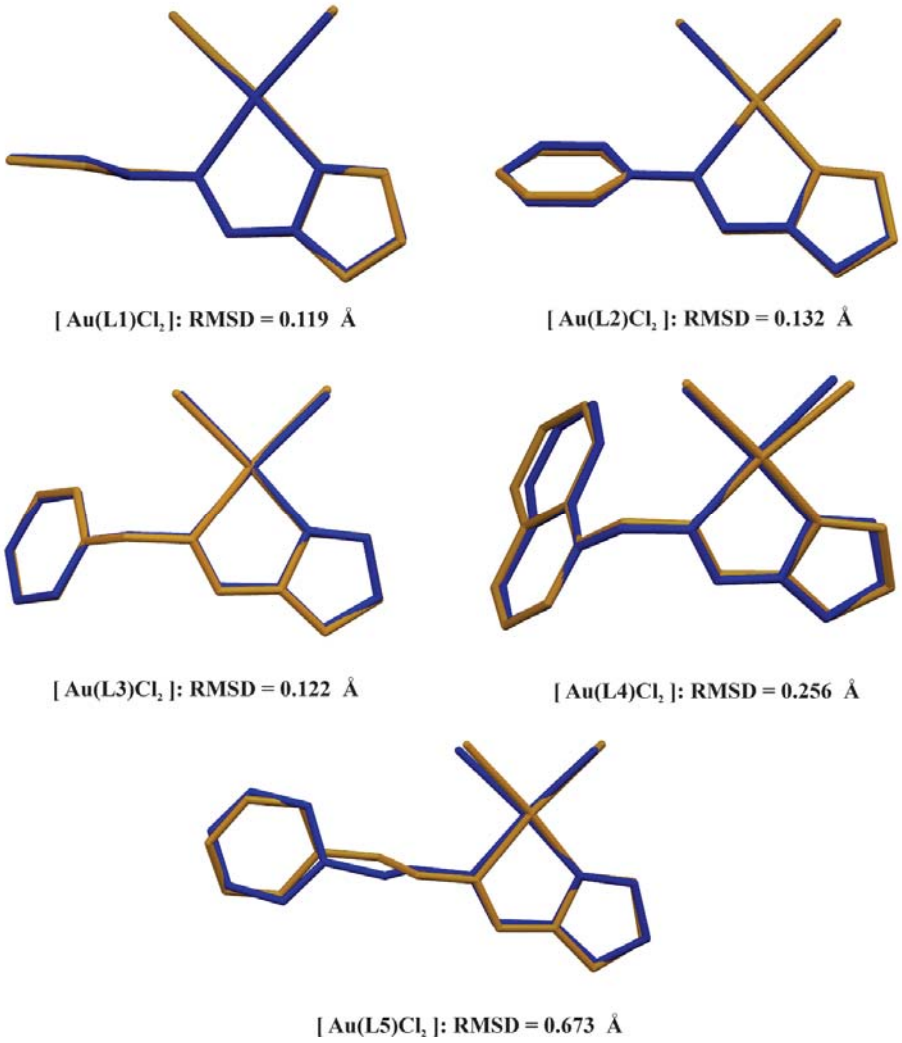

Figure 6.4.1: Least squares fit of the non-hydrogen atoms of the DFT calculated (orange) and X-ray crystal structures (blue) of the gold(III) chelates. The RMSDs are indicated on the diagram.

The geometric parameters for the gold(III) chelates summarised in Table 6.4.1 show that in general, the coordination sphere of the gold(III) ion was accurately simulated. The greatest deviation is with the Au-Cl bonds which are significantly longer in the calculated structures. These data coupled with the low RMSDs show that the structures were accurately calculated. This would suggest that the basis set used was appropriate and should produce reliable results in the bulk of the simulations.

Table 6.4.1: Comparison of the bond lengths (Å) and bond angles (°) of the experimental and calculated structures of the gold(III) chelates.

Complexes		**Bond Lengths (Å)**				**Bond Angles (°)**
		Au-$N_{pyrrole}$	**Au-N_{imine}**	**Au-Cl1**	**Au-Cl2**	**N_{imine}-Au-$N_{pyrrole}$**
[Au(L1)Cl_2]	Exp.	1.993(4)	2.035(6)	2.275(1)	2.276(2)	81.02(2)
	Calc.	2.0277	2.0897	2.4066	2.4030	80.35
	% Dif.	-1.7	-2.6	-5.5	-5.3	0.8
[Au(L2)Cl_2]	Exp.	1.985(4)	2.045(3)	2.2834(9)	2.273(1)	80.8(1)
	Calc.	2.0308	2.1133	2.4005	2.4070	80.17
	% Dif.	-2.3	-3.3	-4.9	-5.6	0.8
[Au(L3)Cl_2]	Exp.	1.97(1)	2.05(1)	2.292(4)	2.274(4)	81.5(5)
	Calc.	2.0258	2.0908	2.4067	2.4028	80.36
	% Dif.	-2.6	-2.0	-4.8	-5.4	1.4
[Au(L4)Cl_2]	Exp.	1.985(4)	2.045(3)	2.276(1)	2.270(1)	80.8(1)
	Calc.	2.0255	2.0933	2.4080	2.4037	80.40
	% Dif.	-2.0	-2.3	-5.5	-5.6	0.5
[Au(L5)Cl_2]	Exp.	1.98(1)	2.04(1)	2.275(4)	2.281(4)	80.4(6)
	Calc.	2.0263	2.0901	2.4073	2.4028	80.34
	% Dif.	-2.3	-2.4	-5.5	-5.1	0.1

*Percentage difference is calculated as $\left(\frac{\text{Exp}-\text{Calc}}{\text{Exp}}\right) \times 100\%$

6.4.2 Vibrational Frequency Results

The vibrational frequencies were calculated to firstly determine whether the geometry optimisation results were the true minimum on the global potential energy surface and secondly to compare the frequencies of the calculated spectra to the experimental IR spectra. The frequencies were compared by plotting a superposition of the experimental IR and calculated frequency data. An example of these superposition plots is shown in Figure 6.4.2.

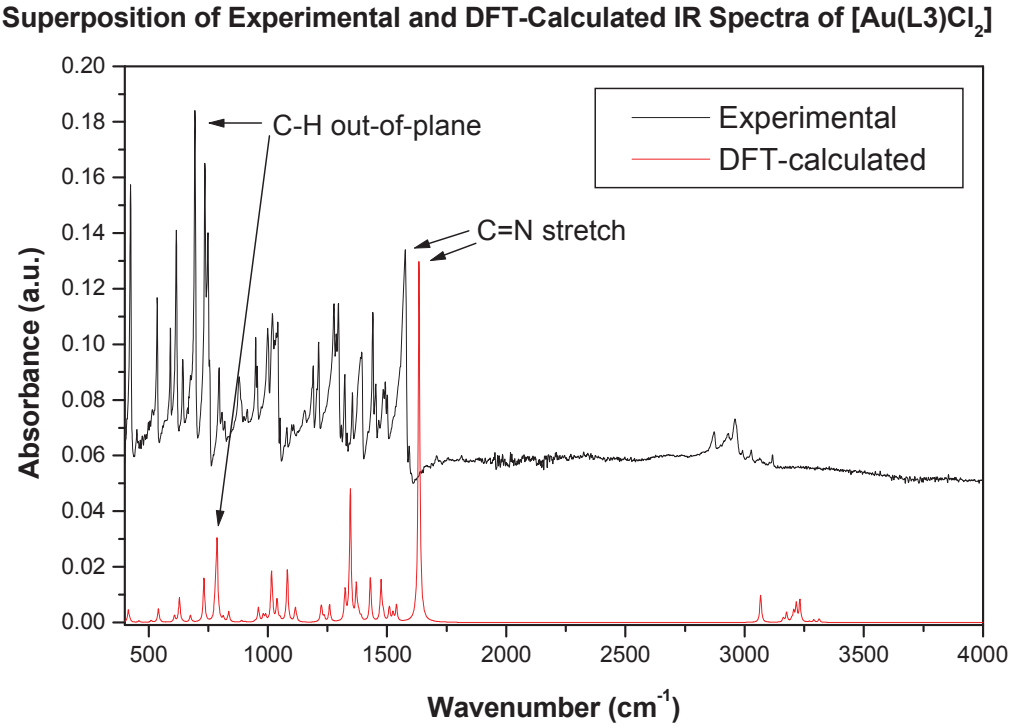

Figure 6.4.2: Superposition of experimental and DFT-calculated IR spectra. DFT-calculated data has been scaled.

Figure 6.4.2 shows that the frequency calculations are reasonably accurate. The relative intensities of the peaks have been accurately simulated. The absolute values of the vibrational frequencies have, however, been overestimated in general. Table 6.4.2 shows the C-H wagging, C=N stretch and imine C-H stretch vibrational frequencies of the various gold(III) chelates. The data were compared to the experimental results to get a measure of their accuracy. The frequencies were both over and under estimated. The C=N stretch being fractionally underestimated with a mean percentage difference of 2.5%. The imine C-H stretch and C-H waging show poor correlation with percentage errors up to 12.3%. The plot of calculated versus experimental frequencies in Figure 6.3.3 is linear. This suggests that the error in the calculations is systematic and could be corrected by applying a scaling factor which could be derived from the slope of the graph.

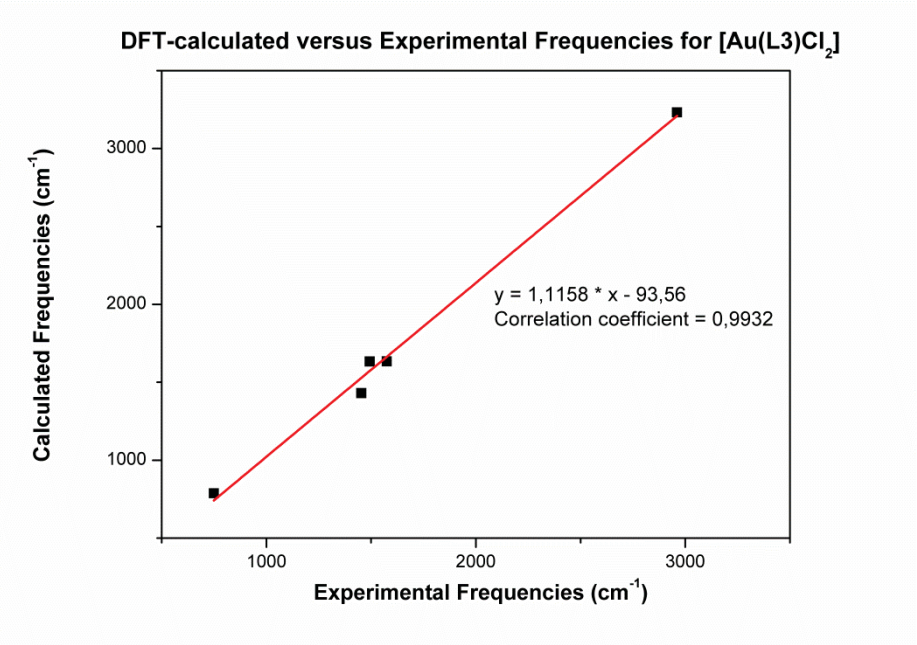

Figure 6.3.3: Linear plot of DFT-calculated and experimental frequencies for [Au(L3)Cl_2].

Table 6.4.2: Summary of calculated and experimental vibrational frequencies and their percentage errors for the gold(III) chelates.

Vibration		C-H bend (out of plane)	C-H bend (in plane)	C = C stretch	C = N stretch	Aromatic C-H stretch
[Au(L1)Cl_2]	Exp.	748.9	1432.6	1440.1	1576.1	-
	Calc.	787.48	1430.39	1476.08	1636.49	-
	% Dif.	-5.15	0.15	-2.50	-3.83	-
[Au(L2)Cl_2]	Exp.	734.88	1425.31	1546.47	1634.66	2953.14
	Calc.	716.51	1427.91	1624.69	1627.66	3207.02
	% Dif.	2.50	-0.18	-5.06	0.43	-8.60
[Au(L3)Cl_2]	Exp.	748.9	1453.1	1493.42	1575.15	2961.03
	Calc.	787.03	1430.11	1633.34	1634.41	3232.14
	% Dif.	-5.09	0.58	-9.37	-3.76	-9.16
[Au(L4)Cl_2]	Exp.	749.21	1439.23	1571.57	1662.12	2956.72
	Calc.	787.38	1429.34	1627.89	1633.82	3220.56
	% Dif.	-5.09	0.68	-3.58	1.70	-12.31
[Au(L5)Cl_2]	Exp.	744.20	1389.46	1444.66	1577.31	2925.18
	Calc.	787.33	1429.44	1632.87	1635.69	3229.35
	% Dif.	-5.80	-2.88	-13.03	-3.70	-10.40

*Percentage difference is calculated as $\left(\frac{\text{Exp}-\text{Calc}}{\text{Exp}}\right) \times 100\%$

6.4.3 Electronic Transition Results

The electronic transitions were calculated for the bidentate pyrrolide-imine gold(III) chelates using the TD-DFT method, solving for 16 excited states. The level of theory used was B3LYP/LanL2DZ. This basis set does not include the core electrons in the simulations, only valence electrons. In principle, this should not affect the accuracy of the simulations as core electrons are not usually involved in electronic transitions. The results were compared with the experimental UV/visible absorption spectra (Figure 6.4.4).

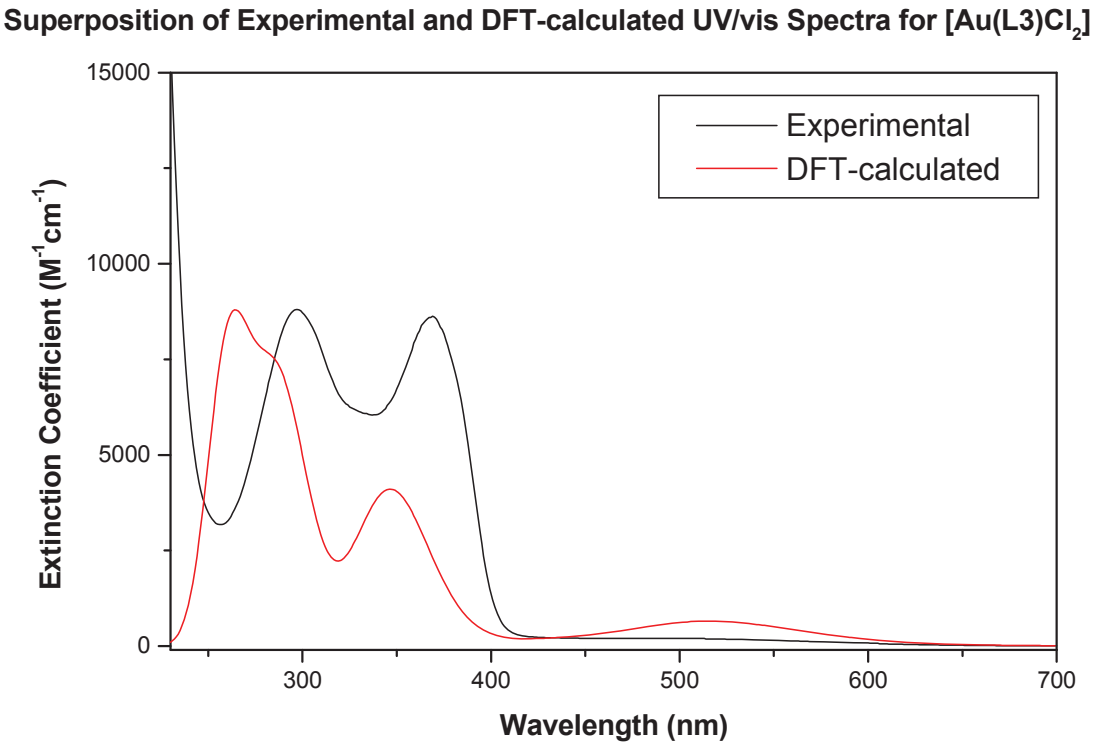

Figure 6.4.4: Superposition of experimental and DFT-calculated UV/visible spectra for [Au(L3)Cl_2]. The DFT-calculated spectrum has been scaled.

Figure 6.4.4 shows a moderate correlation between the calculated and experimental spectra; however, the energy of the transitions has been overestimated. That is, the calculated spectrum shows a hypsochromic (blue) shift relative to the experimental spectrum. The relative intensities of the transitions have been relatively poorly estimated.

The calculated spectra shown in Figure 6.4.4 is the result of multiple electronic transitions between different molecular orbitals. The orbitals that are involved in most of the transitions are shown in Figure 6.4.5, due to the other complexes having similar molecular orbitals they have not been shown here, but are available in **Appendix E.**

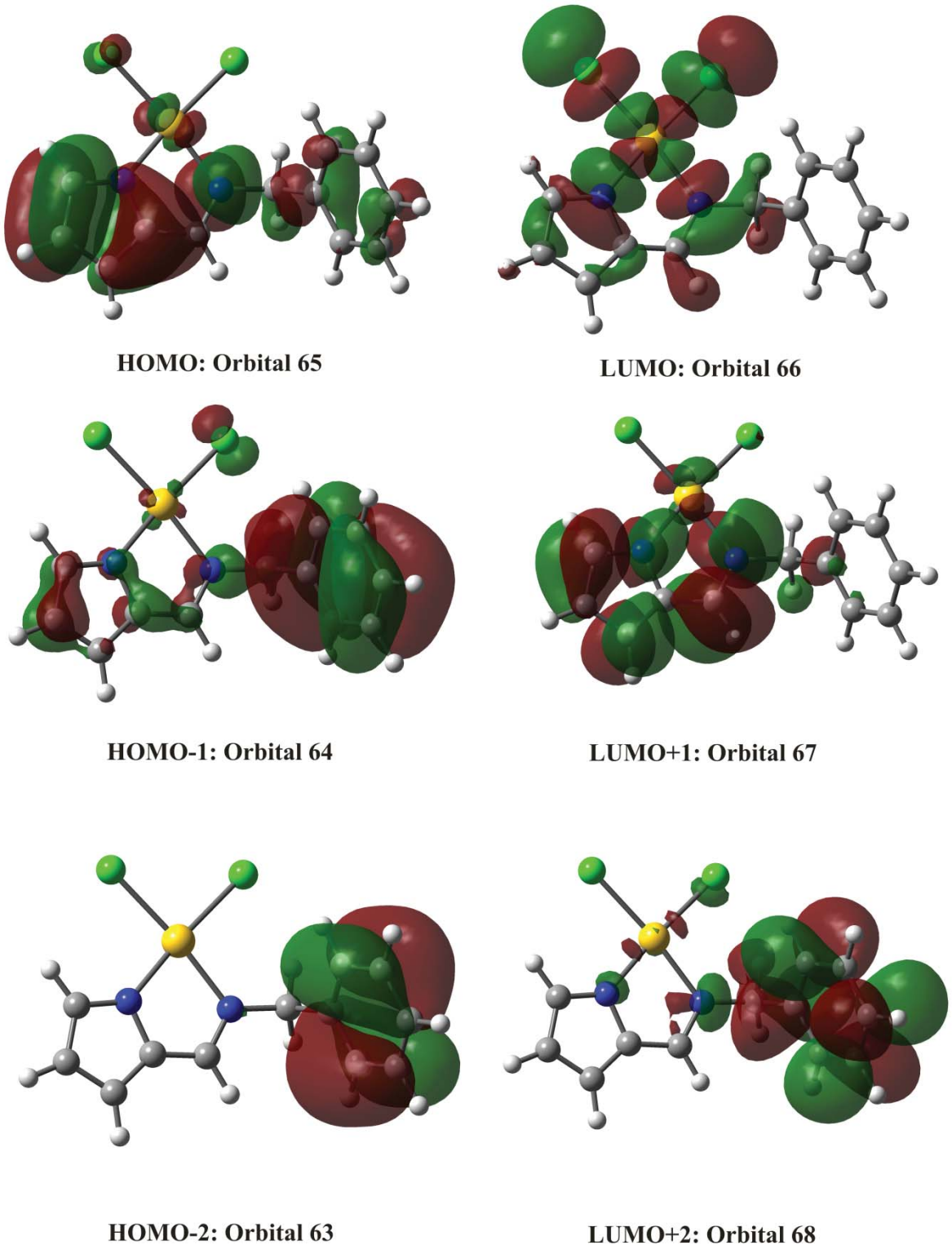

Figure 6.4.5: The electronic orbitals of [Au(L3)Cl_2] involved in the majority of the electronic transitions. The orbitals are all of π-symmetry except the LUMO orbital which is of σ-symmetry.

Figure 6.4.5 shows that the calculated HOMO orbital is of π-symmetry with the orbitals located over the pyrrole ring and imine bond. The HOMO plot also shows d_{xz} orbitals of the gold(III) ion. The LUMO plot is of σ-symmetry, with the dx^2-y^2 orbitals of the gold(III) ion mixed with the σ-orbitals of the ligand. The major electronic transitions for [Au(L3)Cl_2] are summarised in Table 6.4.3. The electronic transitions that are associated with the balance of the complexes are summarised in Table 6.4.4.

Table 6.4.3: Summary of the calculated electronic transitions for the complex [Au(L3)Cl_2] and the associated orbitals.

Wavelength(nm)	**Molecular Orbitals**	**Symmetry of Orbitals**	**Oscillator strength**
252.9	HOMO-5→LUMO+1	π→π*	0.0465
	HOMO-4→LUMO+1	π→π*	
346.9	HOMO→LUMO+1	π→π*	0.1265
	HOMO-8→LUMO	π→σ*	

The molecular orbital plots show that the orbitals are all mixed with contributions from the ligand and metal ion. This means assigning orbitals to either ligands or metals is redundant.

Table 6.4.4: Summary of calculated and experimental electronic transitions for the bidentate pyrrolide-imine gold(III) chelates and the molecular orbitals involved.

Complex	**Exp. (nm)**	**Calc. (nm)**	**Symmetry Orbitals**	**Type**	**Oscillator Strength**
$[Au(L1)Cl_2]$	294	249.52	HOMO-11→LUMO	π→π*	0.1572
	364		HOMO-8→LUMO	π→σ*	
		253.312	HOMO-9→LUMO	π→σ*	0.1483
			HOMO-8→LUMO	π→σ*	
		285.28	HOMO-1→LUMO+1	π→π*	0.1858
			HOMO-10→LUMO	π→σ*	
		342.49	HOMO→LUMO+1	π→π*	0.1118
			HOMO-10→LUMO+1	π→σ*	
$[Au(L2)Cl_2]$	224	260.93	HOMO-4→LUMO+1	π→π*	0.0004
	316		HOMO-2→LUMO+1	π→π*	
			HOMO-1→LUMO+1	π→π*	
		352.77	HOMO→LUMO+1	π→π*	0.3564
		463.95	HOMO-3→LUMO	π→σ*	
$[Au(L4)Cl_2]$	290	285.04	HOMO→LUMO+2	π→π*	0.1931
	363	288.89	HOMO-3→LUMO+1	π→π*	0.165
			HOMO→LUMO+2	π→π*	
		294.88	HOMO-3→LUMO+1	π→π*	0.0638
		344.83	HOMO-1→LUMO+1	π→π*	0.1226
$[Au(L5)Cl_2]$	292	268.62	HOMO-8→LUMO	π→σ*	0.0792
	363	345.97	HOMO-8→LUMO	π→σ*	0.1614
			HOMO→LUMO+1	π→π*	

6.4.4 Calculated NMR Spectral Data

The ^{1}H and ^{13}C NMR spectra were simulated using the GIAO method at the same level of theory (LanL2DZ/B3LYP) used for the geometry optimisation, frequency and electronic calculations.

The calculated and experimental ^{1}H NMR chemical shifts for the gold(III) chelates are summarised in Table 6.4.5. These data show that there is an over estimation of the chemical shifts in the calculations with regard to the δ, γ and β protons. The imine chemical shifts were, however, consistently overestimated when the calculated and experimental shifts were compared. The γ and β protons have a percentage difference below 5%, the δ protons all have a percentage error less than 8.5% . This shows that there is moderate concordance between the calculated and experimental chemical shifts.

A plot of calculated versus experimental ^{1}H NMR chemical shift was used to determine if a systematic relationship exists. This plot showed that there is a linear relationship between the calculated and experimental proton chemical shifts for all the gold(III) chelates, this is illustrated by the linear plot in Figure 6.4.6. The bulk of the plots are available in **Appendix E**. ^{1}H NMR chemical shifts for the calculated and experimental data are summarised in Table 6.4.5.

Table 6.4.5: Calculated and experimental ^{1}H NMR chemical shifts for the gold(III) chelates.

Gold(III) chelate		δ	γ	β	Imine
[Au(L1)Cl_2]	Exp.	7.28	6.40	7.01	8.26
	Calc.	7.88	6.68	7.17	7.97
	% Dif.	-8.24	-4.38	-2.28	3.51
[Au(L2)Cl_2]	Exp.	7.47	6.52	7.16	8.32
	Calc.	7.97	6.84	7.37	8.05
	% Dif.	-6.69	-4.91	-2.93	3.25
[Au(L3)Cl_2]	Exp.	7.35	6.43	7.08	8.37
	Calc.	7.88	6.67	7.13	8.14
	% Dif.	-7.21	-3.73	-0.71	2.75
[Au(L4)Cl_2]	Exp.	7.36	6.42	7.00	8.09
	Calc.	7.88	6.63	6.96	7.82
	% Dif.	-7.07	-3.27	0.57	3.34
[Au(L5)Cl_2]	Exp.	7.26	6.39	6.98	8.05
	Calc.	7.88	6.70	7.22	8.02
	% Dif.	-8.54	-4.85	-3.44	0.37

*Percentage difference is calculated as $\left(\frac{\text{Exp}-\text{Calc}}{\text{Exp}}\right) \times 100\%$

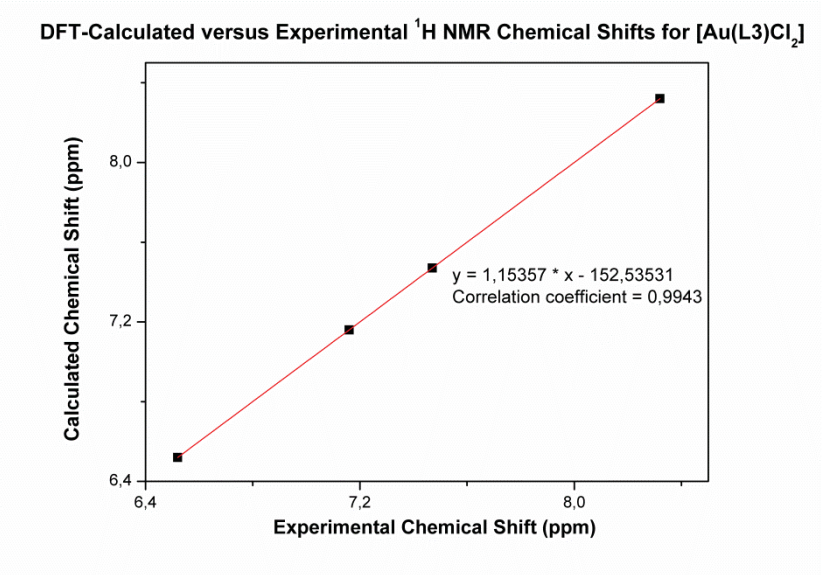

Figure 6.4.6: Linear plot of DFT-calculated and experimental ^{1}H NMR chemical shifts for $[Au(L3)Cl_2]$.

The ^{13}C NMR chemical shifts for the calculated data were all underestimated relative to the experimental data. The δ carbon was the most accurately estimated with an average error less than 3.5%. The chemical shifts of the remaining carbon atoms were less accurately estimated with errors ranging from 4-10%. The ^{13}C NMR shifts of the calculated and experimental data are summarised in Table 6.4.6 along with their percentage differences for the gold(III) chelates. The ^{13}C and ^{1}H NMR chemical shifts of the calculated spectra were in moderately good agreement to that of the experimental chemical shifts (Table 6.4.5 and 6.4.6). This shows that the basis set Lan2DZ was effective for these calculations.

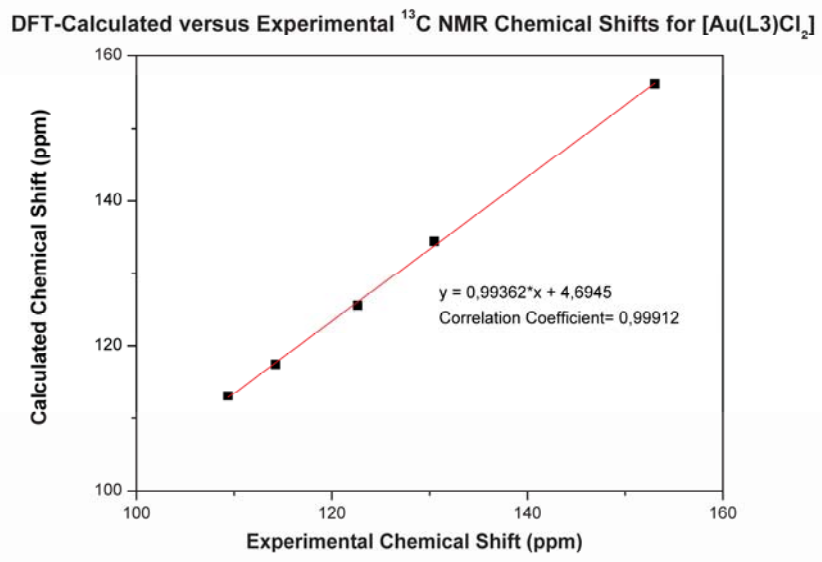

Figure 6.4.7: Linear plot of DFT-calculated and experimental ^{13}C NMR chemical shifts for $[Au(L3)Cl_2]$.

Table 6.4.6: Calculated and experimental ^{13}C NMR chemical shifts for the gold(III) chelates.

Proton		δ	γ	β	α	Imine
	Exp.	134.44	110.98	122.24	135.07	165.23
$[Au(L1)Cl_2]$	Calc.	131.49	103.06	116.78	124.18	156.22
	% Dif.	2.19	7.14	4.47	8.06	5.45
	Exp.	137.24	112.55	124.35	136.57	164.63
$[Au(L2)Cl_2]$	Calc.	132.84	105.46	118.96	125.49	154.50
	% Dif.	3.21	6.30	4.33	8.11	6.15
	Exp.	136.74	111.52	129.30	137.16	165.86
$[Au(L3)Cl_2]$	Calc.	131.95	103.82	117.54	125.37	157.70
	% Dif.	3.50	6.90	9.10	8.60	4.92
	Exp.	136.63	111.44	123.63	129.16	165.02
$[Au(L4)Cl_2]$	Calc.	131.86	103.40	117.15	124.67	155.75
	% Dif.	3.49	7.21	5.24	3.48	5.62
	Exp.	136.42	111.15	122.48	138.18	165.16
$[Au(L5)Cl_2]$	Calc.	131.78	103.35	117.27	124.26	156.69
	% Dif.	3.40	7.02	4.25	10.07	5.13

*Percentage difference is calculated as $\left(\frac{\text{Exp}-\text{Calc}}{\text{Exp}}\right) \times 100\%$

6.5 Conclusions

Density functional theory (DFT) simulations were used to calculate various characteristics of the free ligands and gold(III) chelates. The simulated and experimental data were then compared. This is a key aspect in order to fully understand observed experimental data.

Overall, there was good agreement between the experimental X-ray and simulated structures, as indicated by the low RMSDs of the experimental and calculated structures. There was slight deviation in the torsion angles of the functional groups this was due to steric repulsion between molecules not being taken into account.

The hydrogen bonding in the solid state could be explained in terms of electrostatics using the NBO charges with the imine nitrogen being the most electronegative and the pyrrole NH the most electropositive. It can be concluded that this hydrogen bonding motif is highly reliable based on electrostatic arguments.

The vibrational frequencies and experimental IR spectra showed good agreement. However, in the calculated spectra the frequencies were overestimated for the higher energy vibrations and underestimated for the lower energy vibrations in comparison to the experimental data.

The ligand electronic spectra were very accurately estimated, but the absorption spectra of the gold(III) chelates were blue shifted relative to the experimental data. The absorption bands were the result of transitions between several orbitals, most of which were of π-symmetry.

The ^{1}H and ^{13}C NMR data were calculated for the free ligands and gold(III) complexes. The simulated data were moderately accurate. The ^{1}H NMR chemical shifts were both over and underestimated relative to the experimental data and thus no correction factor could be determined to improve the accuracy of the results. The errors in the ^{13}C NMR chemical shifts were more consistent and a correction factor could be calculated.

In general, the DFT-calculated parameters for the ligands were more accurate than those of the gold(III) chelates. This is expected since the basis set used for the ligands (6-311G) is substantially larger than that used for the gold(III) chelates (LanL2DZ). In future work, a split basis set which applies the 6-311G(dp) basis set to the light atoms and the LanL2DZ basis set to the gold(III) ion only could improve the accuracy of the calculated parameters.

Chapter Seven: Biological Studies

7.1 Introduction

There has been growing interest in gold and its compounds with regard to their cytotoxicity towards human tumour cell lines.[10] One of the more important future applications of gold is in the development of anti-cancer DNA intercalator drugs. The square planar geometry of the gold(III) ion allows for effective intercalation as well as Au···π interactions with the aromatic DNA base pairs of the double helix. In order to treat various cancers there are three methods that can be used: 1) surgery, 2) radiotherapy and 3) drug therapy.[1] With these three treatments it has been possible to cure approximately half of those diagnosed with cancer and the other fifty percent have experienced prolonged survival. Of the three methods, drug therapy is the one that requires most improvement;[1] many of the drugs currently in commercial use are effective, but have severe side-effects and therefore require further development. Since chemotherapy can be developed in a step-by-step approach it is a popular area of pharmaceutical research.

The cytotoxicity of a potential chemotherapeutic agent towards various cancer cell lines is measured by several growth inhibition parameters. Illustrated below in Figure 7.1.1 is the dose response curve for a bis(pyrrolide-imine) gold(III) chelate. To determine the cytotoxicity of a new compound, a particular tumour cell line is inoculated with several concentrations of the drug candidate and the change in growth rate as a function of concentration is analysed. From this experiment, three different growth parameters can be determined. Firstly, the GI_{50} value which is the concentration of a compound at which there is 50% growth inhibition this corresponds to a 25% cell kill rate. Secondly, the concentration where there is no overall cell growth, a 50% cell kill (IC_{50}) and finally, the concentration of the compound that causes a negative 50% cell growth rate (75% cell kill), this is the LC_{50} value. The main advantage of screening several potential drug candidates against different human cancer cell lines is that it shows which attributes have the greatest effect on the cytotoxicity and these can be further developed.

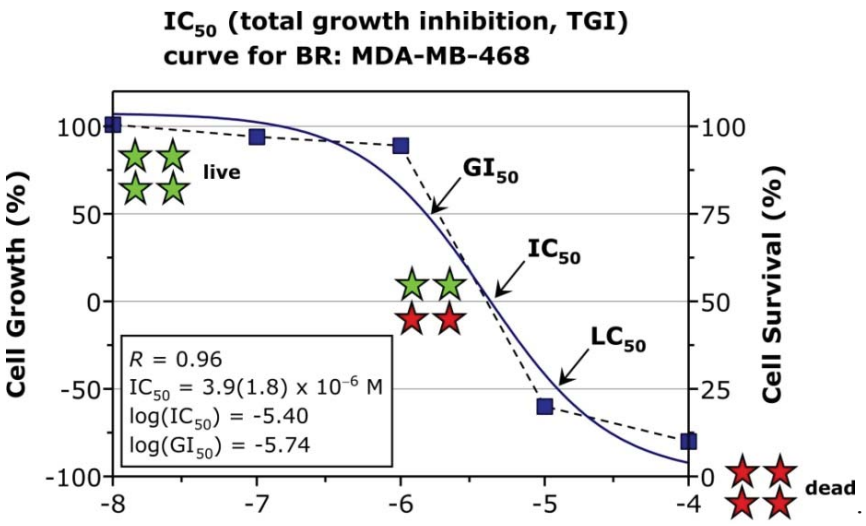

Figure 7.1.1: Illustration of various cell growth rate parameters for a bis(pyrrolide-imine) gold(III) chelate.

7.2 Experimental

The assay's endpoint was determined via the CellTiter Aqueous Non-Radioactive Assay (Promega Corporation, Madison, Wisconsin, USA). A 96-well microtiter plate was seeded with cells at a low passage number, at a concentration of 2×10^5 cells mL^{-1} in a total volume of 100 µL complete medium (TK-10, A549, U251 and HT-29). The media contained 10% foetal bovine serum (FBS, Highveld Biological, R.S.A.) and necessary antibiotics. After an incubation period of 24 hours at 37 °C and 5% CO_2, the test compounds were added in two-fold serial dilutions for a total of seven concentrations (50 – 0.78 µM). After an incubation period of 96 hours, 10 µL $well^{-1}$ of the CellTiter solution was added; the contents gently mixed and the plates incubated under the previously described conditions. The plates were read at time intervals of 2 and 4 hours at an absorbance wavelength of 490 nm on a multiplate reader (xMarkTM, Bio-Rad). IC_{50} values were determined as the concentration of the test substance required to reduce cell viability by 50% using OriginPro® version 8.0.[94] The cell screening was performed at Mintek, South Africa.

7.3 Results and Discussion

In this work, five gold(III) chelates were screened against a panel of four human tumour cell lines by Mintek. These cell lines represent non-small cell lung carcinoma (A549), central nervous system cancer (U251), human colon adenocarcinoma (HT29) and human renal adenocarcinoma (TK-10) cancers. This panel of human tumour cell lines covers a cross section of the many human tumour variants. The activity of the chelates against this panel of cell lines is given as the –log IC_{50} value. The IC_{50} value represents the concentration of the complex required to terminate 50% of the tumour cells, resulting in zero overall growth rate. In general, the lower the IC_{50} value (measured in mol dm^{-3}) the more cytotoxic a compound is towards a particular tumour cell line.

Figure 7.1.2 shows that $[Au(L3)Cl_2]$ has the highest activity of the five gold(III) chelates, showing particular activity towards non-small cell lung carcinoma (A549) and central nervous system cancer (U251). Complexes $[Au(L4)Cl_2]$ and $[Au(L5)Cl_2]$ have the highest activity towards human renal adenocarcinoma (TK-10). However, when looking at the mean values for all five gold(III) chelates it is noted that the activity is very similar across the four cancer cell lines.

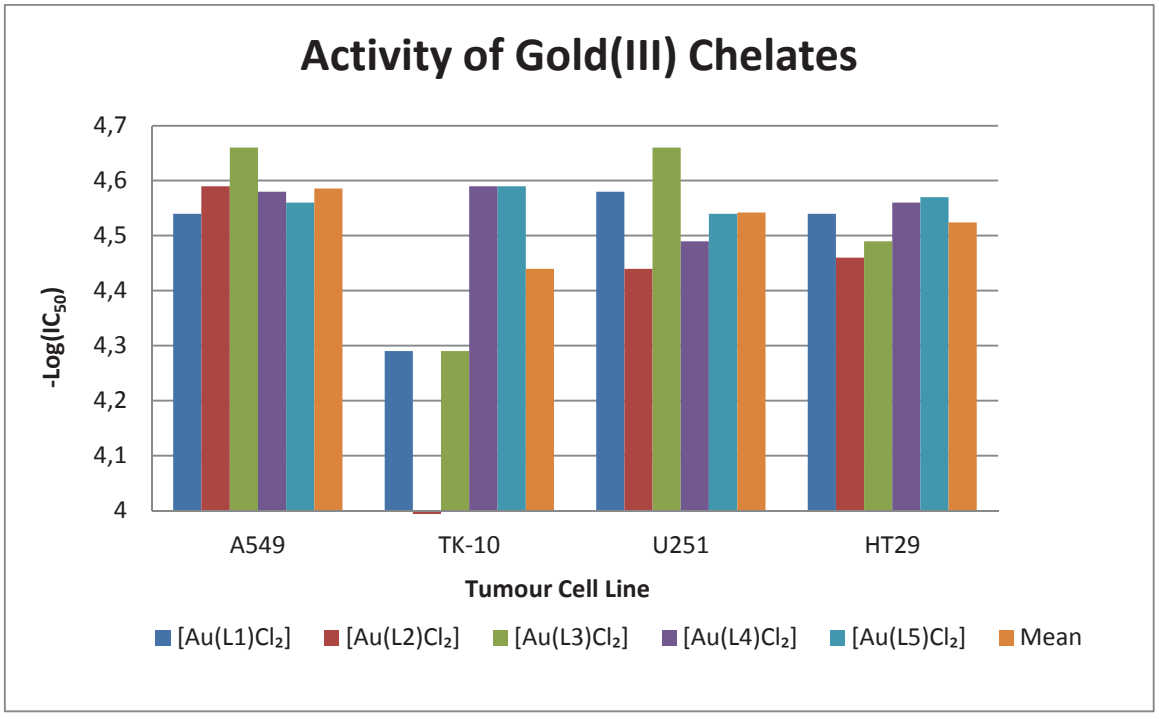

Figure 7.1.2: Comparison of -log(IC_{50}) values of the five gold(III) chelates and mean values.

Since the efficacy of the chelate is given as the –log IC_{50} value as opposed to the concentration of the chelate in μM a larger value represents a greater activity of the chelate against that cell line. The plot in Figure 7.1.2 therefore clearly shows that the five gold(III) chelates are more active against non-small cell lung cancers (A549). $[Au(L1)Cl_2]$, $[Au(L2)Cl_2]$ and $[Au(L3)Cl_2]$ are considerably less active against renal cancer (TK-10). This varying efficacy against different tumour cell lines is an encouraging result as it suggests that the compound is not only a poison, but a moderately effective chemotherapeutic agent with a well defined mechanism of action. With the exception of TK-10 all of the compounds have very similar activities; well within the standard deviation of the measured values. This implies that the structural variation of the chelates has little impact on the cytotoxicity. There are two possible reasons for this: firstly, the drugs may not be acting as DNA intercalators, but rather DNA cross-linkers and then the extent of aromaticity will have little influence on the cytotoxicity. Secondly, the stability of the compound in a cellular environment has not been determined. It is possible that the compounds are being reduced and the resulting gold colloids are in fact responsible for the cytotoxicity. The mean -log IC_{50} for the four cell lines for $[Au(L1)Cl_2]$, $[Au(L2)Cl_2]$, $[Au(L3)Cl_2]$, $[Au(L4)Cl_2]$ and $[Au(L5)Cl_2]$ are: 4.48, 4.49, 4.52, 4.55 and 4.57, respectively. These compare favourably to that of cisplatin, which is 5.21 against the National Cancer Institute's panel of 60 human cancer cell lines (Table 7.1.1). Considering that cisplatin is still one of the most widely used chemotherapeutic agents, particularly for the treatment of testicular as well as head and neck cancers, these data show that the pyrrolide-imine gold(III) chelates in this work could well find application in the future treatment of cancer once further testing has been preformed.

A comparison of the cytotoxicity of the five gold(III) chelates with other commercially available chemotherapeutic agents (cisplatin, carboplatin and bleomycin) is shown in Figure 7.1.3. This comparison shows that against specific cancer cell lines the gold(III) chelates synthesised in this work have poor activity towards the four cancer cell lines compared to the commercial chemotherapeutic agents. Specifically, these compounds are less cytotoxic compared to the high activity drugs, such as bleomycin and cisplatin. All five chelates do, however, have a higher activity than carboplatin.

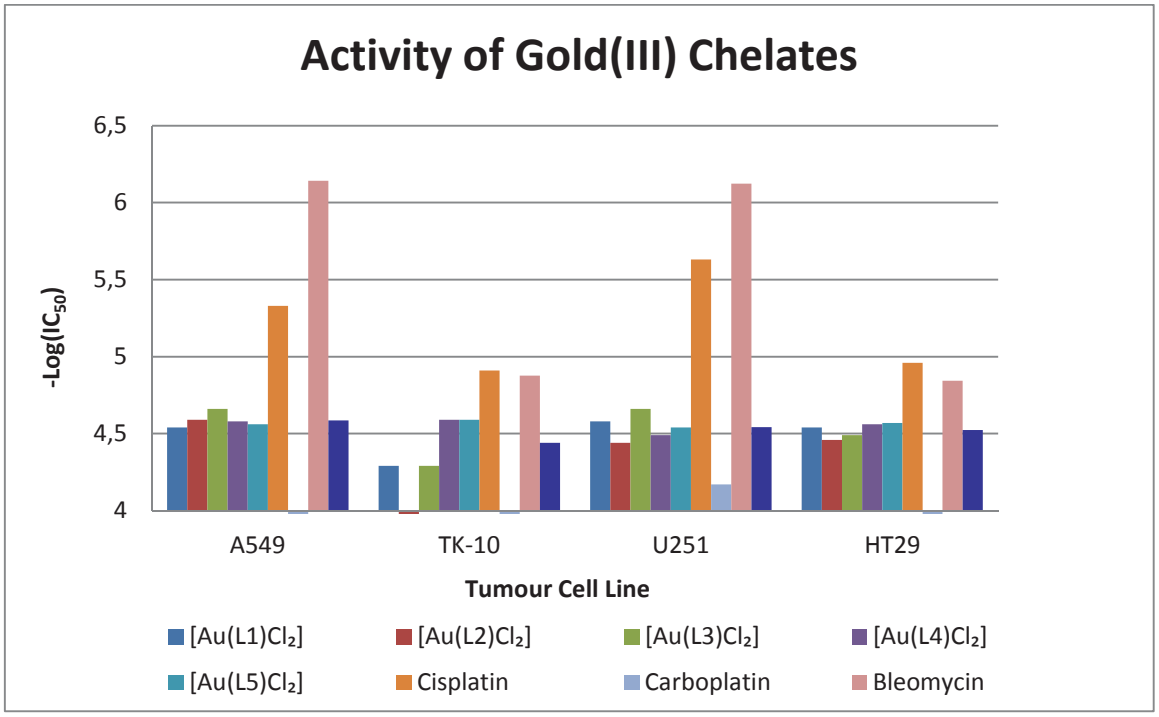

Figure 7.1.3: Comparison of -log(IC_{50}) values of the gold(III) chelates with commercially available chemotherapeutic agents for specific human cancer cell lines.

It seems that a longer chain length with increased aromaticity increases the activity towards certain cancer cell lines, specifically human renal adenocarcinoma (TK-10). The five gold(III) chelates have a very similar cytotoxicity level, therefore we assume that the method of DNA binding is in fact not intercalation, as the compounds would each have differing intercalation abilities, but potentially DNA crosslinking. Other commercially available chemotherapeutics that are DNA cross-linkers, such as cisplatin, show comparable activity towards the four cancer cell lines.[95] The data in Table 7.1.1 shows that the five gold(III) chelates have poor activities towards the four cancer cell lines when compared to bleomycin and cisplatin but they do have a greater activity than carboplatin which has a very low activity towards all off tested cancer cell lines. This is a commercially available chemotherapeutic which targets ovarian cancer. Therefore there is potential for the gold(III) chelates to have a higher activity towards other cancer cell lines, such as ovarian cancers, that were not tested in this work.

Table 7.1.1: Comparison of -log(IC_{50}) values for the four cancer cell lines screened for the gold(III) chelates and current chemotherapeutic agents.

	A549	**TK-10**	**U251**	**HT29**
[Au(L1)Cl_2]	4.54	4.29	4.58	4.54
[Au(L2)Cl_2]	4.59	> 4.30	4.44	4.46
[Au(L3)Cl_2]	4.66	4.29	4.66	4.49
[Au(L4)Cl_2]	4.58	4.59	4.49	4.56
[Au(L5)Cl_2]	4.56	4.59	4.54	4.57
Cisplatin	5.33	4.91	5.63	4.96
Carboplatin	3.95	3.60	4.17	3.60
Bleomycin	6.14	4.88	6.12	4.84

A direct comparison of the cytotoxicity of the bidentate gold(III) chelates with other previously studied gold(III) chelates was not possible as the cell lines reported in literature are different to those tested in this work. However, looking at the work of Wilson *et al.* the gold(III) chelates compare favourably to the compounds in this work with an average IC_{50} value of 23(11) μM from 60 cancer cell lines tested.[18] This corresponds to a -log(IC_{50}) value of 4.64, which compares favourably with the mean -log(IC_{50}) value in this work of 4.52. A similar bidentate *cis*-chloride chelate reported by Ronconi *et al.,*[9] Figure 7.1.4, showed similar properties to those reported by Wilson *et al*. In other work using dichloro gold(III) chelates it was shown that [Au(phen)Cl_2]Cl had potential against ovarian carcinoma with a -log(IC_{50}) value of 3.8.[21]

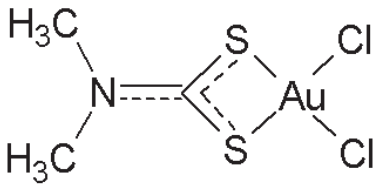

Figure 7.1.4: Structure of *cis*-dichloro gold(III) dithiocarbamates.[9]

Although the cytotoxicity of the gold(III) chelates in this work are modest this does not mean that the compounds are not potential chemotherapeutics. As the cytotoxicity is not the only factor that determines the success of a drug. It has been noted that compounds with a greater cytotoxicity often have severe side-effects. Drug design is a fine balance between cytotoxicity and side effects. For example duanorubicin is far more cytotoxic than carboplatin and yet both are used in the treatment of cancer. The ultra-high activity of duanorubicin has been known to induce secondary cancers due to its toxicity. In future work, the uptake of the gold(III) chelates in healthy versus neoplastic tissue must also be measured as this is a key factor in the success of a drug candidate.

Chapter Eight: Conclusions and Future Work

8.1 Conclusions

Five pyrrolide-imine Schiff base ligands were synthesised in this work; two of which were novel compounds. The ligands comprised a pyrrole ring joined via an imine linkage to an alkyl (HL1) or aromatic unit (HL2 - HL5). Each ligand had variable chain lengths and varying aromatic ring structures. The ligands were designed to be strong σ-donor ligands to stabilise the gold(III) ion. Coordination of the ligand to the gold(III) ion required deprotonation of the pyrrole NH yielding a bidentate, monoanionic ligand. The chelation of the bidentate *N*-donor ligand and *cis*-chloride ligands resulted in gold(III) chelates with a square planar coordination geometry and an overall neutral charge. Chelation to the gold(III) ion was only successful when $[Bu_4N][AuCl_4]$ was used as the source of the gold(III) ion in the presence of a two-fold excess of ligand. The structures of the gold(III) chelates synthesised in this work are shown in Figure 8.1.1.

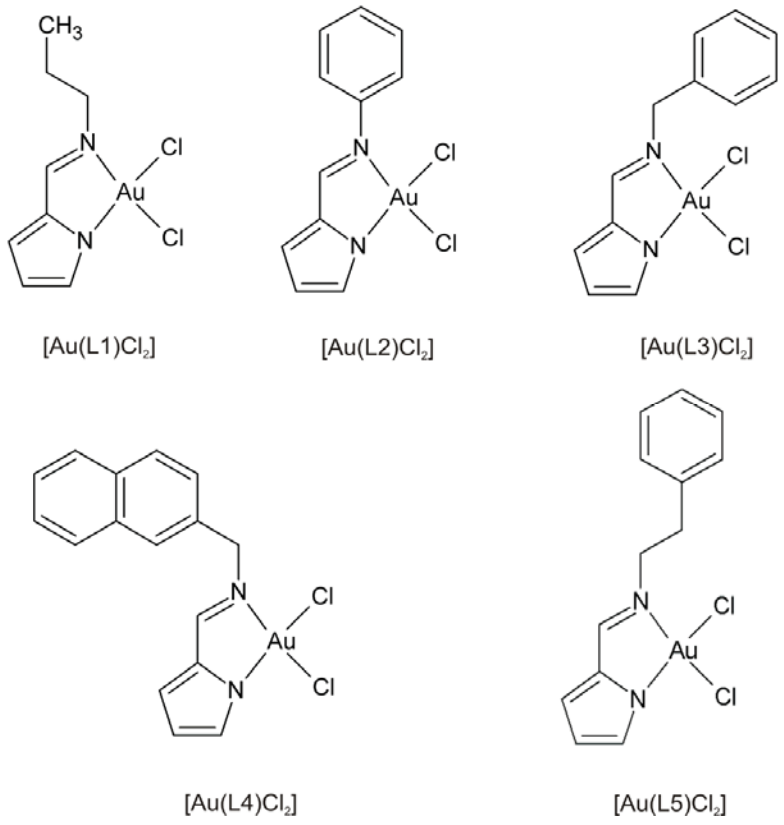

Figure 8.1.1: Structures of the bidentate pyrrolide-imine gold(III) chelates synthesised in this work.

Using spectroscopic methods such as NMR (^{1}H, ^{13}C, cosy, nosy, dept, hmbc and hmqc, where applicable), FTIR and UV-visible as well as mass spectrometry the free ligands and gold(III) chelates were fully characterised. The ^{1}H and ^{13}C NMR spectra of the chelates both showed a downfield shift in the signals when compared to the free ligand spectra. This was the result of the highly polarising and deshielding effect of the gold(III) ion. UV-visible spectroscopy showed a $\pi \rightarrow \pi^*$ band was present in the free ligands as well as in the gold(III) chelates, the gold(III) chelates also had an LMCT band at longer wavelengths.

The solid-state structures of four ligands and all five gold(III) chelates were elucidated using single crystal X-ray diffraction. These studies showed that the ligands formed stable hydrogen-bonded dimers in the solid state. These supramolecular structures were all supported by the same hydrogen bonding motif, consisting an imine nitrogen atom and pyrrole NH hydrogen atom, which act as hydrogen bond acceptors and donors, respectively.

The gold(III) ions of the chelates all exhibit a nominally square planar coordination geometry, this is consistent with the d^8 electronic configuration of the metal ion. The deprotonation of the pyrrole NH resulted in a monoanionic *N*-donor ligand. The average Au-N_{imine} bond length was 2.037(3) Å this was consistently longer than the Au-$N_{pyrrole}$ bond length which averaged 1.983(3) Å this difference was attributed to the stronger bond formed between the gold(III) ion and anionic pyrrole ring. The gold(III) chelate structure deviated slightly from the ideal square planar geometry with an acute bond angle of 82° (N1-Au-N2) this bond angle was constrained by the small bite angle of the ligand. The structures all exhibited Au$\cdots\pi$ interactions, this confirms the electrophilic nature of the gold(III) ion and suggests that the chelates are predisposed to forming favourable interactions with the aromatic DNA base pairs.

The Density Functional Theory (DFT) method was used to calculate various properties of the free ligands and gold(III) chelates. The experimental data and theoretical data were compared to determine the effectiveness of the basis set and hybrid functional used. The simulations were also used to better understand the experimental phenomena that were observed in this work. The level of theory used in the DFT simulations was B3PLYP/6-311G(dp) for the free ligands and B3PLYP/LanL2DZ for the gold(III) chelates. The geometry optimised structures as well as the NMR, vibrational and electronic spectra were calculated. The vibrational frequencies of both the gold(III) chelates and metal-free ligands both showed no negative Eigen values. This indicates that a true minimum on the potential energy surface was reached and the geometry optimised structure was likely the lowest energy conformation. Comparing the experimental and calculated frequency data showed an overall overestimation at higher frequencies and an underestimation at lower frequencies. Despite this inaccuracy, the data showed that the relative intensities of the bands were estimated correctly with good parity to the experimental data.

The geometry optimised structures of the monomeric ligands as well as the hydrogen-bonded dimer structures were calculated. The simulations showed that the ligands underwent a degree of conformational distortion from the lowest energy structures to allow for optimal hydrogen bonding. The NBO partial charges showed that the imine nitrogen atom and pyrrole NH hydrogen atom were always the most electronegative and electropositive atoms in the ligand structures, respectively. These partial charges suggest that in simple electrostatic terms the formation of hydrogen bonds between these two groups is the most favourable.

The geometry optimisation of the gold(III) chelates showed good agreement with the experimental data. The geometry of the coordination sphere was accurately predicted, the main deviation between the experimental and calculated structures was in the aromatic appendages. The mean calculated bond lengths and angles are as follows (percentage difference between the calculated and experimental structures are given in parentheses) Au-N_{imine} = 2.095 Å [-1.86%] and Au-$N_{pyrrole}$ = 2.025 Å [1.72%]. However, the mean bond angles were more accurately calculated with a value of 80.32° [0.72%], this small percentage error shows that the computational method was reliable.

The simulated electronic spectra showed a shift to shorter wavelength of the $\pi \rightarrow \pi^*$ and MLCT bands for the gold(III) chelates. The ^{1}H and ^{13}C NMR data were both calculated for the gold(III) chelates and metal free ligands. Overall there was a shift of ^{1}H NMR peaks downfield compared to the experimental data, but in the ^{13}C NMR there was an upfield shift of the spectrum. In general, the simulated data compared favourably to the experimental data showing that the level of theory used for the gold(III) chelates and free ligands was appropriate.

The gold(III) chelates were screened by Mintek for cytotoxicity against four human tumour cell lines; these cell lines represent non-small cell lung carcinoma (A549), central nervous system cancer (U251), human colon adenocarcinoma (HT29) and human renal adenocarcinoma (TK-10) cancers. Overall, it was shown that the gold(III) chelates in this work have modest chemotherapeutic activity against these four cancer cell lines. [Au(L3)Cl_2] was shown to have the highest activity of the five gold(III) chelates. The cytotoxicity of all the chelates was relatively similar, suggesting that the aromatic appendages play little role in the anti-tumour activity. This could imply that they are DNA cross-linking agents, since all the compounds would have a similar propensity for cross-linking their activities would all be similar.

8.2 Future Work

The main objectives of this research project were to successfully synthesise and characterise a range of pyrrolide-imine gold(III) chelates. On completion of this, their potential application as chemotherapeutic agents could be explored. These primary objectives have been achieved; however, during the course of this work several other factors that require further investigation have been identified.

Throughout this work it would appear that the gold(III) chelates did not intercalate the DNA, but possibly interact via cross-linking. This theory needs to be investigated to determine the actual mode of interaction with DNA. If the drugs are DNA cross-linking agents they may well have a different cytotoxicity profile to that expected for DNA intercalators. It would therefore be prudent to screen the drugs against a wider panel of cell lines to determine whether there is any specificity for particular cell lines.

The synthesised gold(III) chelates all exhibited very poor aqueous solubility. This is believed to be due to the lack of an overall positive charge. Therefore, the ligand could be altered to contain a pyridine ring instead of a pyrrole ring.[19, 37, 51, 96] This will give gold(III) chelates with an overall positive charge.[19] This will have a dual effect. Firstly, it will increase the aqueous solubility of the chelates and secondly, it may potentially increase the electrostatic interactions of the compounds with the negatively charged phosphate backbone of DNA. The pyridine ring will also increase the aromaticity of the chelates increasing its ability to intercalate between DNA base pairs.[19] Below is an example of the proposed second generation of gold(III) chelates (Figure 8.1.2).

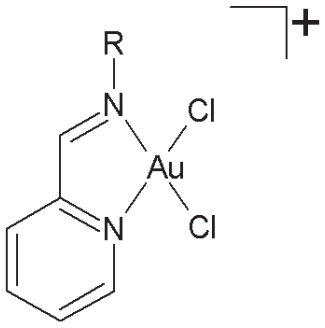

Figure 8.1.2: Structure of the pyridine-imine gold(III) chelate proposed for future work.

The range of R groups could also be expanded to include biotin and longer chain lengths. There is an over expression of biotin receptors in cancer tissues thus attaching biotin (also known as vitamin H) may potentially increase the uptake of the gold(III) chelates into neoplastic as opposed to healthy tissue.[2, 97-99] Since biotin does not have a primary amine suitable to form an imine bond, a new ligand design would be required. The biotin could be tagged onto an amine group, forming an amide bond such as the structure proposed below.

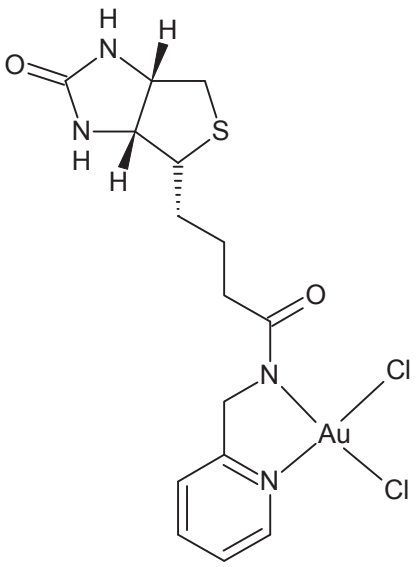

Figure 8.1.3: Structure of the proposed gold(III) chelate with a biotin cell-targeting appendage.

In the current work, an increase in chain length and aromaticity lead to an increase in activity towards the cancer cell lines and therefore needs to be explored in greater depth.

The chelates may also be susceptible to reduction; this would limit their cytotoxicity as the synthesised compound may not be reaching the intended cellular target. The stability of the compounds in a cellular environment should also therefore be explored. Pending the outcome of this, the stability of the chelates may need to be improved by replacing the chloride ligands with stronger σ-donor groups which would better stabilise the chelates.

References

Uncategorized References

[1] I. Kostova, *Anti-Cancer Agents Med. Chem.* (2006), ***6***, 19-32.
[2] V. Milacic and Q.P. Dou, *Coord. Chem. Rev.* (2009), ***253***, 1649-1660.
[3] F. Ullah, T. Kang, E.J. Yoon, E.C. Choi, S. Kim and J. Lee, *Eur. J. Med. Chem.* (2009), ***44***, 239-250.
[4] O.Q. Munro and G.L. Camp, *Acta Crystallogr., Sect. C: Cryst. Struct. Commun.* (2003), ***C59***, 0672-0675.
[5] R.W.Y. Sun and C.-M. Che, *Coord. Chem. Rev.* (2009), ***253***, 1682-1691.
[6] H.E. Abdoua, A.A. Mohameda, J.P. Fackler, A. Burinib, R. Galassib, J.M. López-De-Luzuriagac and M.E. Olmosc, *Coord. Chem. Rev.* (2009), ***253***, 1661-1669.
[7] E.R.T. Tiekink, *Inflammopharmacology* (2008), ***16***, 138-142.
[8] P. Calamai, S. Carotti, A. Guerri, L. Messori, E. Mini, P. Orioli and G. Paolo Speroni, *J. Inorg. Biochem.* (1997), ***66***, 103-109.
[9] L. Ronconi, C. Marzano, P. Zanello, M. Corsini, G. Miolo, C. Maccà, A. Trevisan and D. Fregona, *J. Med. Chem.* (2006), ***49***, 1648-1657.
[10] C. Che, R.W. Sun, W. Yu, C. Ko, N. Zhu and H. Sun, *Chem. commun.* (2003), ***14***, 1718-1719.
[11] O.Q. Munro, S.D. Strydom and C.D. Grimmer, *New J. Chem.* (2004), ***28***, 34-42.
[12] D.E. Thurston, *Chemistry and pharmacology of anticancer drugs*. CRC press: London, 2007.
[13] G.K. Podila, *Nucleic acid detection and Analysis*. 2010; Vol. 11, p 269.
[14] A.D. Richards and A. Rodger, *Chem. Soc. Rev.* (2007), ***36***, 471 – 483.
[15] T. Phillips, I. Haq, A.J.H.M. Meijer, H. Adams, I. Soutar, L. Swanson, M.J. Sykes and J.A. Thomas, *Biochem.* (2004), ***43***, 13657-13665.
[16] A. Bindolia, M.P. Rigobello, G. Scutarib, C. Gabbianic, A. Casinid and L. Messoric, *Coord. Chem. Rev.* (2009), ***253***, 1692-1707.
[17] Y. Wang, Q.-Y. He, R.W.-Y. Sun, C.-M. Che and J.-F. Chiu, *Eur. J. Pharmacol.* (2007), ***554***, 113-122.
[18] C.R. Wilson, A.M. Fagenson, W. Ruangpradit, M.T. Muller and O.Q. Munro, *Inorg. Chem.* (2013), ***52***, 7889−7906.
[19] S. Schouteeten, O.R. Allen, A.D. Haley, G.L. Ong, G.D. Jones and D.A. Vicic, *J. Organomet. Chem.* (2006), ***691***, 4975-4981.
[20] P. Shi, Q. Jiang, Y. Zhao, Y. Zhang, J. Lin, L. Lin, J. Ding and Z. Guo, *J. Biol. Inorg. Chem.* (2006), ***11***, 745-752.
[21] L. Messori, F. Abbate, G. Marcon, P. Orioli, M. Fontani, E. Mini, T. Mazzei, S. Carotti, T. O'connell and P. Zanello, *J. Med. Chem.* (2000), ***43***, 3541-3548.
[22] B. Lippert, *Chemistry and Biochemistry of a Leading Anticancer Drug*. 1st ed.; Wiley-VCH: Republic of Germany 1995.
[23] Y. Pommier, J.K. Minford, R.E. Schwartz, L.A. Zwelling and K.W. Kohn, *Biochem.* (1985), ***24***, 6410-6416.
[24] A.L.F. Chan, W.S. Chang, L.M. Chen, C.M. Lee, C.E. Chen, C.M. Lin and J.L. Hwang, *Molecules* (2009), ***14***, 1342-1352.
[25] J. Li, J. Hu, Y. Gu, F. Mei, T. Li and G. Li, *J. Mol. Catal. A: Chem.* (2011), ***340***, 53-59.
[26] A. Bacchi, M. Carcelli, L. Gabba, S. Ianelli, P. Pelagatti, G. Pelizzi and D. Rogolino, *Inorg. Chim. Acta* (2003), ***342***, 229-235.
[27] S. Akmal, A. Gaball, S. Mohsen, B. Asker, S. Atiat, C. Barakat, M. Said and C. Teleb, *Spectrochim. Acta, Part A* (2007), ***67***, 114–121.

[28] C.D. Meyer, C.S. Joiner and J.F. Stoddart, *Chem. Soc. Rev.* (2007), ***36***, 1705-1723.
[29] N. Shahabadi, S. Kashanian and F. Darabi, *Eur. J. Med. Chem.* (2010), ***45***, 4239-4245.
[30] K.Heinze, G.Marano and A.Fischer, *J. Inorg. Biochem.* (2008), ***102***, 1199.
[31] C.S.B. Gomes, D. Suresh, P.T. Gomes, L.F. Veiros, M.T. Duarte, T.G. Nunes and M.C. Oliveira, *Dalton Trans.* (2010), ***39***, 736-748.
[32] M.P. Akerman and V.A. Chiazzari, *J. Mol. Struct.* (2014), ***1058***, 22-30.
[33] S.S. Gunatilleke and A.M. Barrios, *J. Med. Chem.* (2006), ***49***, 3933-3937.
[34] O.Q. Munro, K.J. Akerman and P. Akerman Gold complexes. International Patent WO 2011/158176 A2, Jun 14, 2011.
[35] I. Ott, *Coord. Chem. Rev.* (2009), ***253***, 1670-1681.
[36] G. Marcon, S. Carotti, M. Coronnello, L. Messori, E. Mini, P. Orioli, T. Mazzei, M.A. Cinellu and G. Minghetti, *J. Med. Chem.* (2002), ***45***, 1672-1677.
[37] T.V. Segapelo, I.A. Guzei, L.C. Spencer, W.E.V. Zyl and J. Darkwa, *Inorg. Chim. Acta* (2009), ***362***, 3314-3324.
[38] P.-F. Shi and Q. Jiang, *Acta Crystallogr.* (2006), ***E62***, m1183-m1185.
[39] M. Navarro, *Coord. Chem. Rev.* (2009), ***253***, 1619-1626.
[40] D. Aguilar, M. Contel, R. Navarro, T. Soler and E.P. Urriolabeitia, *J. Organomet. Chem.* (2009), ***694***, 486-493.
[41] M. Suwalskya, R. González, F. Villena, L.F. Aguilar, C.P. Sotomayor, S. Bolognin and A. Zatta, *Coord. Chem. Rev.* (2009), ***253***, 1599-1606.
[42] P.J. Barnard and S.J. Berners-Price, *Coord. Chem. Rev.* (2007), ***251***, 1889-1902.
[43] C.S.B. Gomes, C.A. Figueira, P.S. Lopes, D. Suresh, P.T. Gomes and M.T. Duarte, *Acta Crystallogr., Sect. C: Cryst. Struct. Commun.* (2011), ***67***, o315-o318.
[44] M. Lin, W. Liu, Z. Chen, L. Yang, H. Pei, J. Wu, X. Wan, T. Lei and Y. Li, *RSC Adv.* (2012), ***2***, 3451-3457.
[45] T. Yasumoto, T. Yamagata and K. Mashima, *Organometallics* (2005), ***24***, 3375-3377.
[46] Biospin*Bruker Topspin 2.1*, pl6.
[47] P.G. Cozzi, *Chem. Soc. Rev.* (2004), ***33***, 410-421.
[48] T.R.V.D. Ancker, G.W.V. Cave and C.L. Raston, *Green Chem.* (2006), ***8***, 50-53.
[49] O.Q. Munro, S.D. Joubert and C.D. Grimmer, *Chem. Eur. J.* (2006), ***12***, 7987-7999.
[50] D. Sinha, A.K. Tiwari, S. Singh, G. Shukla, P. Mishra, H. Chandra and A.K. Mishra, *Eur. J. Med. Chem.* (2008), ***43***, 160-165.
[51] M. Serratrice, M.A. Cinellu, L. Maiore, M. Pilo, A. Zucca, C. Gabbiani, A. Guerri, I. Landini, S. Nobili, E. Mini and L. Messori, *Inorg. Chem.* (2012), ***51***, 3161-3171.
[52] A. Dogan, B. Schwederski, T. Schleid, F. Lissner, J. Fiedler and W. Kaim, *Inorg. Chem. Commun.* (2004), ***7***, 220-223.
[53] F.H. Allen, *Acta Crystallogr., Sect. B: Struct. Sci* (2002), ***B58***, 380-388.
[54] K. Hüttinger, C. Förster, T. Bund, D. Hinderberger and K. Heinze, *Inorg. Chem.* (2012), ***51***, 4180-4192.
[55] D. Gerlach, E. Brendler, T. Heine and J. Wagler, *Organometallics* (2006), ***26***, 234-240.
[56] M.N.Tahir, M.I.Tariq, S.Ahmad, M.Sarfraz and R.H.Tariq, *Acta Crystallogr. Sect. E: Struct. Rep.* (2010), ***E66***, o2295.
[57] F. Franceschi, G. Guillemot, E. Solari, C. Floriani, H.B. N. Re and P. Pattison, *Chem.Eur. J.* (2001), ***7***, 1468-1478.
[58] T. Steiner, *Chem. Commun.* (1997), ***8***, 727-734.
[59] C.M. Wansapura, C. Juyoung, J.L. Simpson, D. Szymanski, G.R. Eaton, S.S. Eaton and S. Fox, *J. Coord. Chem.* (2003), ***56***, 975-993.
[60] A. Casini, M.C. Diawara, R. Scopelliti, S.M. Zakeeruddin, M. Gratzel and P.J. Dyson, *Dalton Trans.* (2010), ***39***, 2239-2245.

[61] F. Abbate, P. Orioli, B. Bruni, G. Marcon and L. Messori, *Inorg. Chim. Acta* (2000), ***311***, 1-5.
[62] *Saint and SADABS*, version 2012 Bruker Apex2, Bruker Axs Inc., Madison, Wisconsin, USA, (2012).
[63] G.M. Sheldrick, *Acta Crystallogr.* (2008), ***A64***, 112-122.
[64] L.J. Farrugia, *Appl. Cryst.* (2012), ***45***, 849-854.
[65] Newport Experience Solutions. http://www.newport.com/Introduction-to-FTIR-Spectroscopy/405840/1033/content.aspx (accessed Sep 27, 2014).
[66] B.B. Koleva, T. Kolev and M. Spiteller, *Inorg. Chim.* (2007), ***360***, 2224-2230.
[67] D.L. Pavia, G.M. Lampman, G.S. Kriz and J.R. Vyvyan, *Introduction to Spectroscopy*. 4th ed.; Brooks/Cole: 2009.
[68] A. Garza-Ortiz, H. Den Dulk, J. Brouwer, H. Kooijman, A.L. Spek and J. Reedijk, *J. Inorg. Biochem.* (2007), ***101***, 1922-1930.
[69] A. Blackman and S. Bottle, *Chemistry*. John Wiley & Sons: 2007.
[70] D. Skoog, *Instrumental Analysis Priciples*. 6 ed.; Brooks/Cole: 2006.
[71] B.B. Koleva, T. Koleva, S.Y. Zareva and M. Spiteller, *J. Mol. Struct.* (2007), ***83***, 165-173.
[72] Y. Yang, M.N. Weaver and K.M.M. Jr, *J Phys. Chem. A.* (2009), ***36***, 9843-9851.
[73] I.Y. Zhang, J. Wu and X. Xu, *Chem. Commun.* (2010), ***46***, 3057-3070.
[74] A.D. Mclean and G.S. Chandler, *J. Chem. Phys* (1980), ***72***, 5639-5648.
[75] K. Raghavachari, J.S. Binkley, R. Seeger and J.A. Pople, *J. Chem. Phys* (1980), ***72***, 650-654.
[76] M. Bortoluzzi, G. Paolucci, G. Annibale and B. Pitteri, *Polyhedron* (2009), ***28***, 1079-1084.
[77] C. Qin, G. Yang, L. Zhao, S. Sun, Y. Qiu, Z. Sua and Y. Zhu, *Synth. Met.* (2009), ***159***, 2406-2409.
[78] J.P. Perdew, K. Burke and M. Ernzerhof, *Phys. Rev. Lett* (1996), ***77***, 3865-3868.
[79] J.P. Perdew, K. Burke and M. Ernzerhof, *Phys. Rev. Lett* (1997), ***78***, 1396.
[80] A.J.H. Wachters, *J. Chem. Phys* (1970), ***52***, 1033.
[81] P.J. Hay, *J. Chem. Phys* (1977), ***66***, 4377-4384.
[82] K. Raghavachari and G.W. Trucks, *J. Chem. Phys* (1989), ***91***, 1062-1065.
[83] S.D. Bella, I. Fragalà, A. Guerri, P. Dapporto and K. Nakatani, *Inorg. Chim. Acta* (2004), ***357***, 1161-1167.
[84] I.J. Bruno, J.C. Cole, P.R. Edgington, M. Kessler, C.F. Macrae, P. Mccabe, J. Pearson and R. Taylor, *Acta Cryst.* (2002), ***B58***, 389-397.
[85] G. Zhang, G. Yang, Q. Chen and J.S. Ma, *Cryst. Growth Des.* (2005), ***5***, 661-666.
[86] R. Bauernschmitt and R. Ahlrichs, *Chem. Phys. Lett* (1996), ***256***, 454-464.
[87] M.E. Casida, C. Jamorski, K.C. Casida and D. R. Salahub, *J. Chem. Phys* (1998), ***108***, 4439-4449.
[88] E. Stratmann, G.E. Scuseria and M.J. Frisch, *J. Chem. Phys* (1998), ***109***, 8218-8224.
[89] C.V. Caillie and R.D. Amos, *Chem. Phys. Lett* (1999), ***308***, 249-55.
[90] C.V. Caillie and R.D. Amos, *Chem. Phys. Lett* (2000), ***317***, 159-164.
[91] F. Furche and R. Ahlrichs, *J. Chem. Phys* (2002), ***117***, 7433-7447.
[92] G. Scalmani, M.J. Frisch, B. Mennucci, J. Tomasi, R. Cammi and V. Barone, *Chem. Phys.* (2006), ***124***, 094107:1-15.
[93] G.W.T. M. J. Frisch, H. B. Schlegel, G. E. Scuseria, M. A. Robb, J. R. Cheeseman, G. Scalmani, V. Barone, B. Mennucci, G. A. Petersson, H. Nakatsuji, M. Caricato, X. Li, H. P. Hratchian, A. F. Izmaylov, J. Bloino, G. Zheng, J. L. Sonnenberg, M. Hada, M. Ehara, K. Toyota, R. Fukuda, J. Hasegawa, M. Ishida, T. Nakajima, Y. Honda, O. Kitao, H. Nakai, T. Vreven, J. A. Montgomery, Jr., J. E. Peralta, F. Ogliaro, M. Bearpark, J. J. Heyd, E. Brothers, K. N. Kudin, V. N. Staroverov, R. Kobayashi, J.

Normand, K. Raghavachari, A. Rendell, J. C. Burant, S. S. Iyengar, J. Tomasi, M. Cossi, N. Rega, J. M. Millam, M. Klene, J. E. Knox, J. B. Cross, V. Bakken, C. Adamo, J. Jaramillo, R. Gomperts, R. E. Stratmann, O. Yazyev, A. J. Austin, R. Cammi, C. Pomelli, J. W. Ochterski, R. L. Martin, K. Morokuma, V. G. Zakrzewski, G. A. Voth, P. Salvador, J. J. Dannenberg, S. Dapprich, A. D. Daniels, Ö. Farkas, J. B. Foresman, J. V. Ortiz, J. Cioslowski, and D. J. Fox,*Gaussian 09*, Gaussian, Inc: Wallingford CT, 2009.

[94] *OriginPro*, 8; OriginLab Corporation: Northampton, MA 01060 USA.

[95] L.H. Hurley, *Nat. Rev. Cancer* (2002), ***2***, 188-200.

[96] K.J. Kilpin, W. Henderson and B.K. Nicholson, *Dalton Trans.* (2008), ***29***, 3899-3906.

[97] Nci National Cancer Institute. http://www.cancer.gov (accessed 23/09).

[98] G. Tripodo, D. Mandracchia, S. Collina, M. Rui and D. Rossi, *Med. Chem.* (2014), ***S1***, 004.

[99] S. Chen, X. Zhao, J. Chen, J. Chen, L. Kuznetsova, S.S. Wong and I. Ojima, *Bioconjug Chem.* (2010), ***21***, 979-987.